2009

Modeling of Solid Oxide Fuel Cell functionally graded electrodes and a feasibility study of fabrication techniques for functionally graded electrodes

Reuben Flesner
Iowa State University

Modeling of Solid Oxide Fuel Cell functionally graded electrodes and a feasibility study of fabrication techniques for functionally graded electrodes

by

Reuben Richard Flesner

A thesis submitted to the graduate faculty

in partial fulfillment of the requirements for the degree of

MASTER OF SCIENCE

Major: Mechanical Engineering

Program of Study Committee:
Gap-Yong Kim, Major Professor
Steve W. Martin
Sriram Sundararajan

Iowa State University

Ames, Iowa

2009

TABLE OF CONTENTS

LIST OF FIGURES

LIST OF TABLES

ACKNOWLEDGEMENTS

I would like to take this opportunity to thank those who have assisted me throughout my graduate education and provided input and help during the writing of my thesis. First, I would like to thank Dr. Gap-Yong Kim for his guidance in concept clarification, presentation of this research, and financial support. I would also like to thank Dr. Sriram Sundararajan and Dr. Steve W. Martin for their input and taking the time to help with my thesis. I would also like to thank Dr. Baskar Ganapathysubramanian for his assistance in developing the numerical solver used for all of the results in this work. Without him, this work would not have been possible.

I would like to thank my wife Bekki for her support and understanding, and my family for their interest in my work and understanding the nature of research.

ABSTRACT

With the large energy demands, finite natural resources, and concern about carbon emissions, a more efficient method to produce energy for the electrical power grid is needed. Solid Oxide Fuel Cells (SOFC) have demonstrated nearly 70% efficiency in full scale trials. Much time has been spent reducing the cost of SOFCs, but little investigative focus has been put on optimal power output based on electrode microstructure. Moreover, it appears that no modeling has investigated optimization behavior of functionally graded SOFC electrodes. Also, nonlinear functional grading of SOFC electrodes has not been explored.

In this work, a complete SOFC electrode model from literature was adapted for use in analyzing and comparing the losses between homogeneous, linearly, and nonlinearly graded electrodes. The model is based on a coupled differential equation system that was iteratively solved for three dependent variables: voltage, electronic current, and reactant gas pressure.

It was found that particle size and porosity functional grading reduce diffusion losses near the electrode's free surface, while decreasing activation loss levels near the electrolyte interface. A range of particle sizes was identified around the optimal homogenous electrode particles size, where particle size grading is beneficial. Outside of this range, homogeneous structured electrodes show better performance. Nonlinear porosity grading shows an improvement over linear grading in voltage losses at small particle diameters (300 nm); little to no benefit is seen for larger particle diameters (3 μm).

This work discusses (1) relative loss contribution in a SOFC electrode, (2) particle size and porosity grading ranges and their associated grading profiles for optimal performance, and (3) design criteria for the efficacy of particle size graded verses homogeneous electrodes. This work can be used to further explore the contribution of individual losses in a SOFC electrode. This information can then be used to further understand how to optimize SOFCs.

CHAPTER 1. INTRODUCTION

1.1 Motivation

With the large energy demands, finite natural resources, and concern about carbon emissions, a more efficient method to produce energy for the electrical power grid is needed. As seen in Figure 1, the net electrical generation efficiency in 2007 was 34%. The largest fuel source for electrical generation was coal at 50%, while the rest was comprised of nuclear, natural gas, and renewable energy sources [1]. Hitachi finished the highest efficiency coal fired power plant of its time in 2002 and with its efficiency of 44%, which is still wasting 56% of the energy [2].

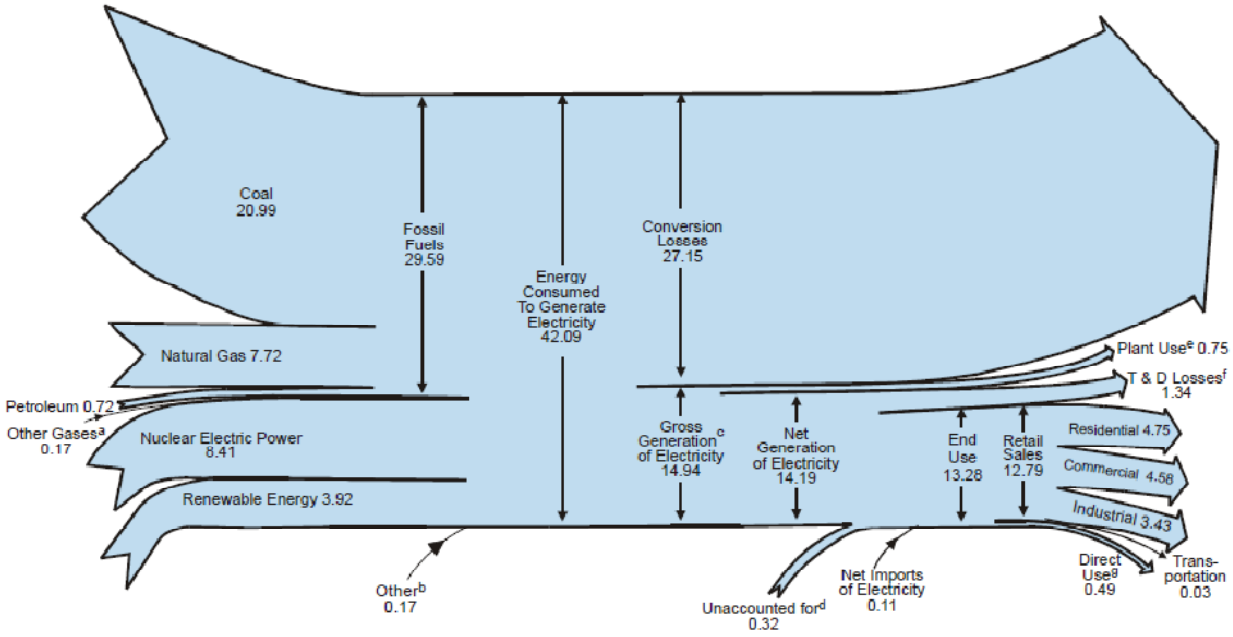

Figure 1. Electricity flow for 2007 from the Energy Information Administration [1].

Solid Oxide Fuel Cells (SOFCs) are one potential solution to energy problems. SOFCs are about 50-60% efficient lower heating value (LHV) alone. Moreover, the high temperature of the exhaust above 650°C, can be put in a cogeneration setup to capture more energy [3]. NetGen of Australia has attained 80% efficiency with a cogeneration setup [4]. Siemens Westinghouse and McDermott Technology have separately developed SOFC-turbine systems of 20 MW and 770 kW, respectively, that achieved nearly 70% efficiency by

2004 [5]. Another major advantage of a SOFC is its fuel flexibility, i.e. the ability to utilize gasified hydrocarbons, ammonia, and carbon monoxide as fuels. Carbon monoxide can poison other fuel cell types. SOFCs can also tolerate sulfur in the fuel stream [6]. Also, no electrolyte maintenance is needed as with other fuel cells. Figure 2 graphically shows power generation techniques and their efficiency relative to the plant size. As can be seen, SOFCs are more efficient than many other common power generation techniques. SOFCs have lower SO_x and NO_x emissions than other power generation techniques [7]. They also are completely quiet, which allows them to be put in and around residential areas. This cannot be done with typical power plants. Since there are no moving parts, less maintenance is required. In addition, SOFCs are efficient in auxiliary applications which cannot be done with common high efficient power generation techniques, due to scale considerations.

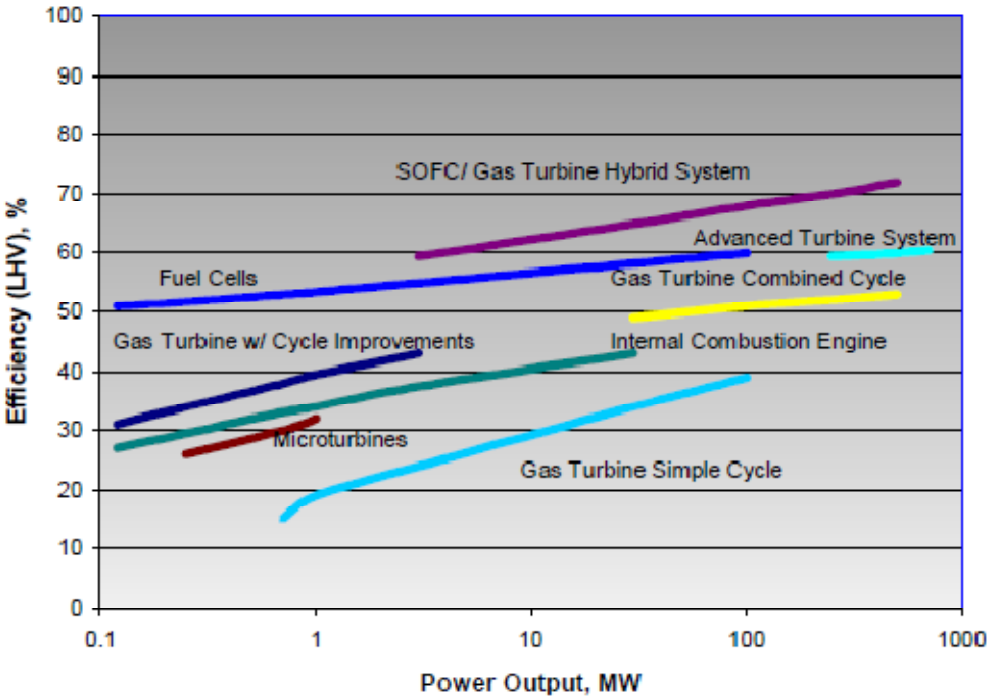

Figure 2. Efficiency of power generation techniques verses scale [5].

Overall, SOFCs are an attractive technology for power generation and have desirable performance in terms of efficiency, simplicity, and maintenance. SOFCs have still not met the performance and cost criteria for commercial implementation. The Solid State Energy Conversion Alliance (SECA) has laid out a three phase program for cost reduction of SOFC

technology to $400/kW capacity installed [8]. The systems developed also need to have less than 2% decrease in power over an operating period of 1500 hours. The goals were chosen to be competitive with existing generation systems, such as diesel-powered generators. All of the program's development teams, including General Electric, Cummins Power Generation, Delphi, and others, are on pace for completion in 2010 [8-9].

While much focus has been put on cost, efficiency, and cell life, little attention has been paid to optimizing peak power output. The SECA program participants are not using functionally graded structures in their SOFCs [9-10]. One way to further improve the performance is to employ functionally graded cell structures. Results from mathematical modeling and experimentation efforts indicate potentially drastic improvement in power output may be achieved. Functionally graded structures have been shown to improve power output; through mathematical modeling and experimentation efforts [11-16]. Ni et al, which appears to be the only full model exploring functionally graded electrodes (FGE), developed a complete model to account for FGEs but did not optimize the system [17]. Schneider et al and Greene et al have modeled conduction percolation effects and mass transfer effects in a SOFC electrode, respectively [18-19]. These models are not complete. Experimentally, large increases in performance have been reported by grading pore size, particle size, porosity, and material composition [11-12, 20].

Ni et al's model varied the electrode structure continuously and linearly, which leaves many more graded structures to be explored. Most fabrication techniques cannot vary electrode structure continuously. Existing studies do not consider future manufacturing capability of existing processes. The following work will show system behavior of particle size and porosity graded SOFC electrodes.

1.2 Research Framework

1.2.1 Feasibility Study of Fabrication Techniques for Functionally Graded SOFC Electrodes

This study investigated possible fabrication techniques for their ability to make graded structures in a manufacturing setting. Fabrication parameters investigated include the ability

to make: continuously graded structures, a structure with desired porosity ranges, and a desired structure with low time cost and complexity.

1.2.2 Modeling of Graded SOFC Electrodes

A complete SOFC electrode model was used with a developed equation set for microstructural grading. This electrode model has been used to investigate and compare homogeneous, linear, and nonlinear structure grading influences on power losses within a SOFC electrode.

1.2.2.1 Modeling of Particle Size Graded SOFC Electrodes

Nonlinear particle size grading is compared and contrasted with linear particle size grading. Peak electrode performance depends on particle size grading range and particle size grading profile. This work also discusses design criteria for the efficacy of particle size graded verses homogeneous structures. Above and below different critical particle sizes, particle size grading in an electrode displays lower power performance than a homogeneous electrode. The causes of this behavior is discussed.

1.2.2.2 Modeling of Porosity Graded SOFC Electrodes

Nonlinear porosity grading is compared and contrasted with linear porosity grading. Peak performance depends on the porosity grading range and profile. The electrode behavior is explained taking into account activation, binary, and Knudsen diffusion losses.

1.3 Research Objectives

The objectives of the research are: (1) to analyze possible fabrication techniques for their ability to make graded SOFC electrodes; (2) to develop a numerical model that can evaluate the performance of graded electrode structures in a SOFC; (3) to quantitatively understand the effect of nonlinear particle size and porosity grading in a SOFC electrode and then compare to homogeneous and linearly graded electrodes; and (4) to establish design guidelines for SOFC electrode fabrication for optimal power output.

1.4 Thesis Organization

The rest of this thesis is divided into seven chapters. Chapters 2 and 3 are overviews of SOFC theory and a feasibility study for functionally graded SOFC electrode fabrication techniques. Chapter 4 discusses the model development. Chapter 5 presents the modeling results and discussion that accounts for FGE behavior in SOFCs. Model validation is also discussed in this chapter. Finally, conclusions about this work are presented in chapter 6. Suggested future work is in chapter 7. Chapter 8 contains all references and is followed by all appendix material.

CHAPTER 2. OVERVIEW OF SOLID OXIDE FUELS CELLS

In 1899 Nernst discovered that YSZ was a solid-state oxygen ion conductor at high temperatures. Schottky, one of Nernst's students, proposed the idea of the Solid Oxide Fuel Cell (SOFC) and the idea came to fruition when Baur and Preis built the first functioning SOFC in 1937 [6].

2.1 Theory

A fuel cell consists of an anode, electrolyte, and cathode, as seen in Figure 3. In its most basic operation, oxygen is supplied to the cathode and hydrogen to the anode. Oxygen is ionized in the porous cathode and then conducted through the dense electrolyte and reacted with ionized hydrogen in the porous anode, forming water. The two half reactions are represented in Eqn. (1) and (2), while the overall reaction products are water, electrons, and heat; as seen in Eqn. (3). From these reactions electricity can be generated.

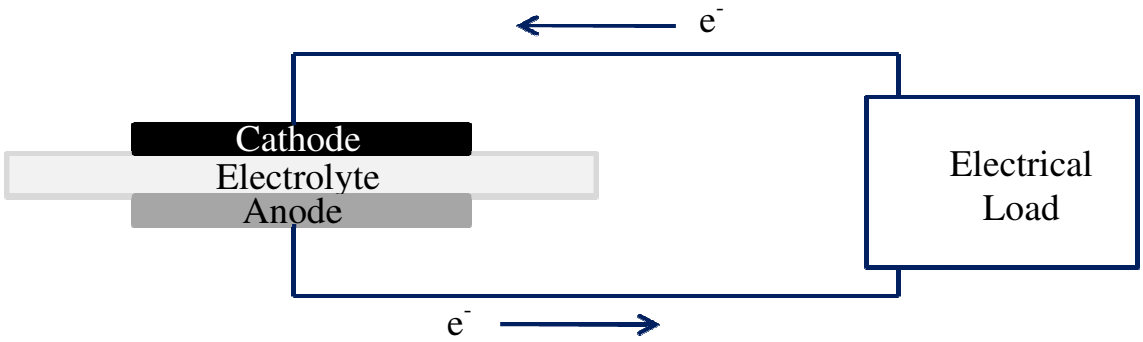

Figure 3. Electrolyte-supported SOFC.

$$\frac{1}{2}O_2 + 2e^- \xrightarrow{catalyst} O^{2-} \quad (1)$$

$$H_2 + O^{2-} \xrightarrow{catalyst} H_2O + 2e^- \quad (2)$$

$$\text{Overall, } \frac{1}{2}O_2 + H_2 \rightarrow H_2O + 2e^- + Heat \quad (3)$$

The electrolyte is electrically insulating and ionically conductive. This forces the electrical circuit external to the cell, where it can be used for electrical work while allowing the electrochemical reaction to proceed.

The reactions in the electrodes occur at triple phase boundary (TPB) sites. TPBs exist where the reactant gas comes into contact with an electronic conductor and an ionic conductor; hence, triple phase boundary [21], as seen in Figure 4. A SOFC electrode with more TPBs will lead to more reactions, which leads to an increase in electrical power output. Oxygen ions are made in the cathode, conducted through the electrolyte, and into the anode. Once in the anode, the formation of water reaction will occur at a TPB and release electrons. The electrons are then conducted to the anode free surface for current collection.

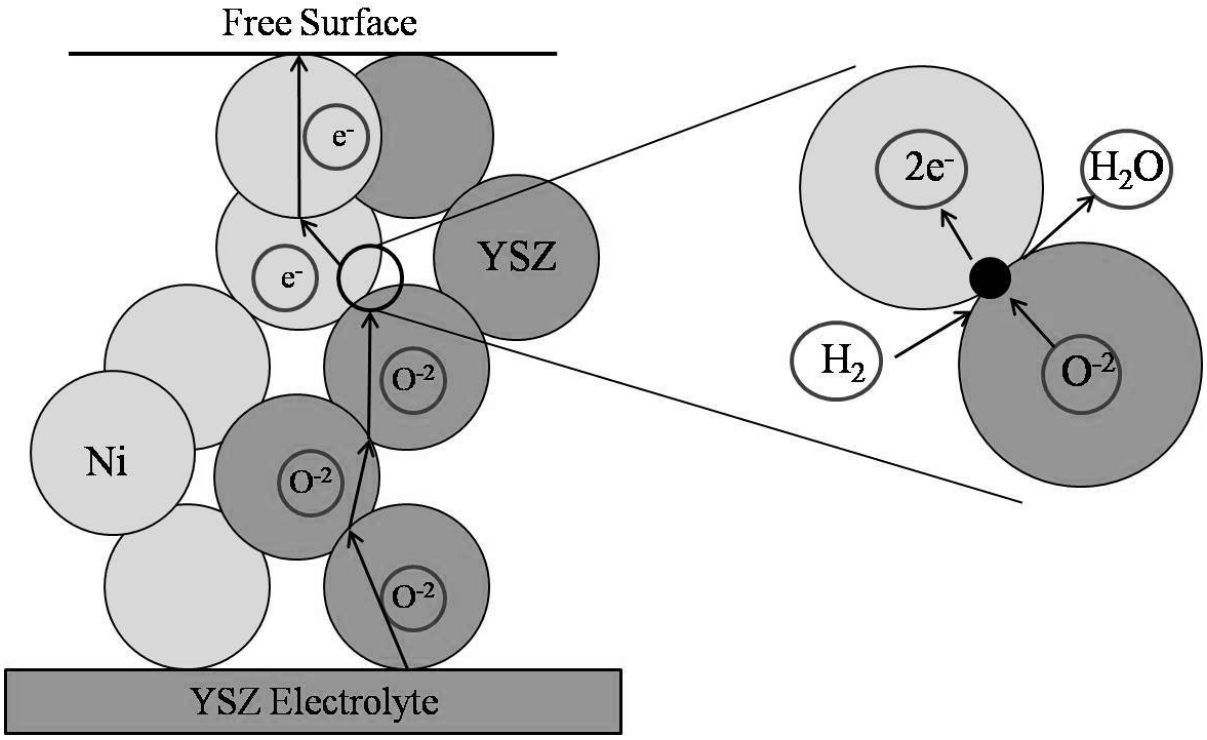

Figure 4. Anode triple phase boundary site model.

To obtain these sites in the anode, a Ni-YSZ cermet is used. Nickel is electronically conductive, YSZ is an ionic conductor, and hydrogen is the reactant gas. The cathode is typically a LSM-YSZ composite. They are electronically and ionically conductive,

respectively. These materials have been chosen for their stability in redox environments and coefficient of thermal expansion (CTE). The CTE mismatch needs to be small to reduce thermally induced stresses in the thin (<150 μm) oxide ceramic structure while it is cycled from ambient to operating temperatures as high as 1000 ºC.

To complete the electrical circuit between the electrodes, the oxygen ions must be conducted through the electrolyte. Traditionally the electrolyte is made of YSZ. This requires the operating temperature of YSZ-based fuel cells to be 800-1000 °C [6].

2.2 Efficiencies and Polarizations

SOFCs are affected by different phenomena while in different operating regimes. There are three efficiencies that SOFCs follow: (1) thermodynamic efficiency, (2) voltage efficiency, and (3) current efficiency [6].

Thermodynamic efficiency is dependent on the Nernst potential which is determined by the type and partial pressures of reactant gasses being utilized in the SOFC. This is the open-circuit voltage (OCV) of the fuel cell. As the operating temperature increases, the Nernst potential decreases, as seen in Figure 5. Although, ionic conduction efficiencies increase with temperature, making a higher operating temperature more effective than a lower one.

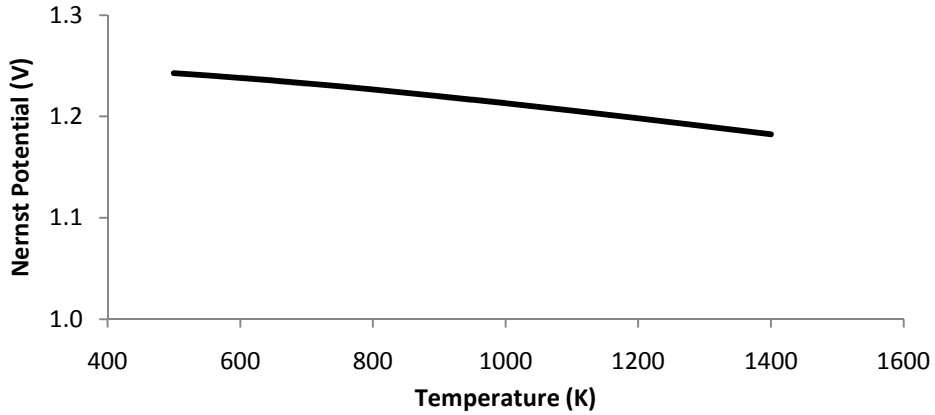

Figure 5. Nernst potential verses temperature using Nernst equation from table values [6].

Voltage efficiency is dependent on three polarizations which are widely studied: (1) activation polarization, (2) Ohmic polarization, and (3) concentration polarization. A polarization can also be called an overpotential, overvoltage, or loss. These polarizations are evident in a characteristic SOFC curve as seen in Figure 6 and are dominant in the regions they are named, although they are present at all current densities. Activation polarizations are due to the activation barrier energy needed for the catalytic reaction to occur and begin the charge transfer. This polarization is dependent on temperature, surface area, concentration, and material. Ohmic polarization is due to electrical and ionic resistances in the circuit. Electrical resistances are present in the electrodes and conducting wires. Ionic resistance is present in the electrolyte and electrodes of the SOFC. Concentration polarizations are caused by a local lack of reactants at the reaction site. This can be caused by slowed diffusion of a reactant gas to the reaction site or the site being saturated with reacted components. The voltage efficiencies are discussed in further detail later.

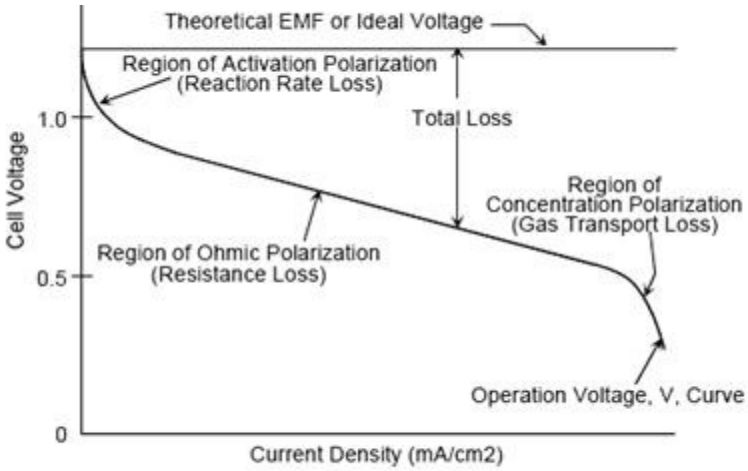

Figure 6. Typical Polarization V-I Curve of SOFC [22].

Current efficiency is due to reactants being converted into an undesirable product, resulting in a lower current. For example, if one hydrogen ion and one oxygen ion join, a hydroxide ion is formed, releasing only one electron. If the ion reacted with another hydrogen ion, then another electron will be released, doubling the charge produced. Of the three efficiencies presented the thermodynamic and voltage efficiencies are dominant.

Fuel utilization is an important consideration when implementing fuel cell technology at a large scale, for practical reasons. As seen in Figure 7, a fuel cell operating voltage is lower when it is utilizing more fuel. For this reason, a voltage of 0.7 V is used as a standard condition for reporting and consistency between studies. The theoretical fuel utilization at 0.7 V is 99.462%. If the voltage is lower than this, there are only greatly diminishing returns. Depending on the application, the system may be operated at a higher voltage so the unused fuel may then be combusted to produce heat, resulting in a cogeneration process.

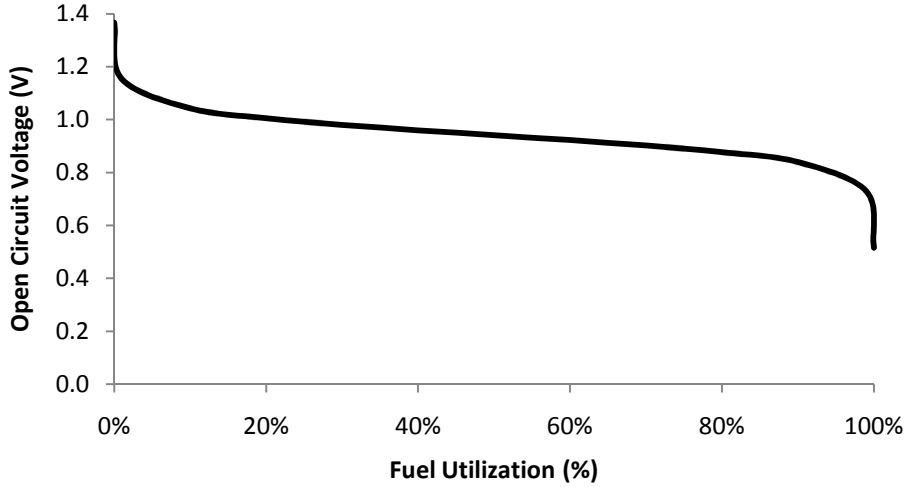

Figure 7. Open circuit voltage of a H_2-air fuel cell verses fuel utilization at 800°C.

2.3 SOFC Configurations

There are four SOFC configurations: (1) planar, (2) tubular, (3) monolithic, and (4) coplanar as seen in Figure 8. Coplanar is the only configuration that does not separate the reactant gasses. This also leads to a lower efficiency for this type. The anode and electrolyte-supported planar cells are the most common. The anode-supported cell is popular for its high power density and the electrolyte-supported cell is popular for its ease of sealing. The tubular configuration does not require the anode be on the outside of the tube. The order of cell components can be reversed concentrically. This type of configuration has been developed by Siemens Westinghouse for decades because it can be easily mass produced by extrusion and dip coating processes [23]. The monolithic structure is used to increase power per volume.

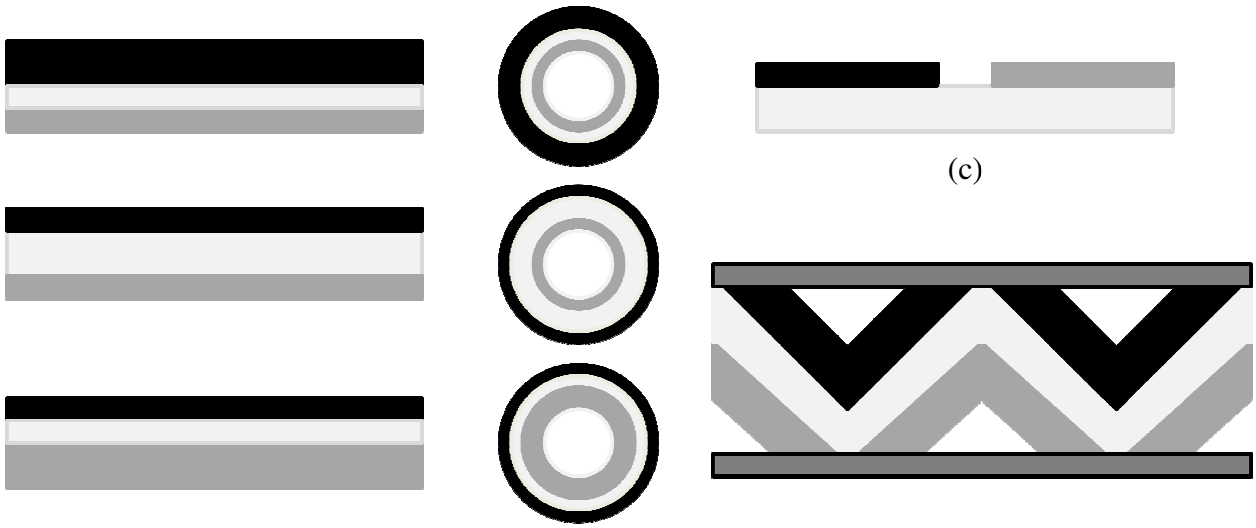

Figure 8. SOFC configurations. The anode, electrolyte, and cathode are designated with black, light gray, and dark gray colors, respectively. The (a) planar and (b) tubular configurations are anode, electrolyte, and cathode supported from top to bottom; (c) coplanar configuration; (d) monolithic configuration shown with interconnects.

The cell structure on the right of Figure 9 shows the cell design developed by Siemens Power Generation to increase volumetric power density. Their old design is on the left. This configuration typically utilizes a one-step sintering process for the entire structure.

Figure 9. Siemens' HPD5 and Delta9 cell stacks, developed in 2005 [10].

2.4 Graded Electrodes

It has been found that grading the structure of an electrode can increase its performance by reducing voltage losses [16]. An electrode can be graded in three ways: (1) porosity, (2) composition, and (3) particle size [17], as seen in Figure 10. Porosity grading changes the percent porosity through the structure. This grading reduces mass transfer losses. Compositional grading changes the number ratio of electronic and ionic conductors through the structure. The black particles are the electronic conductors, while the gray particles are the ionic conductors. This grading reduces Ohmic percolation losses. Particle size grading changes the electronic and ionic conducting particle's sizes through the structure. This grading reduces mass transfer and activation losses.

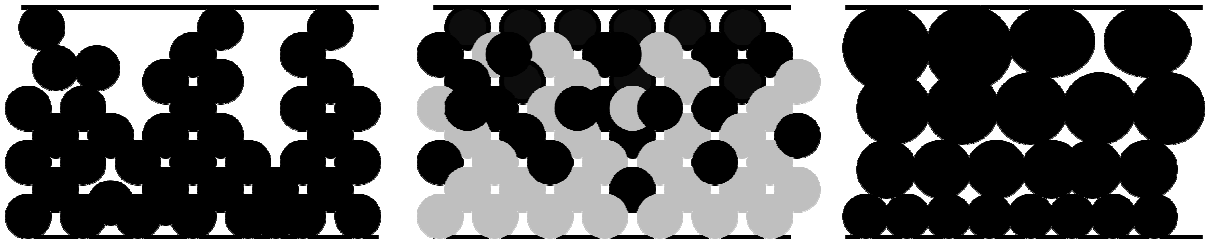

Figure 10. Porosity, composition, and particle size grading schematic.

2.5 Practical Considerations

SOFC's can use a wide range of fuels including hydrogen, methane, propane, diesel, kerosene, ammonia, gasified coal, and carbon monoxide [6]. Carbon monoxide poisons other types of fuel cells. Lost function due to impurities in the reactant stream can be recovered by supplying clean reactants to the fuel cell. These impurities attack the reaction sites in the electrodes, ultimately affecting the effective exchange current density. The exchange current density is an electrochemical property that determines the rate of electrochemical reactions; the higher the value, the faster the reaction. Noble metals are known for their catalytic properties but are cost prohibitive. The Pt family exchange current values range from 10

A/m^2 for platinum to 2 A/m^2 for iridium, while nickel is 0.06 A/m^2; yet nickel is the catalyst of choice for most fuel cells, due to cost [6].

2.5.1 Factors that Influence Conductivity

The electronic and ionic conductivities are important factors in SOFC function. It has been found that anode conductivity is strongly influenced by the element component ratio and microstructure homogeneity [24-25]. For example, if there is not enough nickel metal in the anode, it will not have continuous electrical conduction in the anode and the overall electrical conductivity will suffer. This statement is also true if the Ni-YSZ cermet is not thoroughly mixed. The cathode conductivity is strongly influenced by percent porosity and element component ratio [26]. The higher the porosity, the less material there is to form a conduction pathway.

2.5.2 Summary of SOFC Component Primary Properties

SOFC components need to be able to withstand high temperatures and strong reducing and oxidizing environments to perform as desired. The list below shows the required properties of SOFC components to perform well as a system. This is a summary of properties; there are many others depending on the particular system. For example, sealing requirements are system dependent.

1. Maintain mechanical strength and resist creep at temperatures of 600-1000°C.
2. The electrodes and electrolyte need a similar CTE to reduce thermal cycling fatigue.
3. Chemical stability under strong oxidizing environments for the cathode.
4. Chemical stability under strong oxidizing and reducing environments for the anode and electrolyte for an oxygen ion conducting SOFC.
5. Resistance to forming reaction products at component interfaces at high temperatures.
6. High mixed, electrical and ionic, conductivity in the electrodes.
7. High catalytic behavior in the electrodes; smaller particles are better.
8. High porosity and low tortuosity in the electrodes to aid gas transport.

CHAPTER 3. FEASABILITY STUDY OF SOFC FABRICATION TECHNIQUES

Sintering fabrication techniques are most commonly used to make SOFC structures. Other techniques have not been used as long, and therefore, have not developed to there full potential. Other researchers working toward commercialization are using tape casting, screen printing, tape calendaring, extrusion, dip processing, spray deposition, plasma spraying, and electrostatic deposition [10]. Since these methods are being widely pursued, these techniques will be studied for graded electrode commercial manufacturing. In this study, mist pyrolysis will also be considered for fabricating SOFCs.

The following review is selective in the sense that it will only look at characteristics of each fabrication technique that are critical to fabricating functionally graded planar SOFC electrodes. The most important fabrication characteristics are the ability to make a continuously variable structure, a structure with approximately 30% porosity, and have a low processing time cost and complexity. A truly continuously variable structure is not necessarily needed if multiple thin layers can be deposited to simulate the continuous variation. Also, the technique chosen must be able to at least utilize the most common materials used to make SOFCs.

Figure 11 shows the wide variety of materials being used and developed for SOFC applications. The most common SOFC system uses a Ni-YSZ anode, a YSZ electrolyte, and a LSM cathode. As can be seen, the more common materials are at the top of the lists. Since there is such a wide variety of materials the following sections will only consider the most common materials.

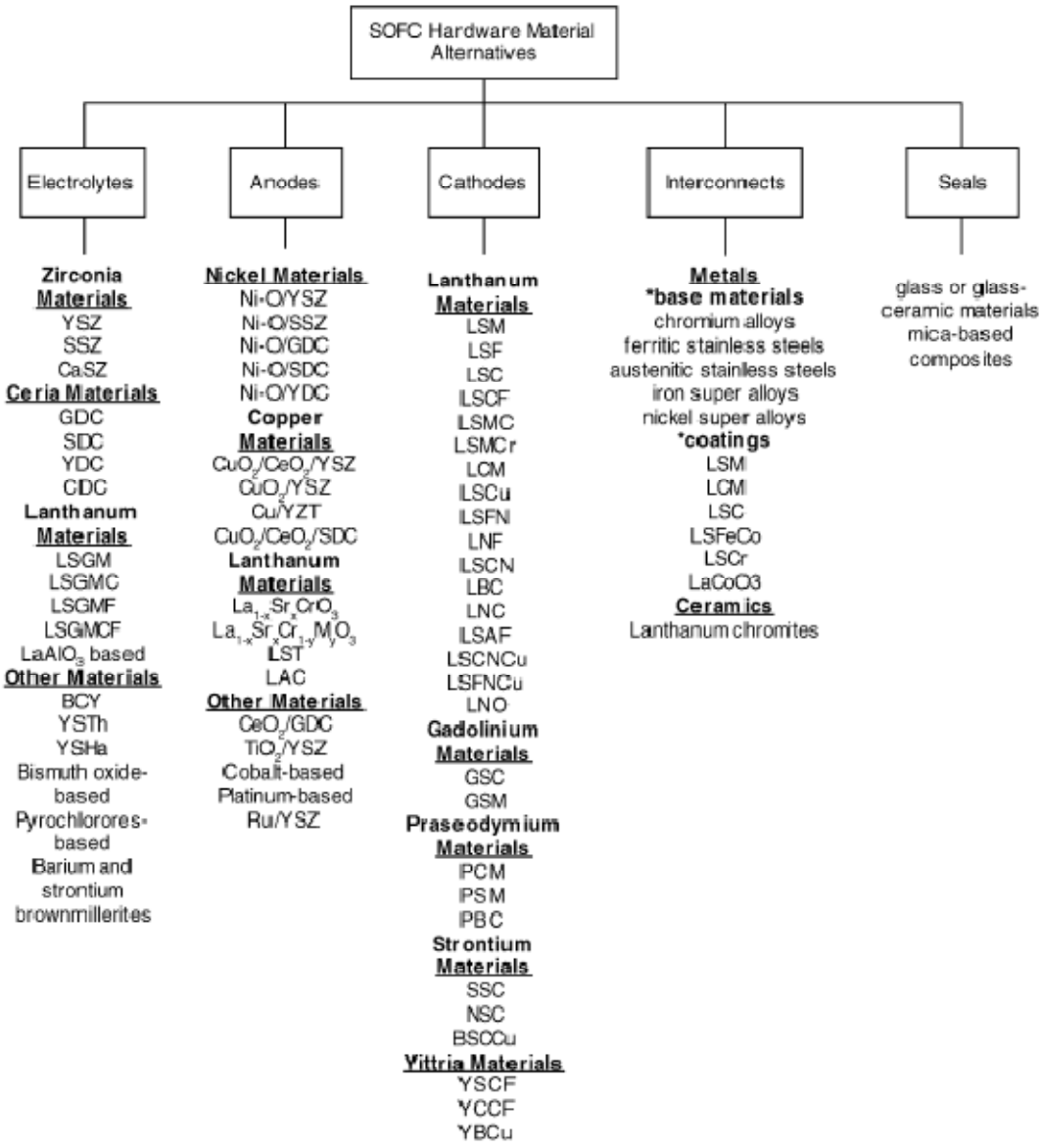

Figure 11. Taxonomy of SOFC materials [27].

3.1 Wet Ceramic Fabrication Techniques

All wet ceramic processing techniques discussed are a mixture of powders, poreformers, binders, and solvents that are, by multiple ways, deposited into a thin layer from single-digit to hundreds of microns thick. Once deposited, the wet ceramic must be dried and then sintered, a process also called densification since the overall size becomes smaller.

Sintering is a high temperature, sometimes high pressure, process of bonding powders below the materials' melting temperature. For example, after zirconia-based layers are formed, they are sintered at 1200-1400 °C, while ceria based layers are sintered at 900-1400 °C [25, 28-30]. Typically cathodes are sintered at lower temperatures than anodes, due to their higher reactivity with other cell components. Sintering can be done after each layer is deposited, or the whole structure can be deposited in a green state and cosintered. Since different components need different sintering temperatures, cosintering results in a non-ideal structure. Higher sintering temperatures and longer holding times, result in larger final particles. Generally, this leads to better grain structure for conductivity, but reduces TPBs and overall is detrimental to power performance.

Many methods can be utilized to produce desirable elemental powders. Glycine-nitrate [31], mist pyrolysis preparation, co-precipitation, strike precipitation, citric-nitrate [31-32], Pechini method [32], precipitation method [32] and others. These methods are used to make well mixed, monodisperse, sized powders. The powders can be further mixed with vehicles or solvents and then ball milled until desired dispersion is acquired. Common solvents are ethanol, acetone, terpineol [31, 33]. Binders are added to prevent cracking while the green ceramic dries and is sintered. Common binders are ethycellulose, polyvinyl butyal, and hexylene glycol [31, 33-34]. Pore-formers are generally added before the ball milling process. For electrodes, pore formers are used to create the desired porosity in the final structure. Some of these pore formers are: graphite, carbon black, rice starch, flour, and potato starch [25, 32, 35]. During sintering they are burned off or sublimed. Solvent can also be used as a pore former and may leave the structure even before sintering [36]. The powder material can also be acquired from various sources such as Tosoh, Praxair, Nextech, or Marketech International. Six commonly used wet ceramic fabrication techniques are described in the following sections. Since all of the techniques use similar slurry preparation technique, they are all capable of similar porosities of 0-60% [25, 37].

3.1.1 Tape Casting

Tape casting can be used to deposit electrolytes and electrodes. A thin substrate is pulled under a contained slurry solution, leaving a thin layer of deposited material. The

substrate is typically a thin sheet of Mylar or another component of a SOFC [25, 38]. A razor controls the thickness of slurry deposited; hence the name “doctor blading” is associated with this technique, as seen in Figure 12. After the slurry is put on the substrate, it is allowed to dry; then the structure is sintered. Almost any percent of porosity can be obtained with this technique with use of pore formers. Continuous gradation is not possible with this technique, but has demonstrated deposited layers as thin as 7 μm [39].

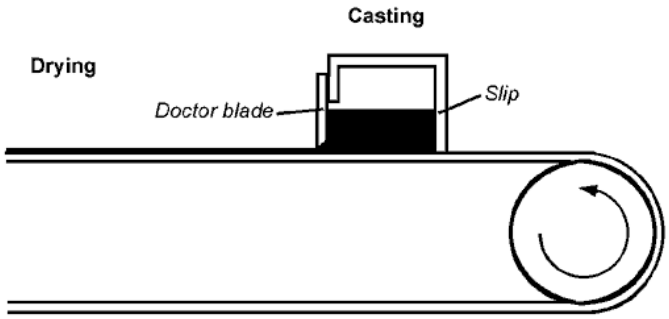

Figure 12. Tape casting schematic [40].

3.1.2 Screen Printing

Screen printing is the most common deposition technique for fabricating SOFC electrodes and electrolytes on their respective substrates. As seen in Figure 13, a screen of desired deposited material thickness is laid over a substrate. The material being deposited is put on top of the screen and flows through it. After this, the excess deposition material is removed from the top of the screen with a squeegee. Then the screen is removed. The material left on the substrate is evenly distributed. This technique is limited by the thickness of the screen and percent open area of the screen. Sometimes the same area of a substrate will be screen printed more than once to avoid spots from being missed. Layers have been made as thin as 8 μm [41].

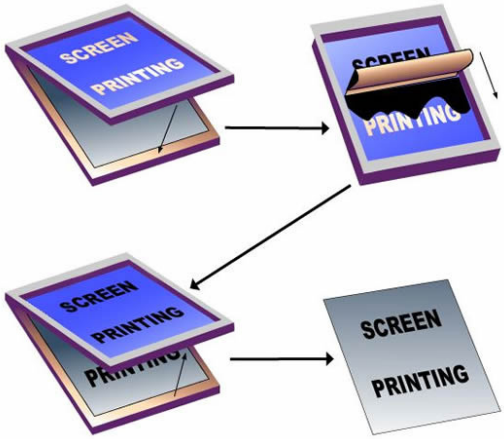

Figure 13. Screen printing schematic [42].

3.1.3 Spin Coating

Spin coating is a common technique for making SOFC components. Pore formers can be added to create porosity in the electrodes or left out to make a dense electrolyte. Figure 14 shows a schematic evolution of the process. First, a slurry solution is put on the substrate. The substrate is then spun, sometimes up to 10,000 RPM, and the solution is then allowed to dry [43]. This can be done multiple times to form one thick layer or a multi-layered structure. After each layer is deposited it is baked to fully evaporate solvents to prevent cracking [44]. Hui et al fabricated layers that were 1 to 9 µm thick. The film thickness in inversely proportional to the logarithm of the rotating speed [43].

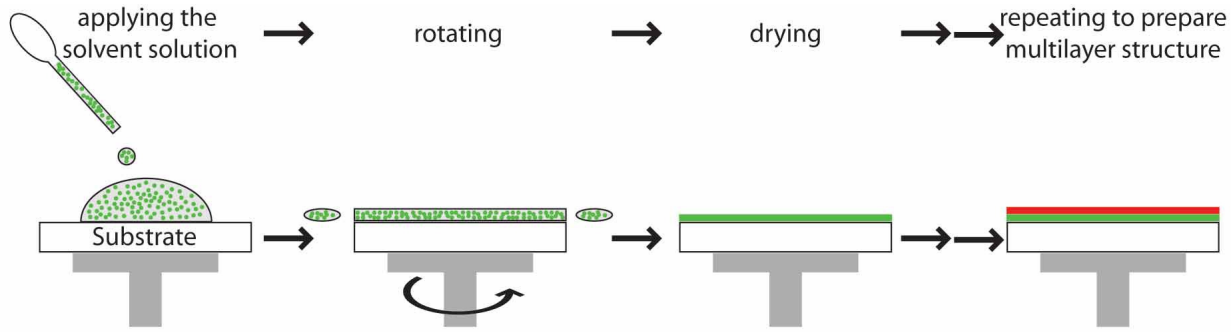

Figure 14. Spin coating schematic [45].

3.1.4 Dip Coating

Dip coating was primarily developed by Siemens in 1958 for tubular SOFCs [6]. This technique controls thickness of the layer deposited by varying the viscosity of the slurry and the rate at which the substrate is withdrawn from the slurry mixture. Unique to this technique is the varying deposited layer thickness from top to bottom as seen in Figure 15**.** This process cannot effectively make planar SOFC structures. Structures as thin as 10-15 µm have been made [37, 46].

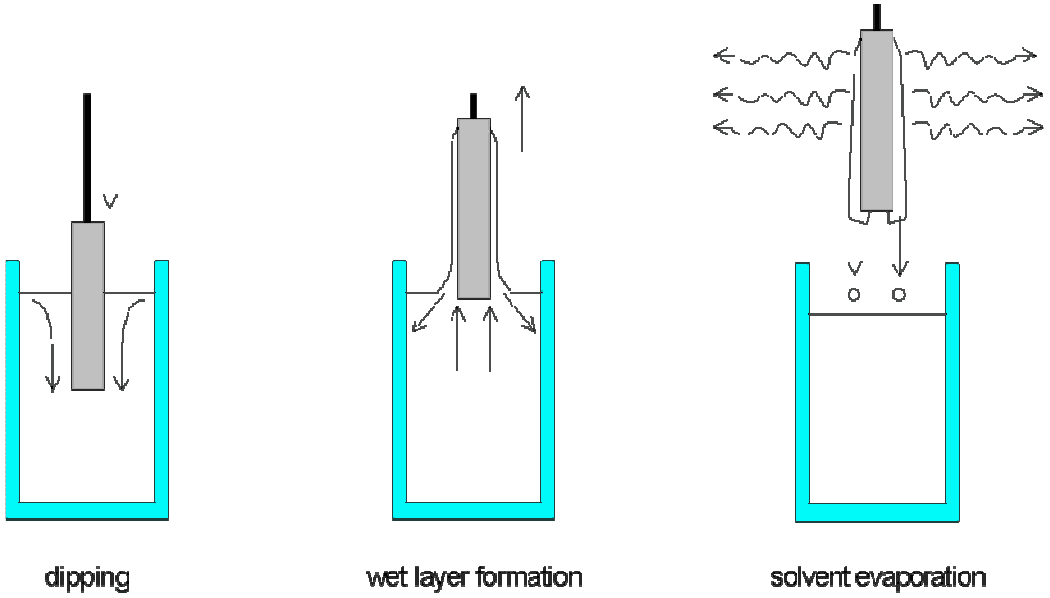

Figure 15. Dip coating schematic [47].

3.1.5 Extrusion Casting

Extrusion fabrication techniques are used to make a tubular or a flat-tube support for the other cell components. This technique is good for fabricating a cell component for other cell components to be deposited onto. This technique does not work with planar cell structures, as they are not self-supporting when in a green state. Extrusion requires a pre-firing heating step before a second component can be deposited onto it. Figure 16 shows cells made by extrusion casting and then dip coating.

Figure 16. Tubular cells fabricated, in part, by extrusion. The electrolyte was extruded, then the anode was dip coated on the inside of the tube, the assembly was fired, the cathode was slurry painted on, and the total assembly was fired again [48].

3.1.6 Tape Calendaring

Tape calendaring is a process that can be used to form a multilayer structure but cannot deposit the layers themselves. It combines multiple green ceramic tapes while controlling the thickness of each layer and the overall thickness during the process. Figure 17 shows a schematic of the tape calendaring process. A slurry solution is squeezed to a desired thickness between two thin pieces of tape and is then fed through a final set of rollers to laminate the number of layers desired. The tape material, containing the slurry, is baked out during the sintering process.

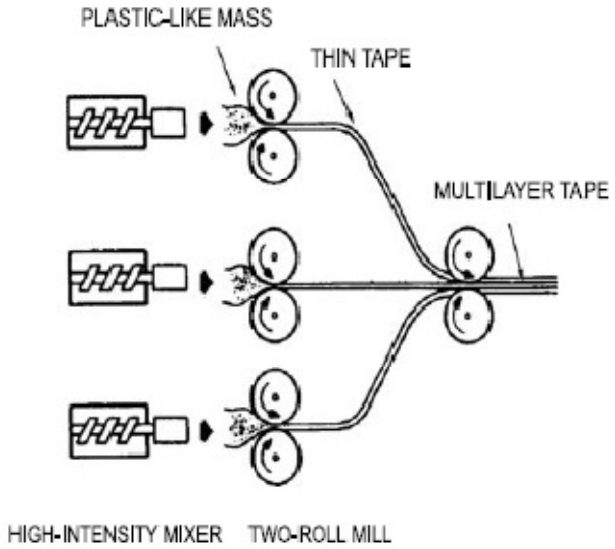

Figure 17. Tape calendaring schematic [49].

All of the previous techniques mentioned have the same potential for final particle size, pore size, and porosity in a SOFC electrode.

3.2 Spray Fabrication Techniques

Three spray techniques are presented in this section. They are plasma spraying, electrostatic deposition, and mist pyrolysis. The last two spray techniques are similar in that they use similar precursor solutions and heated substrates upon which the droplets are deposited. They are different when considering the droplet formation/atomization process and the transport of the droplet to the substrate. A requirement of the solution is that it must be a salt that is soluble in an alcohol or water and decompose to a salt oxide when deposited. Fortunately there are a large number of precursors that can be used with electrostatic deposition and mist pyrolysis [50].

3.2.1 Plasma Spraying

Figure 18 shows the basic concept of plasma spraying. A large electric potential is made between the anode and cathode, changing the feed gas to plasma. As the plasma is leaving the nozzle, the deposition powder is fed into the ionized gas stream, melting it nearly instantly. The material then splats onto the desired substrate cooling at 10^6-10^7 K/s. Plasma

spraying is capable of producing extremely thin layers and can make continuously graded structures by varying the deposition material and spray distance. Argon is easily ionized and often used as the plasma gas. The porosity range of a plasma sprayed layer is 5 to 15% [51]. Spraying distance and feed gas velocity influence the powder's time in the plasma, which determines if the material vaporizes, melts, or resolidifies before reaching the substrate [51]. A material that has close vaporizing and melting temperatures is difficult to deposit.

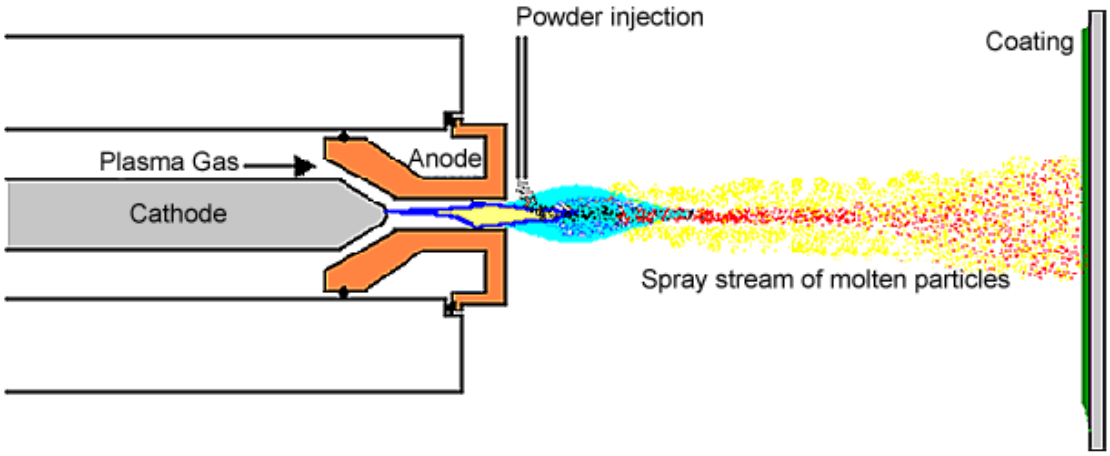

Figure 18. Plasma spraying schematic [52].

3.2.2 Electrostatic Spray Deposition

Electrostatic spray deposition (ESD) atomizes a precursor solution using electrostatic forces caused by a high voltage potential. The formed droplets are carried by electrostatic forces to a substrate on a hot plate where they are deposited. Figure 19 shows a schematic of electrostatic deposition. In the setup seen, the undesirably large droplets fall are not deposited due to gravity. They can be collected and atomized again so little goes to waste.

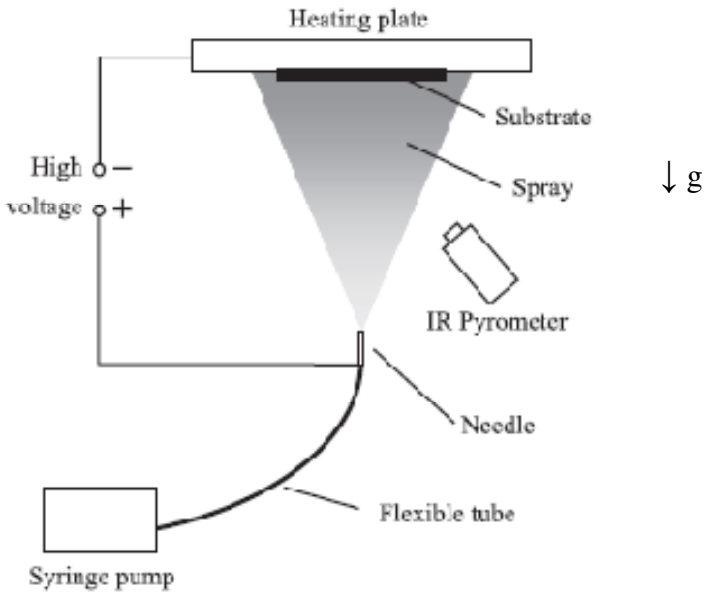

Figure 19. Electrostatic deposition [50].

The droplets that are deposited will be attracted to the highest point on the substrate because the electric field is slightly stronger there. This leads to preferential deposition and ends in a columnar structure if deposition is allowed to proceed, as seen in Figure 20. The longer the deposition time, the rougher the surface will be [50, 53-54]. The solution's surface tension, density, and electric conductivity influence the droplet size [50]. The density has the smallest influence on droplet size of the three properties. The stronger the electric field, the larger the droplets will be. Also, if the surface tension is high, the droplets will be larger. This fabrication technique can deposit layers as thin as the diameter of one droplet. Porosities as high as 60% have been demonstrated.

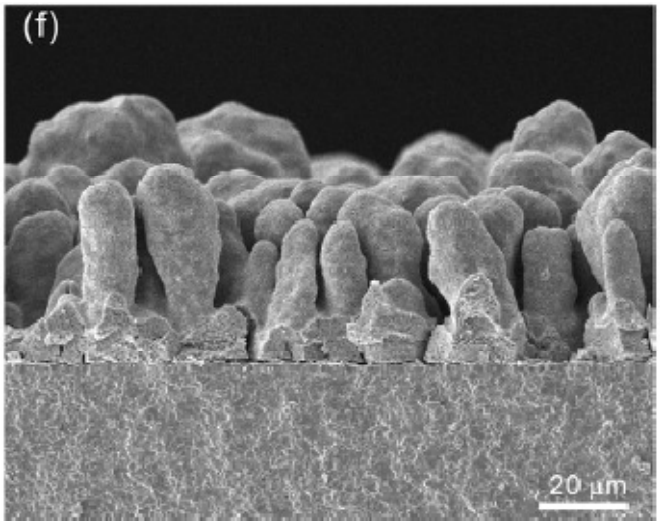

Figure 20. Strontium-doped samarium cobaltite layer with columnar structure. Electrostatic assistance was used to deposit a ultrasonically atomized precursor solution [53].

3.2.3 Ultrasonic Mist Spray Pyrolysis

Ultrasonic mist spray pyrolysis (MSP) atomizes a precursor solution using an ultrasonic atomizer or nebulizer, and then a carrier gas transports the droplets and deposits them onto a heated substrate, as seen in Figure 21. This technique can be used in many orientations. The hot plate can be set on a table, held horizontally, or even upside down, depending on the deposition characteristics desired. Porosities of 0 to 55% have been demonstrated [13, 25, 55-56]. This technique can be used to deposit monolayers of droplets and can vary structure continuously by changing the temperature of the hot plate, carrier gas velocity, or the precursor solution during deposition.

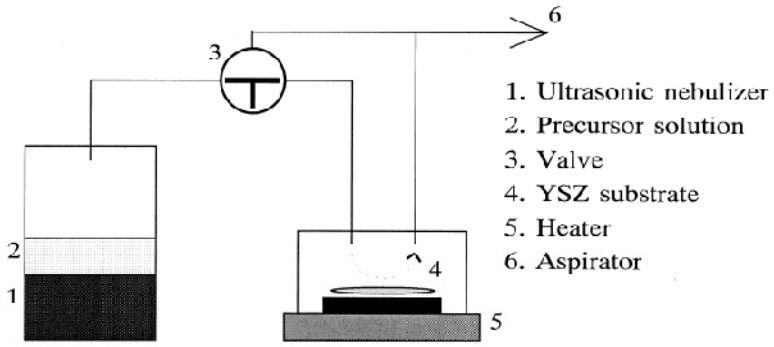

Figure 21. Mist pyrolysis schematic [57].

One variation of mist pyrolysis is shown in Figure 22. In this case, the deposition solution is atomized by ultrasonic motion. As the carrier gas moves the particles toward the substrate they become positively charged by a voltage potential so that they are drawn to the negatively charge, heated substrate. After deposition, the film is calcined [58]. Microstructural morphology varies with the potential applied. If the applied potential is 5 kV, the deposited layer is porous. When the potential is increased to 15 kV, the porosity is reduced because of the droplets being flattened before they decompose to an oxide solid resulting in denser structures [58].

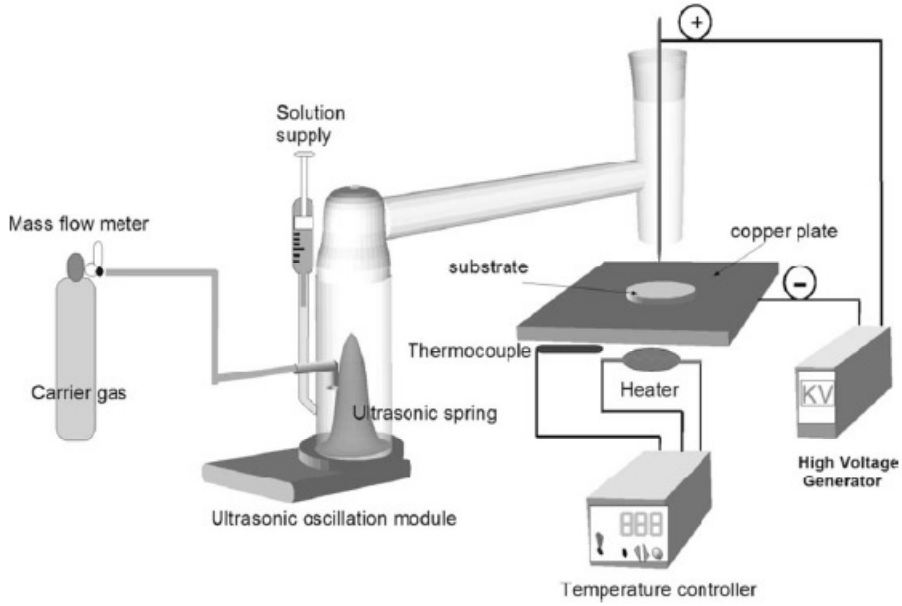

Figure 22. Electrostatic-assisted ultrasonic spray pyrolysis schematic [58].

3.2.4 Vapor Deposition Techniques

Vapor deposition techniques, including chemical vapor deposition and physical vapor deposition, are costly, slow, delicate, and complicated. This makes them undesirable and will not be explored further here [51]; although, they do produce high purity structures. Functionally graded cathodes have been achieved with combustion chemical vapor deposition [59].

3.3 Comparison of Techniques for Graded Electrode Structure Fabrication

Wet ceramic techniques are considered first. A typical electrode shows good performance at a thickness of about 50 µm [53]. Tape casting and screen printing at best are able to deposit layers 7-8 µm thick. This would allow for ~7 layers to vary the structure throughout the electrode. After each layer is deposited, drying time is required, which can take more than a day. Spin coating can produce adequately thin layers to closely approximate a continuously varied structure but still requires drying time between each layer. The thinner the layers, the more of them are needed to make the full thickness of ~50 µm. This results in large amounts of time needed for drying. Since tape calendaring can only be used with tape casting and screen printing and these methods cannot produce thin enough structures for a graded electrode, it is difficult to fabricate continuously graded electrodes. Extrusion fabrication techniques cannot be used to make functionally graded electrodes, but are very good for making a structured substrate to deposit other cell components onto.

After the wet ceramics are deposited they must be sintered. A full day is needed to slowly ramp up and sinter the ceramic at the high temperatures required. Usually more than one sintering step is needed because all cell components do not sinter at the same temperature. If the proper binders are not used the green ceramic will crack before or during sintering. Sintering occurs between 1000 °C and 1600 °C for anode structures [28, 30]. Ramp rates can be 5 °C/min [28, 30]. The spray fabrication techniques are evaluated next.

Plasma spraying is a fast and well-known technique for making thin layers and coatings. It can easily produce graded structures by changing the feed material and can easily be scaled [51]. It is still left wanting when producing SOFC electrodes. It produces porosities of 15% under standard operating conditions and 20% when pore formers are added to the feed stock material [51]. High performance electrodes require ~30% porosity. Plasma spraying also results in lower conductivity due to its pancake splat-like structure [60].

ESD and MSP can easily use a wide variety of inorganic solutions and deposit them onto a heated substrate. These techniques are similar, in that, atomized solution droplets are deposited on a heated substrate. Typically ESD deposition rates are very slow and can take hours to deposit, which is similar to vapor deposition techniques. For thicker structures, ESD will form a columnar or patterned structure [53, 61]. This structure is characteristic of the

technique and can lead to poor conduction through the electrode. It also can lead to mechanical failure issues due to non-uniformity. Although ESD can make continuously graded electrodes, it does not lend itself to high volume manufacture because of its high time cost. Mist spray pyrolysis, just as the other spray techniques, can make a continuously graded structure. As mentioned before, it can create porous structures up to 55%. Only a precursor solution is needed as the feed stock, as opposed to plasma and wet ceramic processing techniques needing a powder feed stock to operate. Deposition times are measured in minutes instead of hours, if controlled properly. An electrode deposited by MSP can be used as deposited, although the conductivity can be improved by calcinating or annealing the electrode [62]. Calcination is very similar to sintering, but the ramp rate can be higher, peak temperature is lower, and the duration at that temperature is shorter.

Currently, there is no clear winner for the fabrication of graded SOFC electrodes. In this review, MSP seems to be a good process candidate when structure grading is needed. Porosity can be graded by changing the substrate temperature, solution concentration, and carrier gas velocity during deposition, while the composition can be graded by mixing two atomized solutions in gas at the proper ratio before being deposited on the heated substrate. The particle size can be graded by varying the solution concentration and the ultrasonic atomizer's frequency. Table 1 shows a summary of the previous discussion. MSP is highlighted as an appropriate fabrication technique for making continuous functionally graded electrodes for SOFCs. Tape calendaring received a lower rating by default since it is a process that sequentially follows tape casting and screen printing. It also received a N/A rating for porosity since the percent porosity does not depend on the calendaring technique.

Table 1. Summary of comparison of SOFC fabrication techniques for graded structures.

Fabrication Technique	Grading capability	Cost (time/complexity)	Porosity	Thickness
Tape casting	Poor	High	0-60	>7 µm
Screen printing	Poor	High	0-60	>8 µm
Dip coating	Poor	High	0-60	>10 µm
Spin coating	Yes	High	0-60	>1 µm
Extrusion casting	No	Low	0-60	N/A
Tape calendaring	Poor	Low	N/A	N/A
Plasma spray	Yes	Low	5-20	>Particle size
Electrostatic spray deposition	Yes	High	0-60	>Particle size
Ultrasonic mist spray pyrolysis	Yes	Medium	0-55	>Particle size

3.5 Material Incompatibility Issues

Material compatibility is an important property for SOFC components. Most of the issues that arise are due to the materials being in contact at high temperatures encountered during sintering.

Table 2 shows common incompatibilities between materials. One of interest is YSZ with doped ceria materials. Ceria is known to be a good ion conductor and even a mixed conductor under low oxygen partial pressures [63]. To avoid the detrimental reaction product, a quick heating process (to limit material diffusion and reaction) can be used, such as plasma spraying; a lower temperature process, such as mist spray pyrolysis; or the incompatible materials can be avoided altogether.

Table 2. SOFC electrolyte material incompatibilities [27].

Electrolyte	Incompatibilities	Forms	Solution	References
YSZ	LSCF, LSM	$SrZrO_3$	Interlayer of GDC, keep below 1200 °C	[1]
	$LaMO_3$-based (M = Mg, Mn, Fe, Co)	$La_2Zr_2O_7$	Interlayer of GDC or SDC, keep below 1200 °C (1000 °C if M=Co)	[37,43–45]
	Doped ceria above 1300 °C	$Y_{.2}Ce$—$Y_{.15}Zr$	Keep cell below 1300 °C	[46,47]
	$LnSrO_3$-based (Ln = Pr, Nd, Gd)	$Ln_2Zr_2O_7$, $SrZrO_3$	Sinter at 1000 °C for 100 h	[48,49]
LSGMC, LSGMF, and LSGMCF	Ni—O	Nickel diffusion	Interlayer of GDC of SDC	[1,34,33,50]
	Itself or LSM (inconclusive)	$SrGaO_3$, La_4SrO_7, $LaSrGaO_4$, $LaSrGa_3O_7$, $SrLaGa_3O_7$, $La_4Ga_2O_9$	Control Sr/Mg ratios	[37,26]
	LSC	Cobalt diffusion	Protective Interlayer	[51]

CHAPTER 4. MODELING OF SOFC

Nomenclature

A	Contact/reaction area per volume, m^2/m^3
d	Pore diameter, m
D	Diffusion coefficient, mol/m^2s
F	Faraday's constant, C/mol
g	Gibbs free energy, J/mol
i	Current density, A/m^2
i_n	Charge transfer current, A/m^2
i_o	Exchange current density, A/m^2
I_t	Total current, A/m^2
J	Molar flux, $mol/(m^2s)$
l	Electrode thickness, m
M	Molecular weight, g/mol
n_e	Number of electrons in reaction, unitless
n	Number fraction, unitless
n_{star}	Number of particle per volume, $\#/m^3$
p	Pressure, Pa
P	Total pressure, Pa
pr	Probability, unitless
r	Particle radius, m
$\bar{r}$	Pore radius, m
R_g	Gas constant, J/mol-K
R_P	Ratio of particle radii, unitless
T	Temperature, K
V	Voltage, V
Z	Coordination number, unitless

Greek

ε	Porosity, unitless
σ	Collision diameter, Å
β	Charge transfer coefficient, unitless
τ	Tortuosity, unitless
γ	Particle necking factor, unitless
ρ	Resistivity, ohm-m
φ	Volume fraction, unitless
θ	Contact angle, radians
Ω	Collision integral

Subscript

a	Anode
A	Specie A
act	Activation
B	Specie B
c	Cathode
$conc$	Concentration
cr	Critical
eff	Effective
el	Electronic
f	Free surface
i	Electrode-electrolyte interface
oc	Open circuit
ohm	Ohmic
H_2	Hydrogen
H_2O	Water
io	Ionic
K	Knudsen
O_2	Oxygen

Superscript

i	Inlet

This SOFC model integrates two models: a macro model and a micro model. The SOFC macro model describes the overall cell behavior with thermodynamic and voltage efficiencies; by considering mass transfer, Ohmic, and activation losses based on chemical and concentration potentials. The micro model describes electrode conductivity and pore size as a function of electrode geometry, microstructure, and physical properties, including particle radii, porosity, contact angle, exchange current, reactant gas pressure, and material

composition. The micro model data are then combined with the macro model. From this compilation, an all encompassing model is developed.

4.1 Model Review

4.1.1 Macro Model Review

A SOFC macro model considers the open circuit voltage (OCV), activation losses, Ohmic losses, and concentration (diffusion) losses. All macro models use the Butler-Volmer rate equation for activation losses, a bulk diffusion and Knudsen diffusion theory for concentration losses, and Ohm's law for Ohmic losses in the electrolyte. The output voltage relationship can be seen in Eqn. (4). See Figure 6 for output voltage verses current density behavior in terms of voltage losses.

$$V_{out} = V_{oc} - \left(\overbrace{V_{act} + V_{Ohmic} + V_{conc}}^{V_{loss}} \right) \tag{4}$$

The parameters most often fitted are the exchange current density in the activation losses and the tortuosity in the diffusion losses. Some papers use multiple fitting parameters to match experimental data. For example, Kim et al used five fitting parameters [64]. Of the five fitting parameters, two were used for fitting the activation loss behavior; two were used for fitting diffusion loss behavior, and one for the ohmic losses. This allows a curve to be fitted very closely to experimental data, but cannot be used to predict cell performance. Kim et al and other researchers use the Tafel approximation of the Butler-Volmer equation, which uses two fitting parameters instead of one in the original equation [65].

The Ohmic losses are calculated based on assumptions for the porous anode and cathode [66] or are ignored [67], as their conductivities are much higher compared to the electrolyte.

The biggest difference among present macro models is in the accounting of diffusion through the electrodes. Ni et al, Hussain et al, and Greene et al used a modified Stefan-Maxell based calculation [68]. Ni et al used the Dusty Gas Model, which accounted for simple molecular and Knudsen diffusions [16]. The simple molecular diffusion works based

on concentration gradients and ignores what the gas species is diffusing through. Hussain et al used a modified Stefan-Maxwell diffusion theory and Knudsen diffusion, but did not specify which bulk diffusion theory was used [69]. Deseure et al used the Homogeneous Flooded Model [66]. This model assumes the diffusing gas partial pressure is uniform. This assumption is only applicable to sufficiently thin electrodes. Lee et al, Chan et al, and Greene et al used a binary diffusion theory and Knudsen diffusion. Greene et al used the Mean Transport Pore Model, which accounted for Knudsen and simple molecular diffusion with the Stefan-Maxwell calculation [19]. Lee et al used Fuller diffusion, while Chan et al used the Chapman-Enskog prediction theory to account for binary diffusion [67, 70].

Many of the diffusion theories presented here appear to only have accounted for simple diffusion when the electrode system is truly a binary diffusion system. The Stefan-Maxwell relation can be used for multi-component gas mixtures and can be difficult to calculate [68]. Chan et al's model was chosen for its simplicity and true accounting for binary diffusion. This model used the Chapman-Enskog prediction theory in conjunction with Knudsen diffusion.

4.1.2 Micro Model Review

A SOFC micro model considers parameters such as porosity percent, particle size, particle coordination number, electronic-ionic conductor size ratio, electronic-ionic conductor particle number fraction, and bulk material conductivities. The model then outputs effective conductivities and pore size.

A commonly used percolation model was proposed by Bouvard [71] and was developed further by Costamagna et al [72]. It is based on the concept of randomly packed spheres that are slightly intersecting. This model has been used in varying degrees by other researchers [16, 69-70, 73-74]. Ni el al, Chan et al, Hussain et al, and Costamagna et al share the same definition for the effective triple boundary phase (TPB) area. Mori's model does not utilize units but a TPB length index L_{TPB}. Nam et al uses a similar equation to quantify the TPB, but uses a length unit. In Nam's formula the arc length of intersecting spheres is used instead of the intersection area of two spheres. This change is understandable because the TPB area quantity used in Costamagna's model is not necessarily the actual TPB area. To

accurately quantify the TPB (length/area/volume) surface diffusion and reaction kinetics need to be addressed, which add great complexity to the model. Some researchers have investigated this influence [75-77]. The TPB area is by nature difficult to define because the porous structure of an electrode cannot be fabricated in a well ordered or perfectly homogeneous way. It is understandable that one method is not widely agreed upon, although the percolation theory and coordination number theory have been used by all of the researchers mentioned in this paragraph. Since Costamagna et al's model uses the fewest assumptions and has been experimentally validated; it will be used in this work.

4.1.3 Functionally Graded Electrode Model Review

Few models have investigated the influence of graded electrode microstructure on electrical power output. Schneider et al developed a 3-D model of randomly packed spheres and studied the effects of grading the nickel/YSZ ratio through the anode [18]. They concluded that this compositional grading only has limited effects for improving anode performance. This is because the Ohmic losses due to electron and ion percolation are negligible when compared to activation and diffusion losses. For this reason, compositional grading will not be studied in this paper. Deseure et al also studied conducting particle ratio effects, but did so with YSZ/LSM for the cathode [66]. Their conclusions were similar. Compositional ratio grading slightly improved performance due to increase percolation and that porosity grading also increases performance while reducing the number of reactions sites available. Greene et al developed a model with functionally graded electrodes while using carbon monoxide and diluted hydrogen as fuels [19]. They found that high porosity near the electrolyte increases the efficiency of the water shift reaction, resulting in increased performance. The only complete model found that has studied FGEs was developed by Ni et al [16]. They studied linearly graded porosity and particle size through various cathodes and anodes. They concluded that particle size grading is more effective at increasing power performance than porosity grading; this is because particle size grading decreases activation and diffusion losses, while porosity grading only reduces diffusion losses greater than it increases activation losses.

4.2 Developed Model

4.2.1 Developed Macro Model

Macro model behavior is determined by Eqn. (4). The voltage losses are subtracted from the open-circuit voltage, which results in the characteristic voltage-current curve seen in Figure 6. The three losses are activation, Ohmic, and concentration. They are defined in Section 2.2.

The macro used is based on a model developed by Chan et al [70, 78]. The basic equations that are used in macro modeling are shared among many research papers [19, 79-80]. The Nernst potential is used to calculate the open-circuit voltage of SOFCs and can be seen in Eqn. (5). As described previously, the Nernst potential is the ideal OCV a cell can obtain and decreases with increasing temperature.

$$V_{oc} = \frac{-\Delta g}{n_e F} + \frac{R_g T}{n_e F} \ln\left(\frac{p_{H_2}\sqrt{p_{O_2}}}{p_{H_2O}}\right) \tag{5}$$

To create the typical system performance voltage vs. current curve, all losses are then subtracted from the OCV. The losses are defined by Eqn. (6). All electrochemical systems have an equilibrium state that is used as a reference point for reaction behavior. The three losses mentioned above are seen when operating in non-equilibrium.

$$V_{loss} = \left(V_{el(eq)} - V_{io(eq)}\right) - \left(V_{el} - V_{io}\right) \tag{6}$$

Eqn. (7) shows the Butler-Volmer equation which is commonly used to describe the activation polarization that occurs in a cell. The transfer coefficient β is typically 0.5. Activation losses are due to the potential needed to cause charge transfer and is dependent on reactant concentration, material, temperature, and surface properties. As a side note $n = 1$ in this equation system even though there are 2 electrons transferred during the overall formation of water reaction from oxygen and hydrogen ions [81-82]. This is because the formation of water reaction is a multi-step reaction, and the Butler-Volmer equation is a rate determining equation. Researchers have found that when $n = 1$ the model better fits experimental data. The reaction mechanisms are not fully understood.

$$i_n = i_o \left\{ exp\left(\frac{\beta n F V_{loss}}{R_g T}\right) - exp\left(-(1-\beta)\frac{n F V_{loss}}{R_g T}\right)\right\} \quad (7)$$

The Ohmic losses through SOFCs are calculated with Ohm's law, using ionic and electronic resistance values, as seen in Eqn. (8). *R* values are difficult to estimate accurately in a porous electrode structure, as it depends on conduction path length. Therefore this equation cannot be easily used. Eqn. (9) and (10) are Ohm's law for the electronic and ionic conductors in an electrode.

$$V_{ohmic} = iR \quad (8)$$

$$\frac{dV_{el}}{dx} = \rho_{el(eff)} i_{el} \quad (9)$$

$$\frac{dV_{io}}{dx} = \rho_{io(eff)} i_{io} \quad (10)$$

The current balance in the electronic and ionic conductors can be seen in Eqn. (12). The first and second derivatives of Eqn. (6) can be seen in Eqn. (13) and (14) with the use of Eqn. (9), (10), and (11).

$$\frac{di_{el}}{dx} = -Ai_n \quad (11)$$

$$-\frac{di_{el}}{dx} = \frac{di_{io}}{dx} \quad (12)$$

$$\frac{dV_{loss}}{dx} = -\left(\frac{dV_{el}}{dx} - \frac{dV_{io}}{dx}\right) = \rho_{io(eff)} i_{io} - \rho_{el(eff)} i_{el} \quad (13)$$

$$\frac{d^2 V_{loss}}{dx^2} = \rho_{io(eff)} \frac{di_{io}}{dx} - \rho_{el(eff)} \frac{di_{el}}{dx} = \left(\rho_{el(eff)} + \rho_{io(eff)}\right) A i_n \quad (14)$$

The concentration losses or mass transfer losses can be calculated using Eqn. (15), which requires Eqn. (16) and (17). This calculation approach only works for a homogeneous

electrode. It assumes that all of the chemical reactions are happening at the electrode-electrolyte interface. Eqn. (15) is a Nernst potential.

$$V_{conc} = -\frac{R_g T}{nF} \ln\left(\frac{p_{r,H_2} p_{H_2O}}{p_{H_2} p_{r,H_2O}}\right) \tag{15}$$

$$p_{r,H_2} = p_{H_2}^i - \frac{RTl_a i}{nFD_{a(eff)}} \tag{16}$$

$$p_{r,H_2O} = p_{H_2O}^i + \frac{RTl_a i}{nFD_{a(eff)}} \tag{17}$$

The basis for the above equations comes from Fickian diffusion, Eqn. (18), combined with the flux of electrons through the electrode Eqn. (19), results in Eqn. (20). This equation is true for all depths throughout the electrode and can account for hydrogen consumption throughout the electrode when combined with the Butler-Volmer equation.

$$J = D_{eff} \frac{dP}{(RT)dx} \tag{18}$$

$$J = \frac{i}{2F} \tag{19}$$

$$\frac{dp_{H_2}}{dx} = -\frac{RTi}{nFD_{(eff)}} \tag{20}$$

$D_{(eff)}$ can be found by considering binary and Knudsen diffusion types. Binary diffusion occurs where molecular-molecular interactions are dominant, and Knudsen diffusion occurs where molecular-surface interactions are dominant. The binary diffusion coefficient can be calculated with the Chapman-Enskog theory, as seen in Eqn. (21) and (22) [78]. σ_{AB} is the collision diameter and Ω_{DAB} is the collision integral based on the Lennard-Jones potential. The collision integral can be found with Eqn. (22). M_{H_2} and M_{H_2O} are the molecular weight of hydrogen and water. p is the total pressure in atm. The average energy well depth is calculated with $\epsilon_{H_2-H_2O} = \left(\epsilon_{H_2}\epsilon_{H_2O}\right)^{0.5}$ in ergs. ϵ_{H_2} and ϵ_{H_2O} are found from

the viscosity of the gas [83]. The average collision diameter is calculated with $\sigma_{H_2-H_2O} = \frac{\sigma_{H_2}+\sigma_{H_2O}}{2}$. σ_{H_2} and σ_{H_2O} are the collision diameters of the specie molecules in angstroms [84].

$$D_{H_2-H_2O} = 0.0018583\left(\frac{1}{M_{H_2}}+\frac{1}{M_{H_2O}}\right)^{\frac{1}{2}}\frac{T^{1.5}}{p\sigma_{H_2-H_2O}^2\Omega_{\mathrm{D},H_2-H_2O}} \tag{21}$$

$$\Omega_{\mathrm{D},H_2-H_2O} = \frac{\mathrm{A}}{(\mathrm{T}^*)^{\mathrm{B}}}+\frac{\mathrm{C}}{\exp(\mathrm{DT}^*)}+\frac{\mathrm{E}}{\exp(\mathrm{FT}^*)}+\frac{\mathrm{G}}{\exp(\mathrm{HT}^*)} \tag{22}$$

$$\text{Where, } \mathrm{T}^* = \frac{\mathrm{kT}}{\epsilon_{H_2-H_2O}} \quad \text{A=1.06036} \quad \text{B=0.15610} \quad \text{C=0.19300}$$

$$\text{D=0.47635} \quad \text{E=1.03587} \quad \text{F=1.52996} \quad \text{G=1.76474} \quad \text{H=3.89411}$$

Knudsen diffusion conditions occur where the pore diameter is approximately 50 nm. The Knudsen diffusion coefficient can be calculated with Eqn. (23) for gas specie A, where $\bar{r}$ is the radius of the pore.

$$D_{AK} = 97\bar{r}\sqrt{\frac{T}{M_A}} \tag{23}$$

The effective diffusion coefficient can be found with Eqn. (24), where ε and τ represent porosity and tortuosity of the porous structure.

$$D_{A(eff)} = \frac{\varepsilon}{\tau}\left(\frac{1}{D_{AB}}+\frac{1}{D_{AK}}\right)^{-1} \tag{24}$$

Figure 23 shows the effective, binary, and Knudsen diffusion coefficients for hydrogen and water. The effective diffusion varies from Knudsen diffusion dominance at smaller particle sizes to binary diffusion dominance at larger particle sizes.

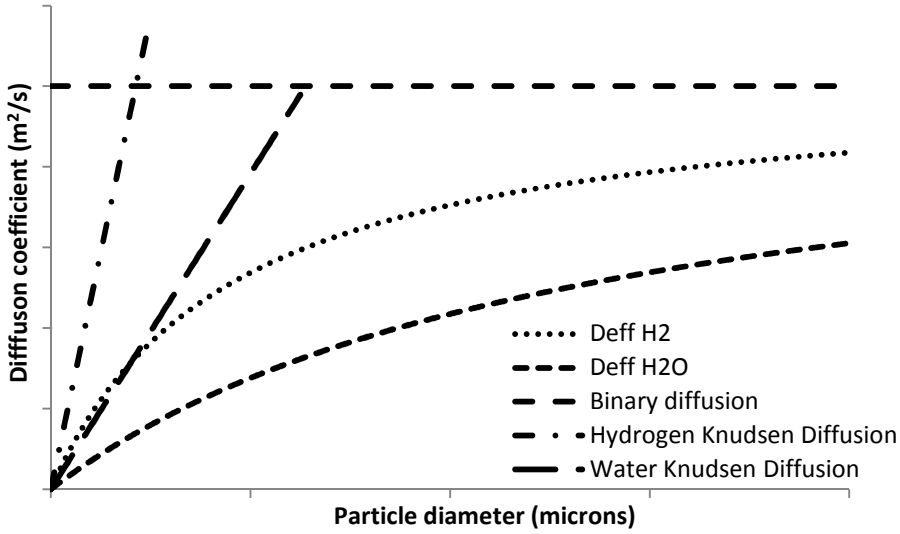

Figure 23. Diffusion coefficients verses particle diameter.

4.2.2 Developed Micro Model

Costamagna's model will be utilized in this paper's model development. In this model, the parameter R_P was defined as the ratio of the matrix particle radius to the inclusion particle radius. We will set the ionic conducting particles as the matrix and the electronic conducting particles as the inclusion phase as seen in Eqn. (25).

$$R_P = \frac{r_{io}}{r_{el}} \tag{25}$$

The mixture of binary particles has the following coordination number based on the particle type as seen in Eqn. (26) and (27). The coordination number Z equals 6 in a random packing sphere system, and n_{el} and n_{io} are the number fraction of electronic and ionic conducting particles.

$$Z_{el} = 3 + \frac{Z - 3}{n_{el} + (1 - n_{el}){R_P}^2} \tag{26}$$

$$Z_{io} = 3 + \frac{(Z - 3){R_P}^2}{n_{io} + (1 - n_{io}){R_P}^2} \tag{27}$$

The volume fraction can be found from the R_P ratio and the number fraction of conducting particles of that phase as seen in Eqn. (28) and (29).

$$\varphi_{el} = \frac{n_{el}}{(1 - n_{el}){R_P}^3 + n_{el}} \tag{28}$$

$$\varphi_{io} = \frac{n_{io}}{(1 - n_{io}){R_P}^{-3} + n_{io}} \tag{29}$$

The chance of electrical or ionic percolation occurring is based upon the probability of a continuous cluster of conducting particles from the electrolyte to the electrode free surface existing in the electrode. Costamagna et al used Eqn. (30), developed by Bouvard, modifying the coefficients based on the experimental determination of $Z_{m\text{-}m}$=1.764 by Kuo et al [85]. Subscript *m* denotes the particle conducting phase.

$$pr_m = \left(1 - \left(\frac{4.236 - Z_{m-m}}{2.472}\right)^{2.5}\right)^{0.4} \tag{30}$$

Kuo et al showed that when R_P<1, Bouvard's model deviates from experimental results. It was shown that Suzuki's model was accurate for 0.154<R_P<6.464. Suzuki's model utilized Eqn. (31) and (32) [86].

$$Z_{el-el} = \frac{n_{el}Z}{n_{el} + (1 - n_{el}){R_P}^2} \tag{31}$$

$$Z_{io-io} = \frac{n_{io}Z}{n_{io} + (1 - n_{io}){R_P}^{-2}} \tag{32}$$

The number of particles per unit volume can be calculated with Eqn. (33). Eqn. (33) and (34) are used when R_P>1.

$$n_{star} = \frac{1 - \varepsilon}{\frac{4}{3}\pi r_{el}^3 (n_{el} + (1 - n_{el}){R_P}^3} \tag{33}$$

The area of contact between the spheres per volume can be calculated with Eqn. (34). θ is the contact angle of the smaller particle.

$$A = \frac{\pi(r_{el}\sin(\theta_{el}))^2 n_{star} n_{el} n_{io} Z_{el} Z_{io} p_{el} p_{io}}{Z} \tag{34}$$

If R_P<1, then Eqn. (35) and (36) should be utilized. Notice θ is based on the smaller particle. If R_P=1, then either equation set can be used.

$$n_{star} = \frac{1-\varepsilon}{\frac{4}{3}\pi r_{io}^3 (n_{io} + (1-n_{io}){R_P}^{-3}} \tag{35}$$

$$A = \frac{\pi(r_{io}\,sin(\theta_{io}))^2 n_{star} n_{el} n_{io} Z_{el} Z_{io} p_{el} p_{io}}{Z} \tag{36}$$

Ni et al calculate an effective resistivity based on tortuosity, porosity, volume fraction of the conducting phase, and the bulk material conductivity [16]. That equation was developed from Hussain et al and Deseure et al [66, 69] and does not agree with the following experimentally proven percolation theory, but this discrepancy will not be discussed here.

The effective resistivity can be calculated by using Eqn. (37) and (38), rewritten from Costamagna [72]. γ is an adjustable parameter that accounts for the affect the necks between the particles have on conductivity. Costamagna used γ=0.5. The critical number fraction is found from percolation theory critical thresholds.

$$\rho_{el,eff} = \frac{(1-n_{el,cr})^2}{\gamma\sigma_{el}{(n_{el}-n_{el,cr})}^2} \tag{37}$$

$$\rho_{io,eff} = \frac{(1-n_{io,cr})^2}{\gamma\sigma_{io}{(n_{io}-n_{io,cr})}^2} \tag{38}$$

Pore diameter can be calculated from Eqn. (39) [73]. When $R_p = 1$, Eqn. (39) reduces to Eqn. (40), which was used by Ni et al [17].

$$d_{pore} = \frac{2}{3}\frac{d_{el}\varepsilon}{(1-\varepsilon)}\left(\frac{n_{el}+(1-n_{el})R_p^3}{n_{el}+(1-n_{el})R_p^2}\right) \tag{39}$$

$$d_{pore} = \frac{2}{3}\frac{d_{el}\varepsilon}{(1-\varepsilon)} \tag{40}$$

4.3 Model Integration

Model integration was done by putting the anode and cathode resistivity values from the micro model directly into the macro model. The electrolyte resistance can be simply calculated from bulk YSZ ionic resistances and known material thickness. The only parameters for fitting a experimental data curve would be the contact angle of the smaller conducting phase particle, particle-to-particle necking factor γ, and the exchange current density.

Eqn. (41), (42), and (43) make up the system of coupled differential equations that is used for the anode. The anode operates under countercurrent diffusion. These are combined from Eqn. (7), (11), (14), and (20).

$$\frac{d^2V_{loss}}{dx^2} = \left(\rho_{el,eff}+\rho_{io,eff}\right)Ai_o\left[\frac{p_{r,H_2}}{p_{H_2}^i}exp\left(\frac{\beta nFV_{loss}}{RT}\right) - \frac{p_a - p_{r,H_2}}{p_a - p_{H_2}^i}exp\left(-(1-\beta)\frac{nFV_{loss}}{RT}\right)\right] \tag{41}$$

$$\frac{dp_{r,H_2}}{dx} = -\frac{RT}{2F}\frac{i_{el}}{\left(1-\frac{p_{r,H_2}}{p_a}\right)D_{H_2(eff)} + \left(\frac{p_{r,H_2}}{p_a}\right)D_{H_2O(eff)}} \tag{42}$$

$$\frac{di_{el}}{dx} = -Ai_o\left[\frac{p_{r,H_2}}{p_{H_2}^i}exp\left(\frac{\beta nFV_{loss}}{RT}\right) - \frac{p_a - p_{r,H_2}}{p_a - p_{H_2}^i}exp\left(-(1-\beta)\frac{nFV_{loss}}{RT}\right)\right] \tag{43}$$

Eqn. (44), (45), and (46) are the coupled differential equation system that is used for the cathode. The cathode operates under self-diffusion.

$$\frac{d^2V_{loss}}{dx^2} = \left(\rho_{el,eff}+\rho_{io,eff}\right)Ai_o\left[\frac{p_{r,O_2}}{p_{O_2}^i}exp\left(\frac{\beta nFV_{loss}}{RT}\right) - exp\left(-(1-\beta)\frac{nFV_{loss}}{RT}\right)\right] \tag{44}$$

$$\frac{dp_{r,O_2}}{dx} = -\frac{RT}{4F}\frac{i_{el}}{D_{O_2(eff)}}\left(\frac{p_c - \delta p_{r,O_2}}{p_c}\right) \quad (45)$$

Where, $\delta = \frac{D_{O_2,K(eff)}}{D_{O_2,K(eff)+D_{O_2-N_2(eff)}}}$

$$\frac{di_{el}}{dx} = -Ai_o\left[\frac{p_{r,O_2}}{p^i_{O_2}} exp\left(\frac{\beta nFV_{loss}}{RT}\right) - exp\left(-(1-\beta)\frac{nFV_{loss}}{RT}\right)\right] \quad (46)$$

The anode and cathode equation systems used the boundary conditions seen in Table 3.

Table 3. Boundary conditions for the anode and cathode equation systems.

$x = 0$	$\frac{dV_{loss}}{dx} = \rho_{el,eff} I_t$	$i_{el} = I_t$	$p_{r,H_2} = p^i_{H_2}$
$x = l$	$\frac{dV_{loss}}{dx} = \rho_{io,eff} I_t$		

4.4 Complete SOFC Electrode Model with Functional Grading

Two types of grading were considered in this work; particle size grading and porosity grading. The following sections show how the grading profiles were develop and varied and how these profiles influence electrode structure, and therefore power output.

4.4.1 Model Assumptions and Limitations

The micro model gives overall electrode properties based on micro-scale geometry and binary mixture sphere packing theory.

Assumptions of the model are:

1. Steady state conditions.
2. Temperature is uniform throughout the electrode.
3. Hydrogen and oxygen are the reactants on the cell.
4. The conducting phases are continuous and homogeneous in size and distribution.
5. The diffusion coefficients are constant for varying partial pressures.
6. The sum of electronic and ionic current equals total current for all electrode depths.
7. This model cannot account for mixed electronic-ionic conductivity materials.

8. The effect of partial pressure on exchange current density is neglected.

4.4.2 Particle Size and Porosity Grading Profiles

Particle size grading changes the macro and micro model outputs. The reaction surface area is a micro model output parameter and is calculated in Eqn. (34) and (36), and is inversely proportional to particle size. This is then put into Eqn. (41) and (43). The hydrogen and water vapor diffusion coefficients are output parameters of the macro model and are directly proportional to particle size. They depend on pore diameter, which is part of the micro model calculations, as seen in Eqn. (39). Eqn. (47) and (48) show how the concave up and concave down particle profiles were developed, respectively. These equations allow the user to choose the starting and ending value and profile. Figure 24 shows the grading profiles of Eqn. (47) and (48) when shaper factor b = 0.0001 and 0.00001. The top two curves are from Eqn. (47) and the bottom two curves are from Eqn. (48)**.** When b = 1 both equations are linear and have the same solution. The electrode free surface is at x=0 and the electrode-electrolyte interface is on the right. The same equation is used for particle size and porosity grading. See Figure 10 for schematic representations of porosity and particle size grading.

$$d_{part} = \frac{\left(d_f - d_i\right)}{d_f}\left(\frac{(b^2 + lb)d_f}{l(x+b)} + d_f - \left(\frac{d_f(b^2+lb)}{lb}\right)\right) + d_i \qquad (47)$$

$$d_{part} = \frac{\left(d_f - d_i\right)}{d_f}\left(\frac{(b^2 + lb)d_f}{l(x-l-b)} - d_f + \left(\frac{d_f(b^2+lb)}{lb}\right)\right) + d_f \qquad (48)$$

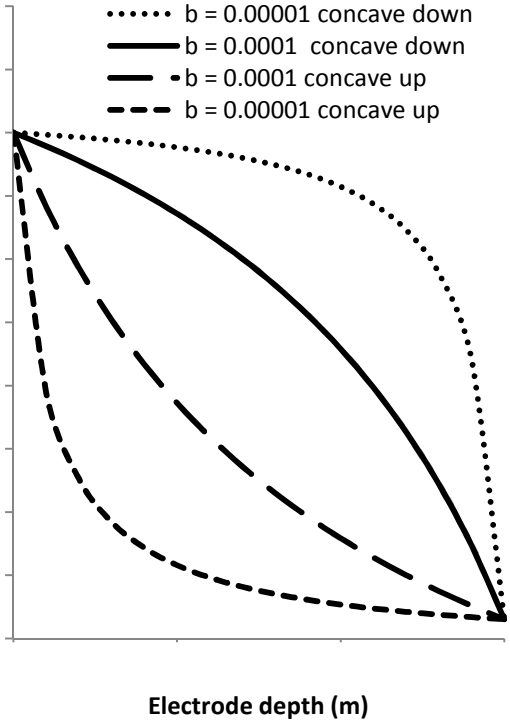

Figure 24. Grading profiles. b=0.0001 for inside curves. b=0.00001 for outside curves.

4.5 Equation System Solver Flow

The equation system presented earlier was solved using MatLab software. An iterative shooting method what used in conjunction with an error minimization function to obtain a system of solutions that included voltage, electronic current, and pressure plots as a function of electrode depth. Since Eqn. (41) is a second-order equation, it was broken into a system of two first-order equations before the overall system was entered into the MatLab code.

The solver flow schematic can be seen in Figure 25. The solver requires an initial guess for voltage. The initial guess along with the initial conditions are fed to a shooter. The shooter references the equation system, consisting of the macro and micro models, and shoots following the equation system's behavior. After the shooter shoots a solution, the ending values are compared with the boundary conditions at the end of the interval. The error value calculated from the difference squared is then sent to a minimization function. If the error is not within allowable tolerances, 0.01 in this case, the minimization function will

choose a new initial guess. The system will iterate in this way until an error within tolerance is obtained. Once the desired error is obtained, the shooter is used one more time and the solution is output.

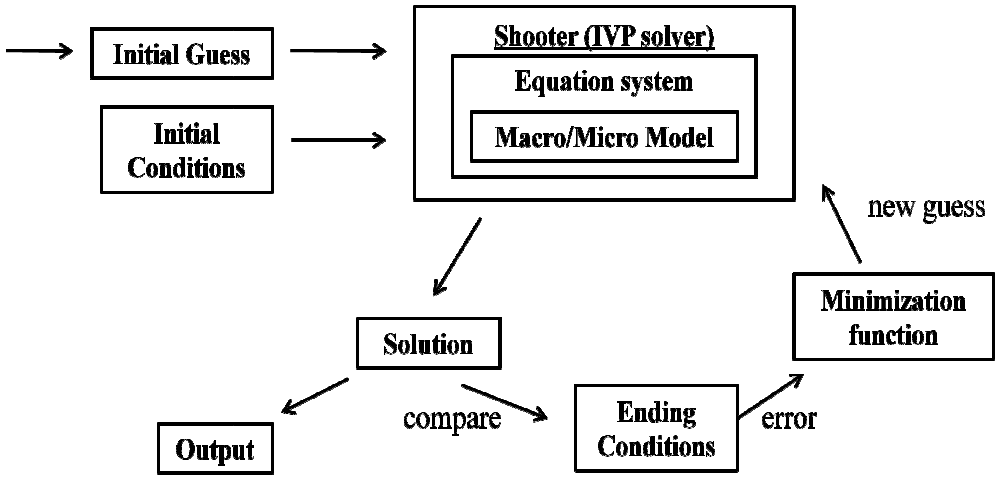

Figure 25. Solver flow schematic.

The homogeneous, particle size, and porosity grading codes execute in very similar ways. They can be found in Appendices A, B, and C, respectively.

CHAPTER 5. MODELING RESULTS & DISCUSSION

5.1 Model Validation with Literature

The model has been validated against experimental data from Jiang et al for operating temperatures of 1073K and 1173K [87], in Figure 26 and Figure 27. Table 4 and Table 5 show the values used for the model validation. If the value is not referenced, then it came from Jiang et al. The key system parameters needed to run the model were the YSZ and Ni particle sizes, Ni/YSZ volume or number ratio, and temperature. The only fitting parameter used was the exchange current density. The fitted exchange current densities for Figure 26 were 1000 A/m^2 and 2200 A/m^2 for the upper and lower curves, respectively. These values are very similar to experimentally determined exchange current densities of other SOFC anodes [65, 70].

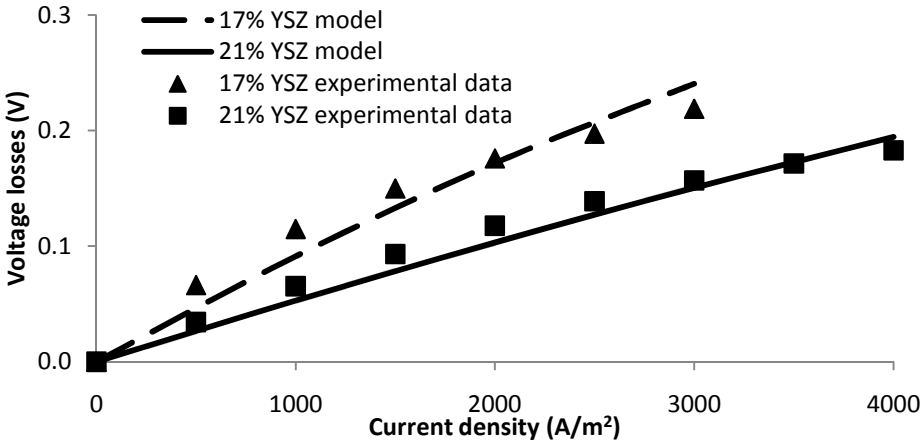

Figure 26. Voltage losses verses current density at 1073K.

Table 4. Model validation parameters at 1073 K.

Model Parameter	Unit	Value
Temperature	K	1073
Fitted anode exchange current	A/m^2	1000/2200
Anode thickness	µm	30
Ni/YSZ volume fraction	unitless	0.83/0.79
Ni/YSZ number fraction	unitless	0.0183/0.0142
Nickel particle diameter	µm	1.6
YSZ particle diameter	nm	250
Porosity	unitless	0.3
Tortuosity	unitless	4.5 [17]
Necking factor	unitless	0.5 [72]
Hydrogen supply pressure	atm	0.97 [70]
Anode electronic conductivity, nickel	S/m	$2x10^6$ [70]
Anode ionic conductivity, YSZ	S/m	$3.44*10^4 exp(-10300/T)$ [88]

The exchange current densities for Figure 27 were 2000 A/m^2 and 6500 A/m^2 for the upper and lower curves, respectively. These values are very similar to experimentally determined exchange current densities of other SOFC anodes [35].

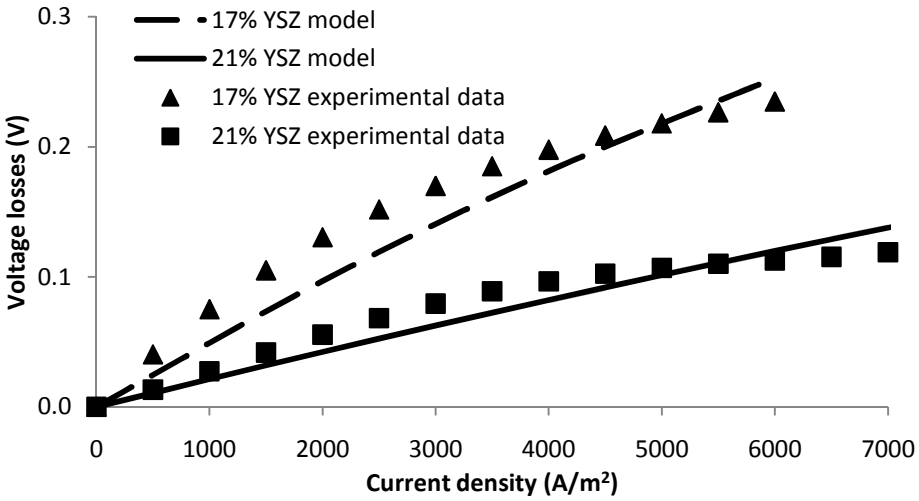

Figure 27. Voltage losses verses current density at 1173K.

Table 5. Model validation parameters at 1173 K.

Model Parameter	Unit	Value
Temperature	K	1173
Fitted anode exchange current	A/m^2	2000/6500
Anode thickness	µm	30
Ni/YSZ volume fraction	unitless	0.83/0.79
Ni/YSZ number fraction	unitless	0.0183/0.0142
Nickel particle diameter	µm	1.6
YSZ particle diameter	nm	250
Porosity	unitless	0.3
Tortuosity	unitless	4.5 [17]
Necking factor	unitless	0.5 [72]
Hydrogen supply pressure	atm	0.97 [70]
Anode electronic conductivity, nickel	S/m	$2x10^6$ [70]
Anode ionic conductivity, YSZ	S/m	$3.44*10^4 exp(-10300/T)$ [88]

5.2 Justification of Model Input Parameters

Fixed model parameters can be seen in Table 6. Tortuosity values were chosen based on Williford et al [75]. This was the only paper found that experimentally determined tortuosity values, and did so with multiple techniques. The anode and cathode exchange currents, as well as the cathode electronic conducting phase (LSM) were taken from Ni et al [16] and is similar to the value used by Costamagna et al [72]. The ionic conductivity for YSZ in this model was taken from Ferguson et al [88]. Ionic conducting media exist in the anode, cathode, and electrolyte. Ionic conductivity is highly dependent on operating temperature. It grows logarithmically as temperature increases, but SOFC life decreases with increasing temperature. Considering these two properties, the operating temperature was chosen to be 1173 K (900 °C). Anode electronic conductivity of nickel, for the anode, was taken from Chan et al [70]. The thin YSZ electrolyte was chosen to be 10 µm, to minimize the losses that were not due to electrode behavior. This helps to see the influences of grading more easily. Moon et al have shown that electrolytes of this thickness are easily fabricated [39]. The water content was chosen to be 15% in the model. In Figure 28, Chan et al showed the voltage losses decrease very little when water content in the hydrogen feed gas is above 15%.

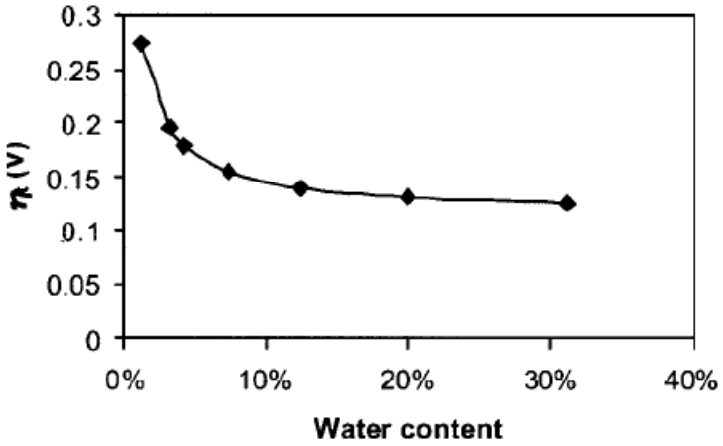

Figure 28. Relationship between water content and polarization (electrode thickness =150 µm, particle diameter = 200nm) [70].

Table 6. Fixed model parameters.

Model Parameter	Unit	Value
Faraday's constant	C/mol	96485
Temperature	K	1173
Electrons in reaction	unitless	1 [81-82]
Gas constant	J/(mol*K)	8.314
Anode exchange current	A/m^2	4000 [17]
Cathode exchange current	A/m^2	1300 [17]
Anode thickness	µm	150
Cathode thickness	µm	30
Electrolyte thickness	µm	10
Porosity	unitless	0.3
Tortuosity	unitless	2.8 [75]
Necking factor	unitless	0.5 [72]
Hydrogen supply pressure	atm	0.85 [70]
Oxygen supply pressure	atm	0.21
Conductor/volume fraction	unitless	0.36
Anode electronic conductivity, Nickel	S/m	$2x10^6$ [70]
Cathode electronic conductivity, YSZ	S/m	10^4 [17, 72]
Anode/Cathode ionic conductivity	S/m	$3.44*10^4\exp(-10300/T)$ [88]

5.3 Analysis of Homogeneous Electrodes

This section will help to understand SOFC electrode behavior. Standard SOFC electrodes have a homogeneous microstructure. Figure 29 shows voltage losses verses electrode particle diameter for cathodes. As the current flow through the electrode increases, so do the voltage losses. This voltage loss increase comes from mass transport losses, which also explains why the minimum voltage is at larger particles sizes for higher current

densities. High current through the electrode is directly related to the number of gas molecules diffusing through the electrode structure. Conduction and activation losses are dominant to the right of the minimum because of fewer contacts for conduction and TPBs for reactions to occur. Diffusion losses are dominant to the left of the minimum voltage because Knudsen diffusion losses increase dramatically at smaller particle sizes.

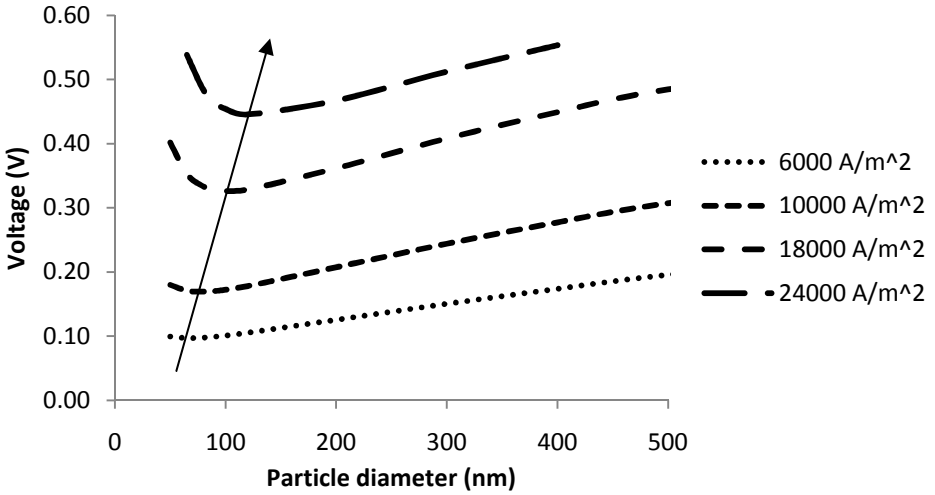

Figure 29. Cathode voltage losses verses particle diameter for varying current densities.

Typical voltage, electronic current, and pressure curves of a homogeneous microstructure are plotted in Figure 30. The voltages losses are due to activation, Ohmic, and diffusion losses; and they are displayed cumulatively. The electronic current is equal to the total current at the anode free surface. At the anode-electrolyte interface, the electronic current is 0 and the ionic current is equal to the total current. The physical flow of oxygen ions and electrons is from the interface to the free surface in the anode. The oxygen ions are formed in the cathode and conducted through the electrolyte and anode. When in the anode, the oxygen ions will react with hydrogen ions in the presence of an electronic conductor. At this point the oxygen ions are essentially converted to electrons. The electrons are conducted out of the anode and used to do electrical work. The pressure drop through a homogeneous electrode is linear until the interface.

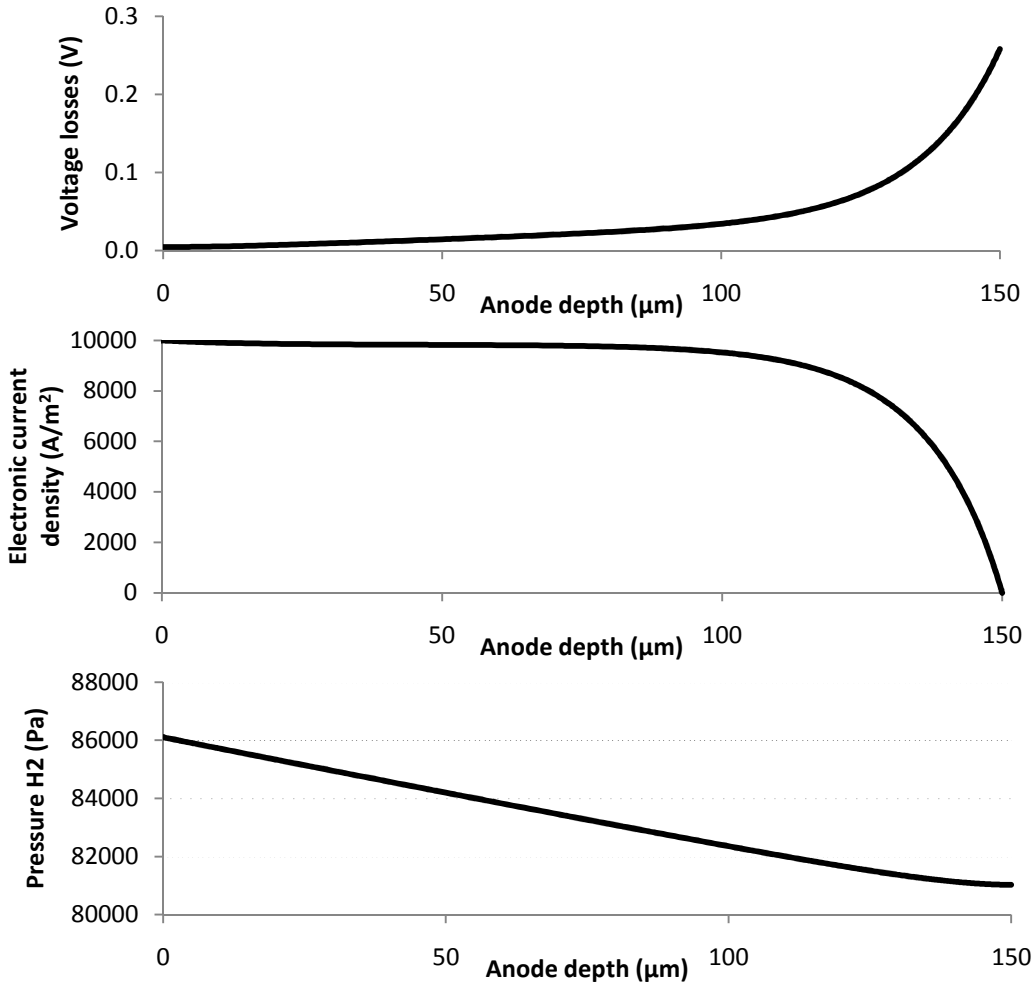

Figure 30. Anode voltage, electronic current, and pressure curves verses depth for homogeneous microstructure. (particle diameter = 1 µm, total current = 10000 A/m^2, electronic number fraction = 0.36)

5.4 Effect of Graded SOFC Electrodes on Power Output

The advantage of a model is to be able to predict cell performance without physical experimentation. This section presents and discusses the effect of (1) using a super-ionic conducting material within an SOFC electrode, (2) linear and nonlinear porosity grading, (3) linear and non linear particle size grading effects on power output, and (4) decision-making criteria of how and when to use particle size grading.

5.4.1 Effect of Linear Particle Size Grading

For this study, the anode and cathode are 150 µm and 30 µm thick, respectively. Figure 31 and Figure 32 show the voltage losses of an anode and cathode with different particle diameters. These two figures are homogeneous structures and will be used for comparison to graded structures later. From these figures, the particle size with the least losses was used to simulate a SOFC system. There are no noticeable diffusion losses in the anode curves. Notice the 65 nm curve for the cathode in Figure 32. After 15000 A/m^2, the diffusion losses become evident by the increased rate of losses when compared with particle diameter.

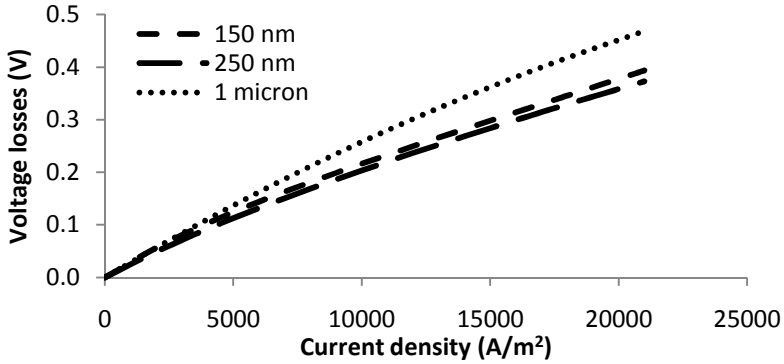

Figure 31. Anode voltage losses verses current density for different particle diameters of a homogeneous anode.

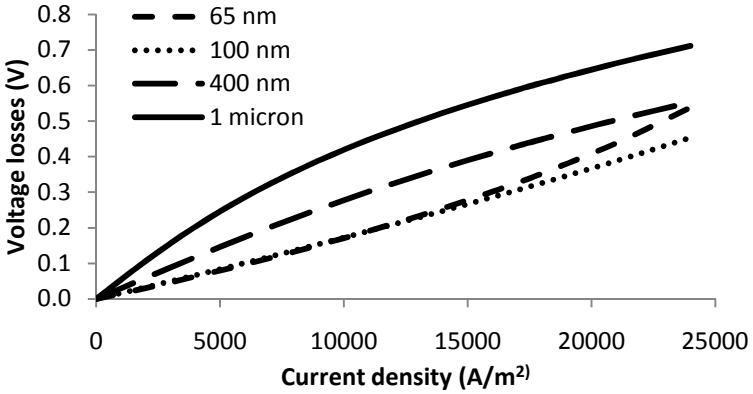

Figure 32. Cathode voltage losses verses current density for different particle diameters of a homogeneous cathode.

Figure 33 shows the voltage and power density curves for an optimized, homogeneous microstructure SOFC. The peak power density is 9600 W/m^2 at 16000 A/m^2 and shows no clear dominance of any one type of polarization/loss. There are no noticeable curvatures in the voltage-current curve. Also notice that for a thinner electrode, the optimal particle size is smaller. Beckel et al showed that a cathode as thin as 500-600 nm can be used when the particle diameter is 35 nm [62].

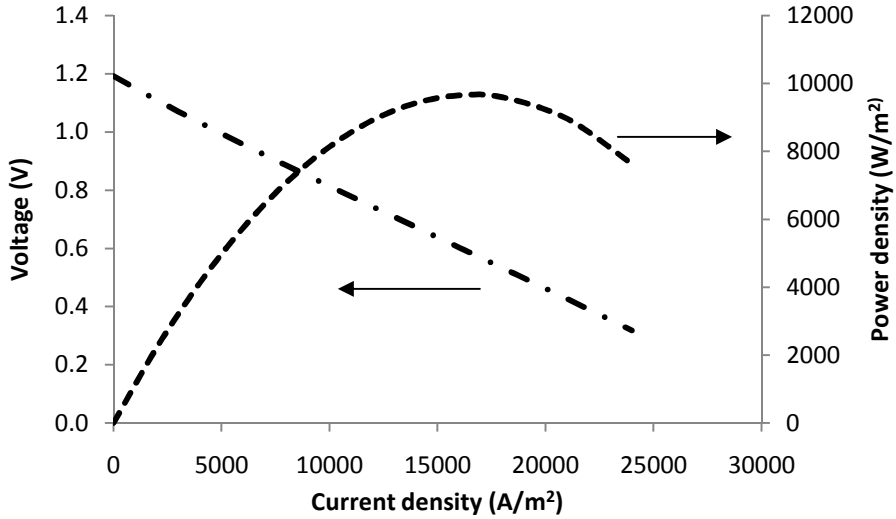

Figure 33. Voltage and power density verses current density for an optimized homogeneous SOFC. (anode particle diameter = 250 nm, cathode particle diameter = 100 nm)

To pick the ideal particle size and range for a linearly graded electrode, the smallest particle diameter was fixed to 50 nm at the electrode-electrolyte interface and then the particle diameter at the electrode's free surface was optimized. The linear grading range that showed the lowest loss for the anode was 50 nm to 5 µm. The linear grading range that showed the lowest loss for the cathode was 50 nm to 500 nm. As seen in Figure 34, the cathode needs more, smaller particles to reduce activation losses. The losses are greater in the cathode because of its 30 µm thickness. If the cathode were made thicker, it would have more reaction sites, reducing the activation losses and therefore the overall losses. Also, there is a very slight "S" shape in the cathode voltage loss curve. The curve at lower current is due to activation and the loss rate increases when diffusion losses become dominant. As can be

seen, the anode losses are reduced by 45% when linear grading in introduced, whereas the cathode losses were reduced by 21% , when comparing Figure 31 and Figure 32 to Figure 34. The anode losses were reduced more easily because the gasses diffusing are smaller molecules, the effective conductivity is higher, and a thicker electrode is easier to optimize for a wider operating current density range.

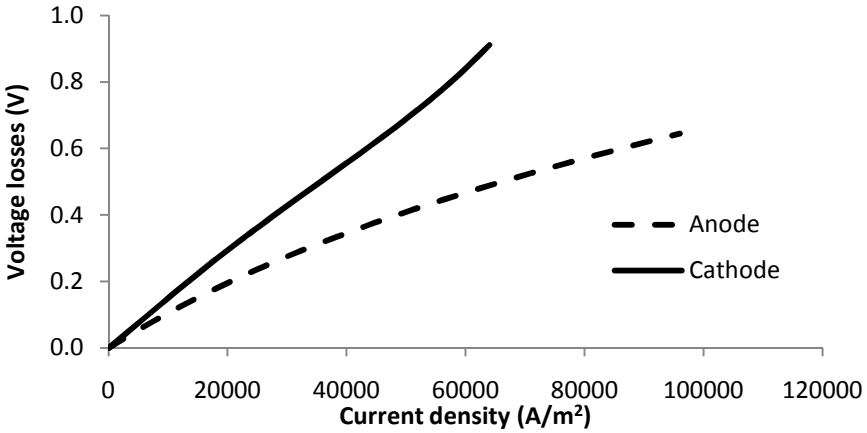

Figure 34. Anode and cathode losses verses current density for linearly graded electrodes. Anode particle diameter ranges from 5 μm to 50 nm. Cathode particle diameter ranges from 500 nm to 50 nm.

Figure 35 shows the voltage and power curves for a SOFC with linearly graded electrodes. The peak power is 14700 W/m^2. This is a 53% improvement over the optimized homogeneous electrodes. This improvement is potentially not the full power increase, since the particle sizes were set at predetermined intervals. If the minimum losses were between the predetermined values, the nearest value was used.

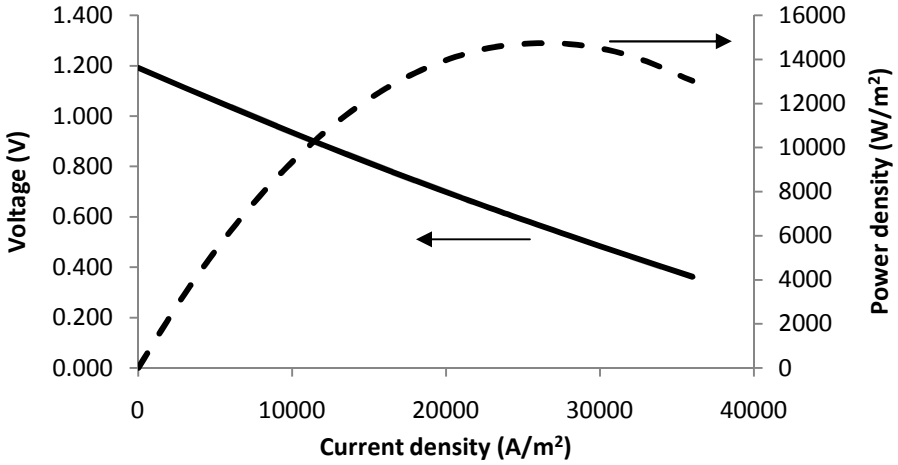

Figure 35. Voltage and power density verses current density for a SOFC with linearly graded electrodes. Anode particle diameter ranges from 5 µm to 50 nm. Cathode particle diameter ranges from 500 nm to 50 nm.

It has been shown here and in literature that linearly grading electrodes in SOFCs can improve power output performance significantly [16]. Fabricating 50 nm particles in a manufacturing setting is difficult. Now we will look at particles sizes that can be considered more realistic for mass production and lifespan, then compare homogeneous, linear, and nonlinear graded structures. The particle diameter at the electrode-electrolyte interface was fixed at 300 nm. Let's call this the 'limited' case. This is larger than the optimal particle diameter for the anode and cathode. Figure 37 show the voltage and power curve with a peak power output of 8300 W/m^2. This power output is actually lower than the optimized homogeneous case when the particle size was not limited, but is more realistic and can be improved upon with particle size grading.

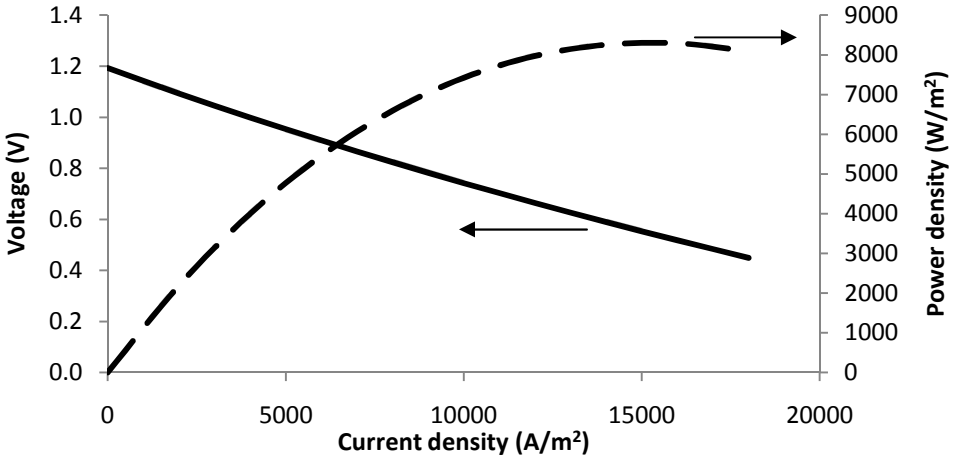

Figure 36. Voltage and power density verses current density. Both electrodes are homogeneous structures with 300 nm diameter particles.

The anode was graded and the optimal range was found to be from 300 nm to 3 µm. To illustrate, Figure 37 shows three linearly particle size graded anode voltage loss curves ranging from 300 nm to 500 nm, 3 microns, and 10 microns at the free surface. As can be seen, the 500 nm and 10 micron curves have higher losses than the 3 micron curve due to diffusion and activation losses, respectively. The activation losses are larger in the 10 micron structure because there is less reaction area, while the diffusion losses are higher in the 500 nm structure. By changing the free surface particle diameter to 3 microns, the diffusion and activation losses are minimized and an overall lower loss curve is achieved. At high current densities, the effect of diffusion losses becomes much more evident in the 500 nm structure. If the graph were extrapolated the 3 micron structure's losses would be greater than the 10 micron structure's losses. These greater losses are not a concern because the cathode losses are much greater than the anode losses, limiting current flow, so the peak power will be realized at ~28000 A/m^2. This means the 3 micron structure will have the lowest losses for the usable current density range.

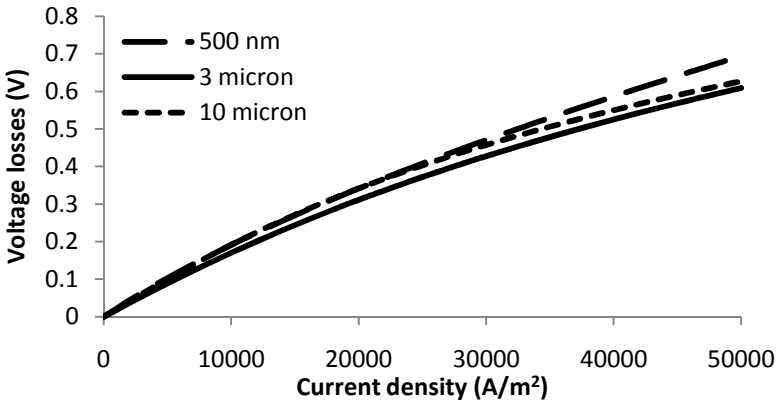

Figure 37. Voltage losses verses current density for three linearly graded anodes. All electrodes have 300 nm diameter particles at the electrolyte interface. The free surface particle diameter is denoted in the legend.

Figure 38 shows the power and voltage curves for a SOFC with a linearly graded anode. The optimal anode from above was used and the optimal cathode was found to be a non-graded/homogeneous particle diameter of 300 nm. The reason for a homogeneous structure being better than a graded structure, in this case, will be discussed later. The peak power is about 8900 W/m^2 with the smallest particle diameter being 300 nm. The linear grading is 7% better than the 'limited' homogeneous electrode case. The performance increase, for the linearly graded SOFC in Figure 38, is due to anode improvements. This shows that it is difficult to improve the performance of a thin electrode (for this study, the cathode), by introducing grading to its structure. In this particular case, the cathode particle size was so large that the dominant losses were all activation and not diffusive. Creating any grading with larger particles would only have been detrimental to the electrode's performance, by increasing activation losses and doing very little to decrease diffusion losses. The anode is relatively thick and therefore can more easily be improved by changing the electrode's microstructure.

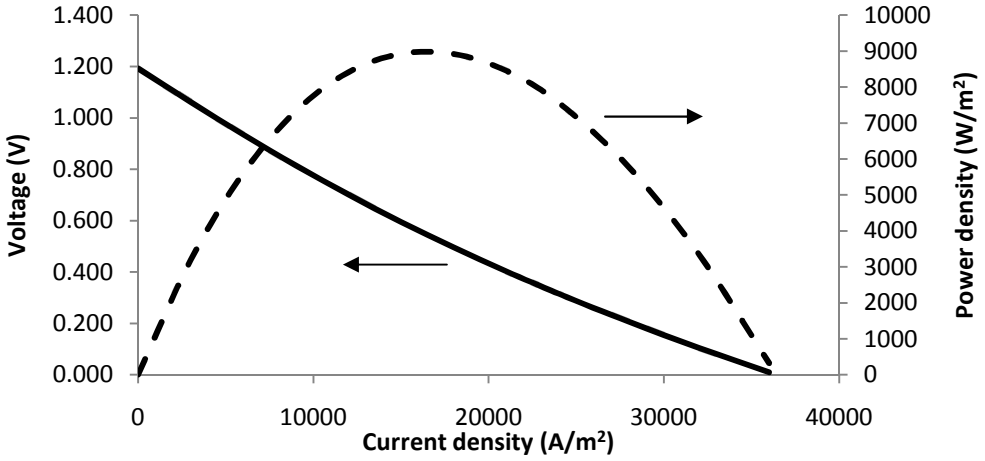

Figure 38. Voltage and power density verses current density for a SOFC with a linearly graded anode. Anode particle diameters are 3 µm to 300 nm. Cathode particle diameter is 300 nm homogeneously.

Nonlinear particle diameter grading will be investigated next. The smallest particle is again kept at 300 nm because of fabrication limitations and ease of comparison. The concave up and concave down terms in Figure 39 refer to the same profile shape with different absolute values as grading profile b = 0.00001 concave up and down in Figure 24. The grading range for the anode in the SOFC system below is from 300 nm to 3 micron diameter; the cathode has homogeneous particles of 300 nm diameter. As can be seen, the linear grading profile is the best. This is because the particle size range was optimized for linear grading and any variation from the linear profile results in lower power output. The activation losses are more dominant than the diffusion losses. This claim follows from the concave down grading profile power curve being less than the concave up grading profile power curve. In the concave up case, there are more, smaller particles in the electrode leading to higher diffusion losses, but these losses are less than the increased activation losses seen by the concave down case, which has more, larger particles.

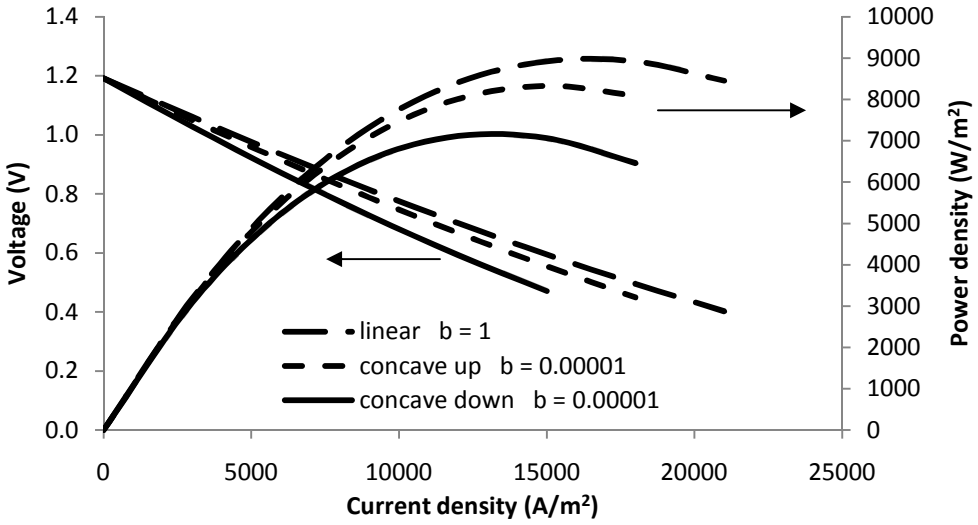

Figure 39. Voltage and power density verses current density for a linear and two nonlinearly graded anodes. Anode is graded from 300 nm to 3 microns. Cathode is 300 nm diameter particles homogeneously.

Figure 40 shows where the difference originates between the power curves seen in the figure above. As said above, the particle size range was optimized for the linear case; therefore any deviation from it leads to increased losses. From this case, it can be concluded that any particle size grading profile can be optimized by changing the particle size grading range, for a given thickness. This type of optimization can be used when a particular grading profile is desired, possibly based on grading profile limitations. For example, if the electrode fabrication apparatus can only produce linearly graded structures.

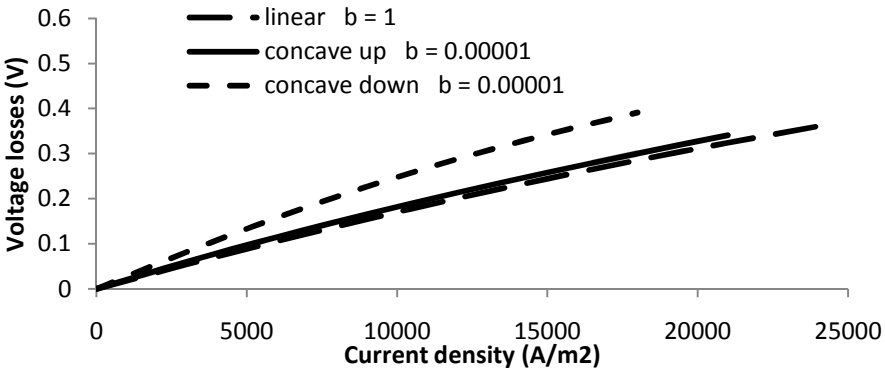

Figure 40. Anode voltage losses verses current density for particle diameter range of 300 nm to 3 microns for 3 different grading profiles.

5.4.2 Effect of Nonlinear Particle Size Grading

A SOFC anode will be optimized for a nonlinear profile and to test the previous analysis. The particle diameter at the electrolyte-anode interface was fixed at 300 nm and the cathode was homogeneous with 300 nm diameter particles. Two cases will be studied for thoroughness. For the first and second case, the particle diameters at the anode free surface are 600 nm and 8 micron, respectively. The profile shape was optimized in the first case with a shape factor of b=0.000075, concave down. The other two profiles shown are b=0.00001 for concave up and down. Figure 41 shows the profiles used in the particle diameter range of 300 nm to 600 nm for the anode.

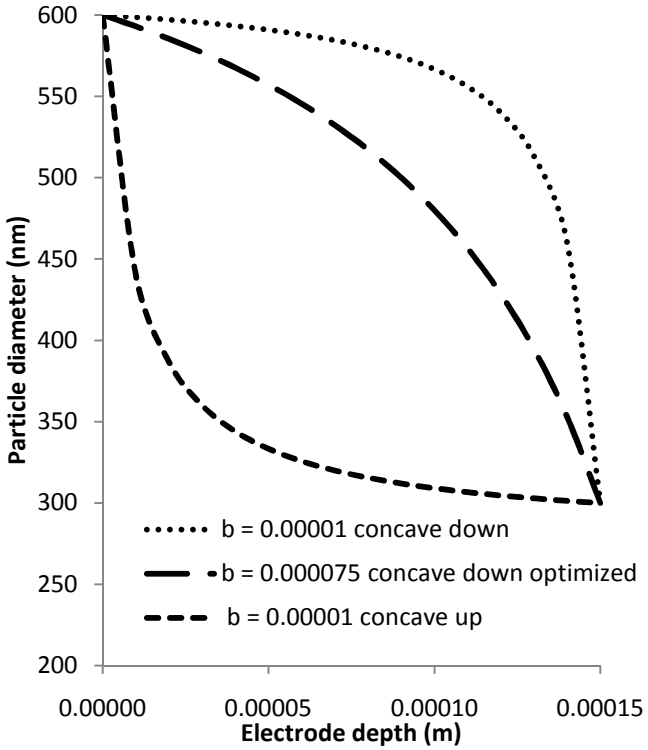

Figure 41. Particle diameter verses electrode depth for three particle diameter grading profiles.

Figure 42 shows the power curves for an optimized nonlinear graded anode from 300 nm to 600 nm diameter particles. The highest power curve is associated with the b = 0.000075 shape factor from Figure 41. This grading profile balances the activation and

diffusion losses. The other two profiles' power curves are presented as well. The concave down grading profile suffers from increased activation losses, while the concave up grading profile suffers from diffusion losses.

From the power curves, it would appear that the diffusion losses have a stronger influence than the activations losses. This is not true. Notice the optimized grading profile and the concave down profile are more similar, than the optimized profile and the concave up grading profile in Figure 41. Yet in Figure 42, the power curves for the concave up and concave down grading profiles are not much different. So qualitatively it can be claimed that activation losses are more influential than diffusion losses in a SOFC electrode.

Keep in mind that the exchange current value chosen for this study was relatively high at 4000 A/m^2 and yet the activation losses are still more influential. The power density improvement of the optimized grading curve is 1.4 and 2.8 % over the other two profiles presented. Another particle diameter grading range will be looked at for thoroughness.

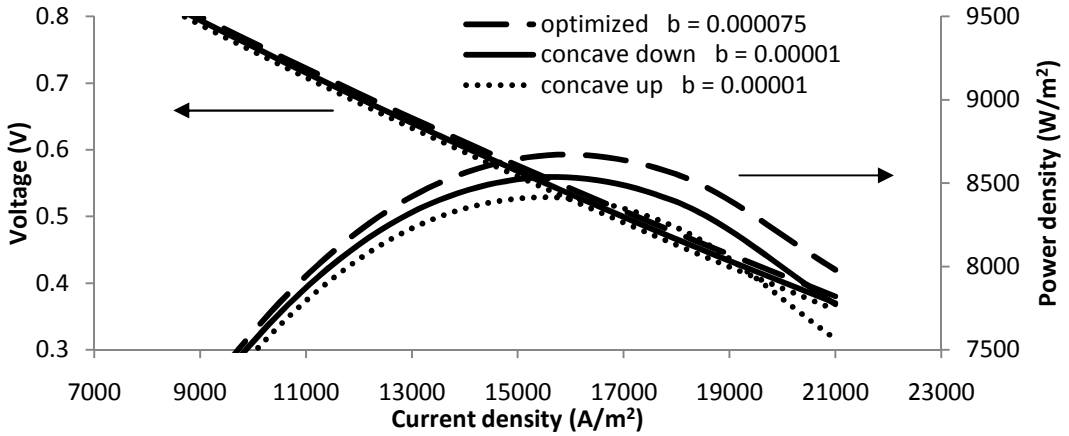

Figure 42. Voltage and power density verses current density for optimized grading profile of determined particle diameter range. Anode ranges from 600 nm to 300 nm. The cathode is homogeneous with 300 nm diameter particles.

Figure 43 shows the particle diameter grading profiles that were used to study the optimization effect of the particle diameter range of 300 nm to 8 microns. The shape factor of b = 0.00005 was found to be optimal. The other curves are presented for comparison.

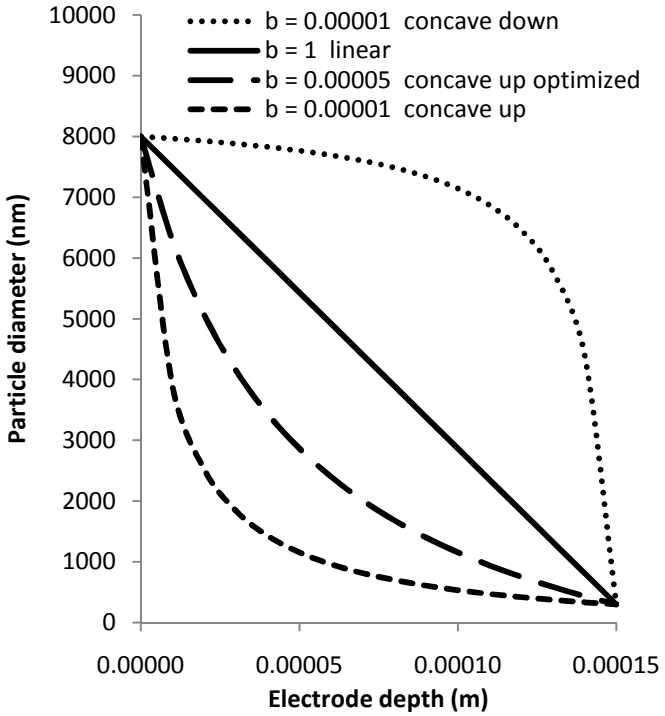

Figure 43. Particle diameter verses electrode depth for four particle diameter grading profiles.

Figure 44 shows the power curves of the grading profiles presented in Figure 43. The anode is graded, while the cathode is homogeneous. The comment above made about activation losses being more dominant than diffusion losses can be seen in this figure as well. Notice the optimized and concave up grading profiles are similar to the optimized and concave down grading profile. In Figure 44, the optimized and concave up power curves are very similar, while the concave down power curve is ~30 % lower. The concave down grading profile has more activation losses because of the fewer number of smaller particles in the electrode structure. The linear grading does not result in the higher power output because the particle size range was not optimized for it, as was done in Figure 39.

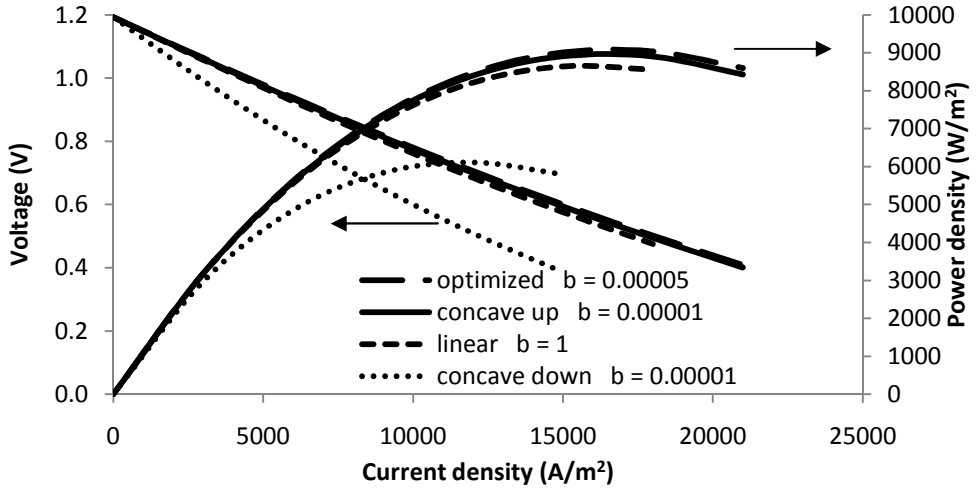

Figure 44. Voltage and power density verses current density for optimized grading profile of determined particle diameter range. Anode ranges from 8 microns to 300 nm. The cathode is homogeneous with 300 nm diameter particles.

From the previous two grading range cases, it can be claimed that any particle size range can be optimized by changing the particle grading profile. This type of optimization can be used when the particle size fabrication abilities are limited to a particular range. It can also be used when there is a concern about dissimilar particle size sintering properties.

5.4.3 Particle Size Grading Design

From the literature available [17, 19], it may appear that particle size grading in an electrode always leads to higher performance. This is not true. In the previous section, when the smallest particle diameter was limited to 300 nm, a homogeneous structure for the cathode was better than a graded structure. This is because there are particle size thresholds on either side of which graded and homogeneous structures are better. Table 7 and Table 8 contain the thresholds of when grading is beneficial in a SOFC cathode. They are at 162 nm and 65 nm for this particular case, in Table 7 and Table 8. Also in these tables, the light gray denotes the cases when grading is beneficial; the medium gray denotes the cases when grading is detrimental (homogeneous is better); the white denotes when grading has little or no effect; and the dark gray denotes the best homogeneous electrode. Notice the diagonal

cells are the voltage losses for homogeneous structures. The best homogeneous structure occurs at 250 nm for the anode and 100 nm for the cathode. This anode and cathode are 150 µm and 30 µm thick. If they were thicker, a larger particle size would be ideal.

If the fabrication technique chosen could only produce particles as small as 100 nm, grading with larger particles toward the free surface would be beneficial. For example, if the cathode were graded from 100 nm to 200 nm from the cathode-electrolyte interface to the free surface (notice white arrow), the voltage loss would be reduced from 0.2668 V to 0.2542 V, a 4.7% reduction in losses. This grading is beneficial because neither activation nor diffusion losses are dominating. (Activation losses become dominant in progressively larger particle diameter structures and diffusion losses become dominant in progressively smaller particle diameter structures) By introducing grading, the diffusion losses were reduced more than the activation losses were increasing, resulting in an overall voltage loss reduction.

If the smallest particle size producible is 162 nm, there would be no benefit to grading with larger particles. If grading with larger particle sizes is introduced, the voltage loss essentially stays the same or increases. Activation losses are dominant when the smallest particle diameter is larger than 162 nm. For example, when the smallest particle size 200 nm, any particle grading with larger particles is detrimental. This is the reason the cathode in the previous section used a homogeneous structure of 300 nm. If any grading with larger particle sizes were introduced, the activation losses would increase more than the diffusion losses would decrease, resulting only in overall increased voltage losses.

Table 7. Cathode voltage loss matrix for a given minimum particle size. Values are voltage losses at 15000 A/m^2.

free surface particle diameter

interface particle diameter

(nm)	20	50	62	65	68	100	150	162	175	200	250	300
300												0.3503
250											0.3285	0.3319
200										0.3056	0.3079	0.3109
175									0.2941	0.2944	0.2963	
162								0.2882	0.2881	0.2883	0.2899	
150							0.2830	0.2825	0.2823	0.2823	0.2838	0.2863
100						0.2668	0.2571	0.2560		0.2542		0.2559
68					0.2749	0.2524	0.2377			0.2323		0.2315
65				0.2779	0.2745	0.2511						
62			0.2816	0.2777	0.2743						0.2259	
50		0.3064	0.2831	0.2786	0.2744	0.2451	0.2256	0.2231	0.2209			
20		0.3501	0.3100	0.3019	0.2944	0.2411						

threshold	grading is beneficial	grading is detrimental	optimized homogeneous

In general, fabrication processes lack the ability to make smaller particle sizes, not larger ones. The following analysis is for thoroughness and may not necessarily be useful in actual fabrication of a SOFC electrode. In Table 8, if the largest particle size producible were 68 nm, then grading with smaller particle sizes from the free surface to the cathode-electrolyte interface could help increase performance until the particle size at the cathode-electrolyte interface is 20 nm. If the cathode were graded from 68 nm at the free surface to 50 nm at the cathode-electrolyte interface (notice vertical white arrow), the voltage losses would decrease because the diffusion losses would increase less than the activation losses would decrease, resulting in an overall voltage loss reduction. This is not true if the cathode were graded from 68 nm at the free surface to 20 nm at the cathode-electrolyte interface. The voltage losses in this case were 0.2944 V. This increase was because diffusion losses have increased to a point such that it is worse than the homogeneous 68 nm case. If the largest particle size were limited to 65 nm and then grading was introduced, there would be essentially no or some increase in voltage losses. Once below 65 nm, the best performing cathode is homogeneous in structure and grading with smaller particles only decreases

performance. Diffusion losses are dominant when the largest particle diameter is smaller than 65 nm.

Table 8. Cathode voltage loss matrix for a given maximum particle size. Values are voltage losses at 15000 A/m^2.

free surface particle diameter

interface particle diameter (nm)	20	50	62	65	68	100	150	162	175
175									0.2941
162								0.2882	0.2881
150							0.2830	0.2825	0.2823
100						0.2668	0.2571	0.2560	
68					0.2749	0.2524	0.2377		
65				0.2779	0.2745	0.2511			
62			0.2816	0.2777	0.2743				
50		0.3064	0.2831	0.2786	0.2744	0.2451	0.2256	0.2231	0.2209
20		0.3501	0.3100	0.3019	0.2944	0.2411			

threshold	grading is beneficial	grading is detrimental	optimized homogeneous

To be consistent through the work, the particle grading threshold was also calculated for the anode. Table 9 shows the anode voltage loss matrix for a given minimum particle size. Similar to the analysis done above for the cathode, the size threshold is at 1.5 µm. If the fabrication technique can only produce particles as small as 1.5 µm, then grading with larger particles toward the free surface will only be detrimental. Above this particle size a homogeneous structure is optimal. A voltage loss matrix for a maximum particle size could not be developed because the numerical solver was unable to reduce error to acceptable levels for accurate results. The results developed for the cathode are conceptual proof that a lower threshold also exists for a given maximum particle size.

Table 9. Anode voltage loss matrix for a given minimum particle size. Values are voltage losses at 15000 A/m^2.

free surface particle diameter

interface particle diameter (µm)	0.25	0.5	1.2	1.5	1.7	1.8	2
2							0.4457
1.8						0.4306	0.4308
1.7					0.4225	0.4226	
1.5				0.4055	0.4055	0.4056	
1.2			0.3769	0.3766		0.3767	0.3768
0.5		0.3040					
0.25	0.2842				0.2271		0.2258

threshold	grading is beneficial	grading is detrimental	optimized homogeneous

The qualitative statements made above about thresholds of particle size grading being beneficial in some regions and detrimental in others is true for all SOFC electrodes. Also, all particle sizes are considered to be after sintering and calcination processes are done.

5.4.4 Effect of Porosity Grading

Ni et al showed that linear porosity grading in electrodes can improve SOFC power performance [16]. In this study, linear and nonlinear porosity grading will be compared with homogeneous electrode structures. Williford et al measured tortuosity values of 2.8 for porosities of 29 to 48% [75]. For this study, tortuosity of 2.8 was used for all porosity values.

Figure 45 shows the voltage losses verses particle diameter for 6 different porosities at 12000 A/m^2. The minimum voltage losses, from 10% to 60% porosity, decrease with decreasing particle size. For all curves, diffusion losses are dominant left of the minimum and activation losses are dominant right of the minimum. The particle size at the minimum voltage loss for each curve increases with decreasing porosity. The pore size is dependent on particle size and percent porosity. This means that larger particle sizes are needed to counteract the decreasing porosity percent. When particle sizes become sufficiently large, the lower porosity has the lowest losses. The best performance occurs when particle size is small and porosity is high. Small particles and high porosity structures are difficult to make. If a good, but not optimal performing, anode was wanted without wanting to balance the porosity

and particle size parameters; then a particle size of greater than 5 µm and a porosity of 10% could be used. The same conclusion can be drawn from Figure 46. As the porosity decreases, the curve becomes more linear for most of its length because the Knudsen diffusion losses become less dominant when compared to the activation losses.

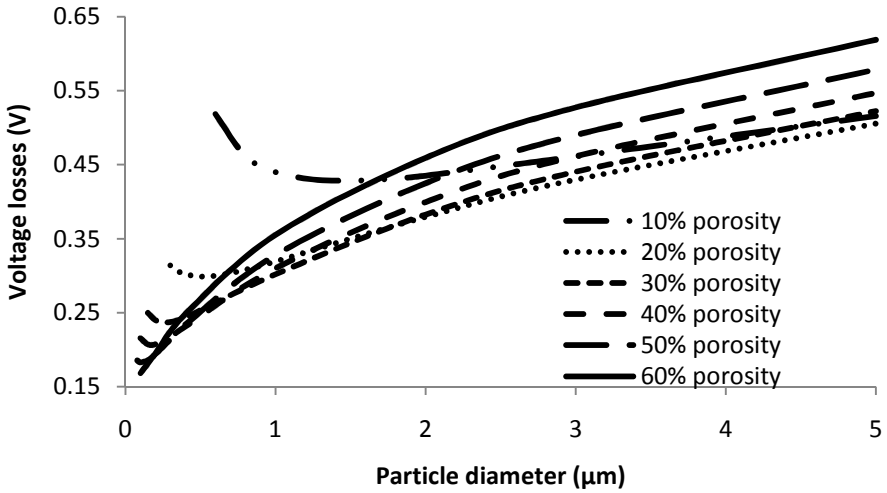

Figure 45. Voltage losses verses particle diameter for 6 different porosities at 12000 A/m^2.

Figure 46 shows the voltage losses verses porosity percent for 4 homogeneous anodes of different particle sizes. The minimum voltage loss for the 0.3 µm, 1 µm, 3 µm and 8 µm anodes is at 50%, 30%, 20%, and 10%, respectively. The minimums occur at these conditions because diffusion losses are dependent on pore size, which is dependent on percent porosity and particle size. The particle size and percent porosity are inversely related when finding the voltage loss minimum. When the particle size becomes smaller, the percent porosity must increase to keep pores large enough to minimize diffusion losses. The converse is also true. The large increase in losses for the 0.3 micron case at low porosity is due to the effect of Knudsen diffusion.

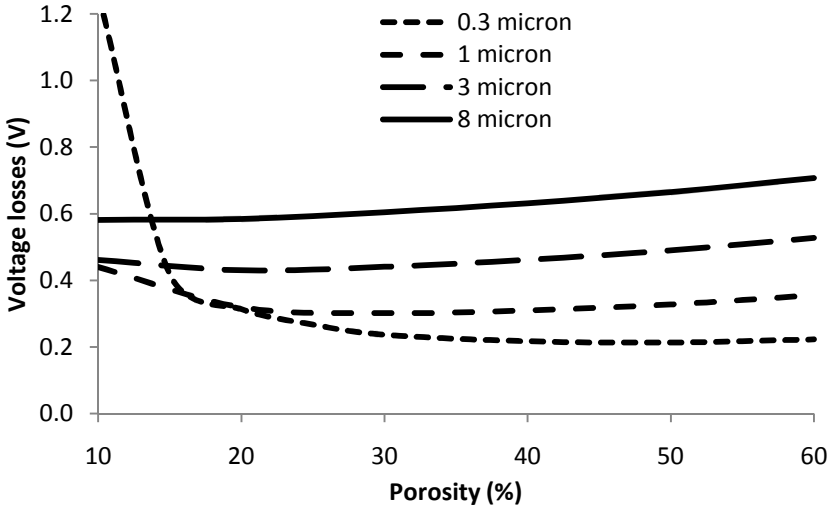

Figure 46. Voltage losses verses porosity percent for homogeneous anodes of four different particle diameters.

Figure 47 shows the porosity grading profiles used in the following study. Table 10 shows the minimum voltage losses for linearly and nonlinearly porosity graded anodes along with particle diameters and porosity grading profile information. The linear porosity grading shares behavior with the homogeneous anodes. The smaller the particle size, the higher the porosity is needed for optimal performance. The nonlinear grading has average porosities are 52%, 36%, 42%, and 28% for 0.3 µm, 1 µm, 3 µm, and 8 µm cases, respectively. The 0.3 micron case has the highest porosity to counteract the smaller particle size on pore size. The 1 and 3 µm case make sense to have lower porosity, but their trend is not as expected. This may have to do with the complicated interplay of losses seen between 1 and 3 microns in Figure 45. The average pore diameter through each structure is 0.22 µm, 0.38 µm, 1.45 µm, and 2.07 µm. The smallest pores for 0.3 µm at 10% porosity are 22 nm, well within the Knudsen diffusion range. The optimal porosity grading profile changes from concave down to concave up as particle sizes become larger.

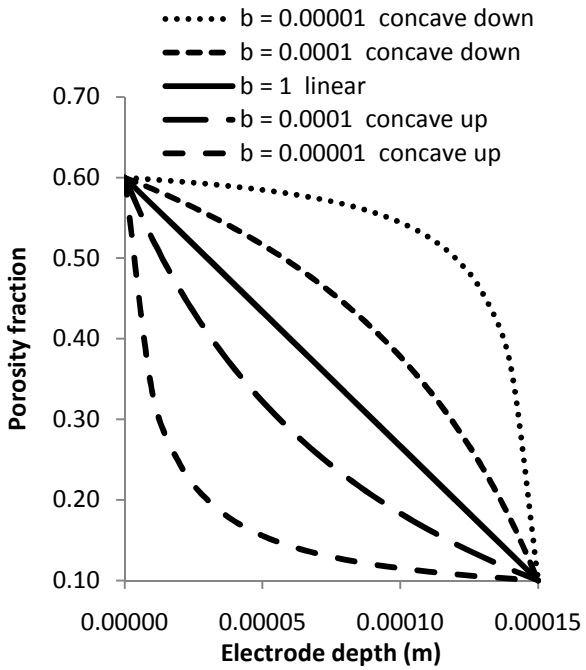

Figure 47. Porosity grading profiles used in this study.

Table 10. Minimum voltage losses for linearly and nonlinearly porosity graded anodes.

	Linear grading		Nonlinear grading		
Particle size	Voltage loss	Porosity	Voltage loss	Porosity	Grading profile/Shape factor
300 nm	0.199	30-60	0.176	10-60	concave down/0.00001
1 µm	0.278	10-60	0.274	10-50	concave down/0.0001
3 µm	0.406	10-60	0.406	10-60	concave down/0.0001
8 µm	0.566	10-40	0.565	10-60	concave up/0.0001

Table 11 shows the voltage loss reduction percent when comparing a homogeneous, linearly, and nonlinearly graded anode. Improvements of 6-8% are seen when linear porosity grading is introduced. When nonlinear grading is used, the 300 nm structure sees the most benefit, while the 1 micron, 3 micron, and 8 micron cases see marginal to no improvement. This is happening because the larger particle sizes have large pores and the effect of Knudsen diffusion is not coming into play and is able to be reduced only with the smaller particle size. The grading profile associated with the minimum voltage loss was drastically different for the linear and nonlinear 3 micron and 8 micron cases, yet they had the same amount of loss. This is likely because the reduction in diffusion losses was offset by the increase in activation

losses. The 0.3 micron cases saw noticeable improvements from linear to nonlinear grading because the diffusion losses were dominant and were decreased more than the activation losses were increased. Also, the optimal grading range was not changed between the linear and nonlinear cases. As was learned from particle size grading, for full optimization both the grading range and profile change together. This means the 0.3 µm particle linear porosity grading was not fully optimized at the 0.1 to 0.6 range.

Table 11. Percent voltage loss reduction between homogeneous and graded anodes. Nonlinear profile information is in Table 10.

Particle diameter	Homogeneous to Linear	Linear to Nonlinear	Homogeneous to Nonlinear
300 nm	7.0%	11.6%	17.8%
1 µm	7.9%	1.4%	9.3%
3 µm	5.6%	0%	5.6%
8 µm	2.7%	0.2%	2.9%

It has been shown that nonlinear porosity grading shows greater benefit in anodes with smaller particles (300 nm), than in anodes with larger particles (3-8 µm). This is due to minimizing the effect of Knudsen losses, which are not noticeable in larger pored structures.

5.5 Effect of Electronic/Ionic Conducting Particle Volume Fraction

Since the ionic and electronic conductors are the same size, the number fraction and volume fraction are interchangeable concepts for this section. Commonly, modeling and experimental papers use the volume fraction of electronic to ionic conductors in the electrode of 0.5 [69-70, 89]. Figure 48 shows that by simply changing the electronic to ionic conductor volume ratio of particles to 0.36, voltage losses can be reduced. Costamagna et al through modeling found the minimum resistance to be 0.37 [72], which is near this ratio and offers further validation to the model developed in this paper. For example, for particle diameters of 0.5 and 1 micron, the voltage loss improvements are 22 and 23%, respectively at 12000 A/m^2. The improved scenarios are presented in solid lines with markers. Smaller particle sizes were not compared because the solver that was used was not able to converge on a solution for particle sizes less than 0.5 microns for the volume fraction 0.5 case. Some

experimental studies use a volume fraction of 0.4 [90-91]. This is very close to the ideal 0.36. There is only a 2.3% voltage loss improvement between these two cases at 12000 A/m^2. It makes sense that the ideal value has not been found experimentally because of experimentations inherent inexactness. This entire study uses the volume fraction and number fraction of 0.36.

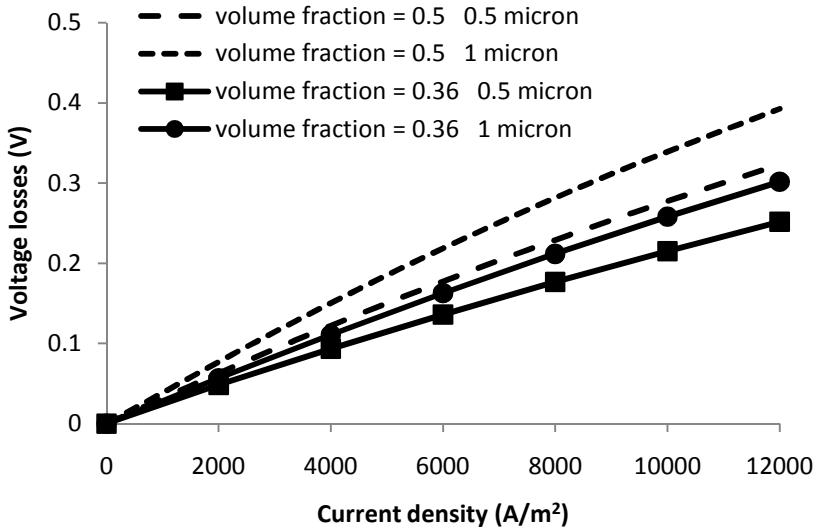

Figure 48. Voltage losses verses current density of 0.5 and 1 micron diameter particles in an anode with electronic number fraction ratios of 0.36 and 0.5 at 12000 A/m^2.

On a side note, Hussain et al concluded that the best volume fraction of electronic to ionic conductors was 0.5 or a 1:1 ratio [69]. This would be true if the electronic to ionic particle size ratio was 2:1. This is in conflict with the results presented here and by Costamagna et al [72]. Hussain's modeling results are also in conflict with the experimental results of [90, 92]. Hussain et al used some of Costamagna et al's micro-model but did not use the empirically-derived percolation theory presented. Hussain instead used a simulation-based percolation model by Sunde et al [93]. Also Hussain et al used an effective conductivity equation from Deseure et al [66] that appears to not have been verified experimentally and conflicts with the micro-model from Costamagna et al.

5.6 Effect of Super-Ionic Conducting Material

There have been developments in ionic conducting materials in recent years that show promise for use in SOFCs. Pasciak et al have investigated bismuth-based ionic conducting materials that exhibit ~70 S/m conductivity at 933 K [94]. Currently, YSZ is primarily used because of its mechanical and chemical stability at high temperatures. A YSZ ionic conductivity curve can be seen below in Figure 49 in comparison with experimental data from Pasciak et al. The YSZ conductivity curve was made from an equation fit to data also used in [16, 88]. At 673 K and 933 K a bismuth-based material yttria-zirconia-stabilized bismuth (YZSB) has 11.6 and 127 times higher conductivity, respectively, than YSZ. Comparison between two anodes, one containing the ordinary YSZ and one containing superconducting YZSB, was performed in this section.

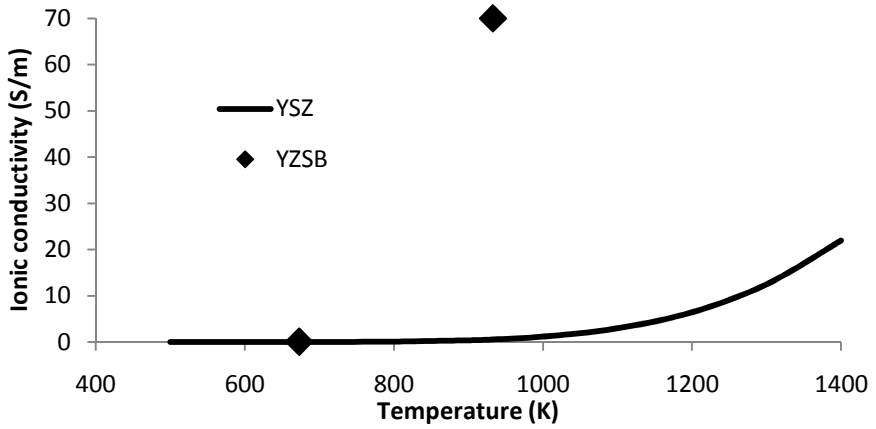

Figure 49. Ionic conductivity verses temperature for YSZ and a bismuth-based super-ionic conducting material [16].

Figure 50 shows the voltage losses verses particle diameter at a current density of 18000 A/m^2, when YSZ is replaced with YZSB, a super-ionic conductor. When YSZ was used, the minimum voltage loss was 0.33 V at 250 nm diameter. When YZSB was used, the minimum voltage loss was 0.144 V at 550 nm diameter. Not only are the voltage losses reduced by 57%, but the particle diameter at which the minimum occurs is 300 nm larger. This larger particle size is much easier to manufacture. Generally, the anode losses account for about half of the total cell losses. Since the anode losses were reduced by 57% the total cell losses

would also be reduced by about 28%. This is large for any power production device or method.

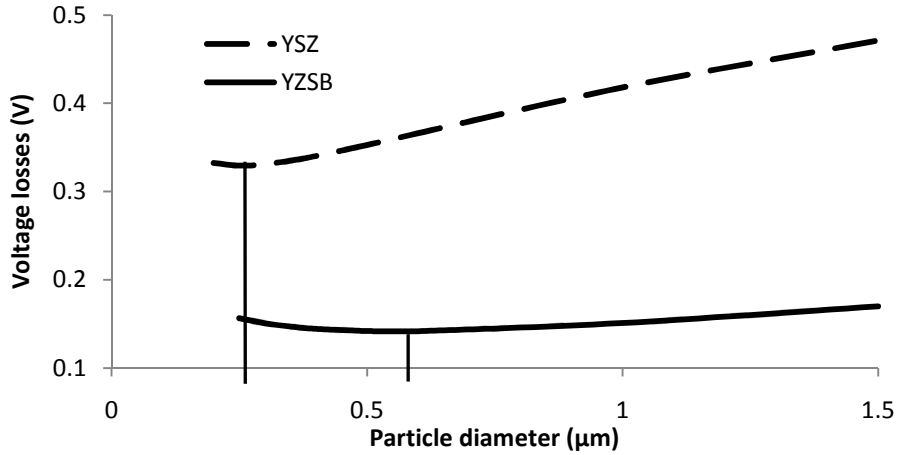

Figure 50. Voltage losses verses particle diameter at 18000 A/m^2. The particle diameter associated with the minimum voltage loss is marked.

Figure 51 shows the voltage losses verses current density for the optimal particle sizes of YSZ and YZSB. Notice the curvature of the YSZ curve and the lack of curvature in the YZSB curve. This means there is lower activation loss in the YZSB curve because the YZSB has a much higher conductivity.

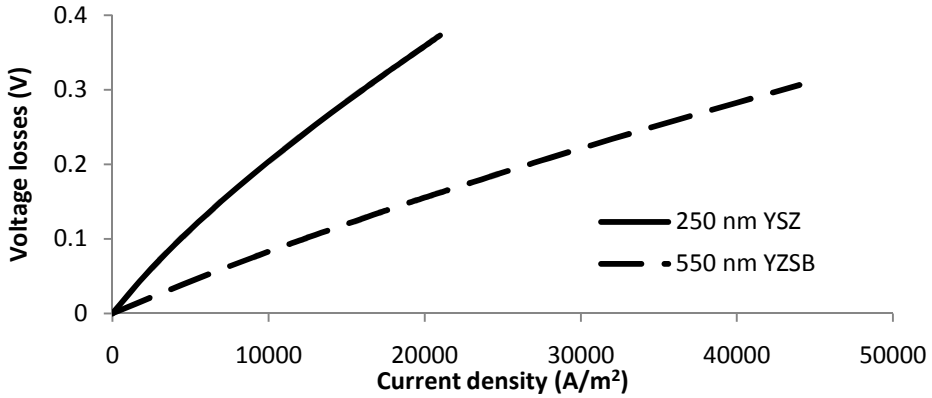

Figure 51. Voltage losses verses current density for the optimal particle size of YSZ and YZSB.

Figure 52 shows the electronic current density profile through the anode when operating at 18000 A/m^2. Each curve was made using the ideal particle size as determined by Figure 50.

The YSZ case used 250 nm, while the YZSB case used 550 nm. The anode free surface is at x=0 and the electrolyte-anode interface is at x=150 microns. Essentially, oxygen ions are conducted into the anode from the electrolyte and are converted to electrons, through the formation of water reaction. This means where the electronic current curve is steeper, there are more reactions occurring. The region, in which the chemical reactions occur, is determined by the balance of effective ionic and electronic conductivities and gas resistance [70]. When YSZ is used, the reaction occurs predominantly near the electrolyte-anode interface because the conductivity of nickel is much higher than YSZ [70]. When YZSB is used, the reaction occurs more evenly through the electrode because YZSB has a higher conductivity than YSZ. Since the reactions are occurring closer to the anode's free surface, the partial pressure of hydrogen is higher, resulting in lower activation losses. The use of YZSB may also reduce Ohmic losses. If the reaction occurs closer to the free surface, where current collection occurs, the electron travels a shorter distance, resulting in a less Ohmic resistance loss. Also consider that the ions are traveling farther as well, since the reactions are occurring further from the electrolyte.

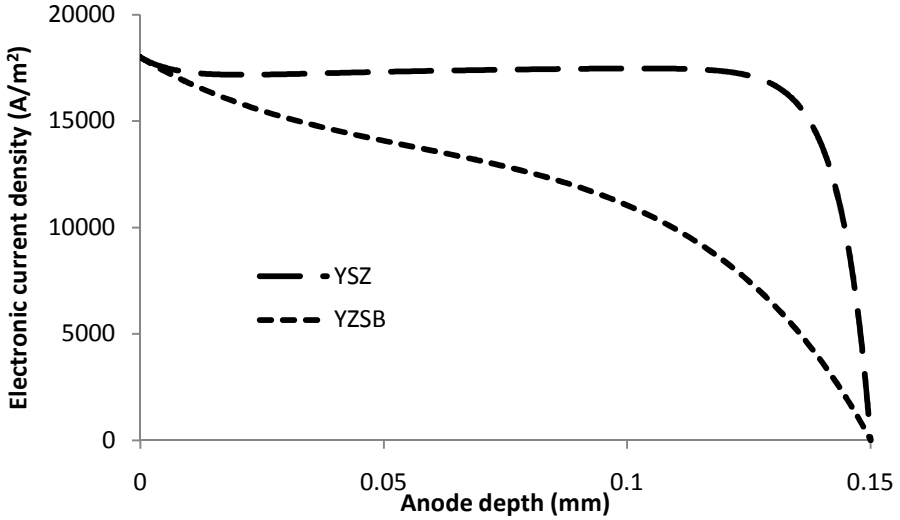

Figure 52. Electronic current density verses anode depth for optimum particle diameters when YSZ and YZSB are used as the ionic conducting phase in an anode. The YSZ and YZSB utilizing anodes had 250 and 550 nm particle diameters, respectively.

CHAPTER 6. CONCLUSIONS & SCIENTIFIC CONTRIBUTIONS

6.1 Conclusions

1. Spray pyrolysis appears to be a suitable fabrication technique for making continuous functionally graded SOFC electrodes.
2. Optimization methodology for SOFC electrodes has been investigated and discussed. This has been done by using a complete 1-D SOFC model and developing a flexible equation to understand influences of linear and nonlinear electrode structure grading on power performance.
    a. Particle size grading optimization methodology
        i. Any particle diameter grading profile can be optimized by changing the particle diameter grading range.
        ii. Any particle diameter grading range can be optimized by changing the diameter grading profile.
        iii. The thinner the electrode, the smaller the particle size grading range will be for optimal power performance. The opposite is also true, the thicker the electrode, the larger the particle size grading range will be for optimal power performance.
        iv. Of the cases presented in this work, larger particle size grading ranges result in lower electrode losses and higher power performance.
    b. Porosity grading optimization methodology
        i. Of the cases presented in this work, larger porosity grading ranges result in lower electrode losses.
        ii. Nonlinear porosity grading shows benefits over linear porosity grading in smaller particle size (300 nm) anodes, due to the effect of Knudsen diffusion losses; benefits are not seen in anodes with larger particles (>3μm).
    c. Activation losses have stronger influence than diffusion losses.
    d. When a SOFC is optimized, the V-I curve will show no dominance of any loss. The curve will become a straight line.

3. Design criteria for particle size grading in SOFC electrodes has been investigated and discussed. When considering particle size grading in a SOFC electrode two cases each with two outcomes is possible.
    a. When electrode fabrication is limited by the smallest particle size that can be used, two outcomes are possible.
        i. If a particle size is used that is smaller than the threshold particle size a graded structure outperforms a homogeneous structure.
        ii. If a particle size is used that is larger than the threshold particle size a homogeneous structure outperforms a graded structure. Activation losses are dominant.
    b. When electrode fabrication is limited by the largest particle size that can be used, two outcomes are possible.
        i. If a particle size is used that is smaller than the threshold particle size a graded homogeneous structure outperforms a graded structure. Diffusion losses are dominant.
        ii. If a particle size is used that is larger than the threshold particle size a graded structure outperforms a homogeneous structure.

6.2 Scientific Contributions

1. The concept of nonlinear graded structures in a SOFC electrode was explored for the first time. A numerical tool was developed that allowed for control of the grading values, including range and profile.
2. Optimization of graded SOFC electrodes in terms of grading range and associated profiles were analyzed and explained in terms of voltage loss contributions. The work yielded electrode design guidelines for fabrication.
3. A deeper understanding was gained of the balance of losses in a SOFC electrode. Losses in an electrode are dependent on microstructural characteristics. The electrodes studied were more sensitive to chemical reaction activation losses (larger particle structures) than losses due to mass transfer (smaller particle structures).

4. A fabrication analysis was incorporated with a SOFC functionally graded electrode model. This encourages the possible pursuit of fabricating continuously graded electrode structures.

CHAPTER 7. RECOMMENDED FUTURE WORK

1. Only symmetric nonlinear particle size and porosity grading was studied. Many other profiles could be explored. This could be done by studying each loss profile.
2. Any further large advancement will not come from changing the physical structure of the electrodes, but by changing the properties of the structures that already exist. For example, activation losses could be reduced by improving TPB conditions or using mixed ionic-electronic conductors.
3. Integrate this electrical performance model with a mechanical lifetime prediction model. This will allow cell design and optimization for power output and cell life prediction.

CHAPTER 8. REFERENCES

[1] EIA/AER, 2007, *Annual Energy Review 2007*, Washington D.C.
[2] Okura, R., Shioshita, S., Kawasato, Y., and Shimizu, J., 2003, "Completion of High-Efficiency Coal-Fired Power Plant," Hitachi Hyoron, 85(2), pp. 163-166.
[3] Song, C., 2002, "Fuel Processing for Low-Temperature and High-Temperature Fuel Cells: Challenges, and Opportunities for Sustainable Development in the 21st Century," Catalysis Today, 77(1-2), pp. 17-49.
[4] Mench, M. M., 2008, *Fuel Cell Engines*, John Wiley & Sons, Hoboken, New Jersey.
[5] Eg&G Technical Services Inc., 2004, *Fuel Cell Handbook*, Morgantown, WV.
[6] Li, X., 2006, *Principles of Fuel Cells*, Taylor & Francis Group, New York.
[7] Fuelcell Energy, March 21, 2007, *Company Update*,
[8] Surdoval, W. A., 2006, *7th Seca Public Workshop & Peer Review*, Philadelphia.
[9] Shaffer, S., 2006, *Development Update on Delphi's Solid Oxide Fuel Cell Power System*, Philadelphia, PA.
[10] Williams, M. C., Strakey, J., and Sudoval, W., 2006, "U.S. Doe Fossil Energy Fuel Cells Program," Journal of Power Sources, 159(2), pp. 1241-1247.
[11] Jono, K., Suda, S., and Hattori, M., 2007, "Effect of Graded Porous Structure on Ni-Ysz Anode Performance," eds., Pennington, NJ 08534-2896, United States, 7, pp. 1541-1546.
[12] Meng, B., Sun, Y., He, X. D., and Li, M. W., 2008, "Graded Ni-Ysz Anode Coatings for Solid Oxide Fuel Cell Prepared by Eb-Pvd," Materials Science and Technology, 24(8), pp. 997-1001.
[13] Hamedani, H. A., 2008, "Investigation of Deposition Parameters in Ultrasonic Spray Pyrolysis for Fabrication of Solid Oxide Fuel Cell Cathode," Ph.D. thesis, Georgia Institute of Technology, Atlanta.
[14] Xu, X., Xia, C., Xiao, G., and Peng, D., 2005, "Fabrication and Performance of Functionally Graded Cathodes for It-Sofcs Based on Doped Ceria Electrolytes," Solid State Ionics, 176(17-18), pp. 1513-1520.
[15] Hart, N. T., Brandon, N. P., Day, M. J., and Lapena-Rey, N., 2002, "Functionally Graded Composite Cathodes for Solid Oxide Fuel Cells," Journal of Power Sources, 106(1-2), pp. 42-50.
[16] Ni, M., Leung, M. K. H., and Leung, D. Y. C., 2007, "Micro-Scale Modelling of Solid Oxide Fuel Cells with Micro-Structurally Graded Electrodes," Journal of Power Sources, 168(2), pp. 369-378.
[17] Ni, M., Leung, M. K. H., and Leung, D. Y. C., 2007, "Micro-Scale Modeling of a Functionally Graded Ni-Ysz Anode," Chemical Engineering and Technology, 30(5), pp. 587-592.
[18] Schneider, L. C. R., Martin, C. L., Bultel, Y., Dessemond, L., and Bouvard, D., 2007, "Percolation Effects in Functionally Graded Sofc Electrodes," Electrochimica Acta, 52(9), pp. 3190-3198.
[19] Greene, E. S., Chiu, W. K. S., and Medeiros, M. G., 2006, "Mass Transfer in Graded Microstructure Solid Oxide Fuel Cell Electrodes," Journal of Power Sources, 161(1), pp. 225-231.
[20] Holtappels, P., and Bagger, C., 2002, "Fabrication and Performance of Advanced Multi-Layer Sofc Cathodes," Journal of the European Ceramic Society, 22(1), pp. 41-48.
[21] O'hayre, R., Barnett, D. M., and Prinz, F. B., 2005, "The Triple Phase Boundary a Mathematical Model and Experimental Investigations for Fuel Cells," Journal of the Electrochemical Society, 152(2), pp. 439-444.
[22] Jain, R., Mandal B. , 2007, "Studies on Ideal and Actual Efficiency of Solar Polymer Electrolyte Fuel Cell," pp.
[23] Casanova, A., 1998, "A Consortium Approach to Commercialized Westinghouse Solid Oxide Fuel Cell Technology," Journal of Power Sources, 71(1-2), pp. 65-70.
[24] Chen, J. C., and Hwang, B. H., 2008, "Microstructure and Properties of the Ni-Cgo Composite Anodes Prepared by the Electrostatic-Assisted Ultrasonic Spray Pyrolysis Method," Journal of the American Ceramic Society, 91(1), pp. 97-102.
[25] Sanson, A., Pinasco, P., and Roncari, E., 2008, "Influence of Pore Formers on Slurry Composition and Microstructure of Tape Cast Supporting Anodes for Sofcs," Journal of the European Ceramic Society, 28(6), pp. 1221-1226.
[26] Jiang, S. P., Love, J. G., and Apateanu, L., 2003, "Effect of Contact between Electrode and Current Collector on the Performance of Solid Oxide Fuel Cells," Solid State Ionics, 160(1-2), pp. 15-26.
[27] Wincewicz, K. C., and Cooper, J. S., 2005, "Taxonomies of Sofc Material and Manufacturing Alternatives," Journal of Power Sources, 140(2), pp. 280-296.

[28] Zhang, X. G., Robertson, M., Deces-Petit, C., Xie, Y. S., Hui, R., Yick, S., Styles, E., Roller, J., Kesler, O., Maric, R., and Ghosh, D., 2006, "Nio-Ysz Cermets Supported Low Temperature Solid Oxide Fuel Cells," Journal of Power Sources, 161(1), pp. 301-307.
[29] Xia, C. R., Chen, F. L., and Liu, M. L., 2001, "Reduced-Temperature Solid Oxide Fuel Cells Fabricated by Screen Printing," Electrochemical and Solid State Letters, 4(5), pp. A52-A54.
[30] Zhang, Y. H., Huang, X. Q., Lu, Z., Liu, Z. G., Ge, X. D., Xu, J. H., Xin, X. S., Sha, X. Q., and Su, W. H., 2006, "A Screen-Printed $Ce_{0.8}sm_{0.2}o_{1.9}$ Film Solid Oxide Fuel Cell with a $Ba_{0.5}sr_{0.5}co_{0.8}fe_{0.2}o_{3-Delta}$ Cathode," Journal of Power Sources, 160(2), pp. 1217-1220.
[31] Ding, J., and Liu, J., 2007, "An Anode-Supported Solid Oxide Fuel Cell with Spray-Coated Yttria-Stabilized Zirconia (Ysz) Electrolyte Film," eds., Shanghai, PEOPLES R CHINA, pp. 1246-1249.
[32] Chen, K. F., Lu, Z., Chen, X. J., Ai, N., Huang, X. Q., Du, X. B., and Su, W. H., 2007, "Development of Lsm-Based Cathodes for Solid Oxide Fuel Cells Based on Ysz Films," Journal of Power Sources, 172(pp. 742-748.
[33] Jacques-Bedard, X., Napporn, T. W., Roberge, R., and Meunier, M., 2007, "Coplanar Electrodes Design for a Single-Chamber Sofc - Assessment of the Operating Parameters," Journal of the Electrochemical Society, 154(3), pp. B305-B309.
[34] Matsuzaki, Y., and Yasuda, I., 2001, "Dependence of Sofc Cathode Degradation by Chromium-Containing Alloy on Compositions of Electrodes and Electrolytes," Journal of the Electrochemical Society, 148(2), pp. A126-A131.
[35] Zhao, F., and Virkar, A. V., 2005, "Dependence of Polarization in Anode-Supported Solid Oxide Fuel Cells on Various Cell Parameters," Journal of Power Sources, 141(1), pp. 79-95.
[36] Zhou, X., Sun, K., Gao, J., Le, S., Zhang, N., and Wang, P., 2009, "Microstructure and Electrochemical Characterization of Solid Oxide Fuel Cells Fabricated by Co-Tape Casting," Journal of Power Sources, 191(2), pp. 528-533.
[37] Du, Y. H., and Sammes, N. M., 2004, "Fabrication and Properties of Anode-Supported Tubular Solid Oxide Fuel Cells," Journal of Power Sources, 136(1), pp. 66-71.
[38] Maffei, N., and De Silveira, G., 2003, "Interfacial Layers in Tape Cast Anode-Supported Doped Lanthanum Gallate Sofc Elements," Solid State Ionics, 159(3-4), pp. 209-216.
[39] Moon, H., Kim, S. D., Hyun, S. H., and Kim, H. S., 2008, "Development of It-Sofc Unit Cells with Anode-Supported Thin Electrolytes Via Tape Casting and Co-Firing," International Journal of Hydrogen Energy, 33(6), pp. 1758-1768.
[40] Breviary Technical Ceramics, 2008, Tape Casting Schematic, December 31, http://www.keramverband.de/pic/ebild57.gif
[41] Will, J., Mitterdorfer, A., Kleinlogel, C., Perednis, D., and Gauckler, L. J., 2000, "Fabrication of Thin Electrolytes for Second-Generation Solid Oxide Fuel Cells," Solid State Ionics, 131(1-2), pp. 79-96.
[42] Tecstra Systems Corporation, 2009, Screen Printing Schematic, January 9, http://glossary.ippaper.com/images/graphicsedviser/print/screen.jpg
[43] Hui, R., Wang, Z. W., Yick, S., Maric, R., and Ghosh, D., 2007, "Fabrication of Ceramic Films for Solid Oxide Fuel Cells Via Slurry Spin Coating Technique," Journal of Power Sources, 172(2), pp. 840-844.
[44] Ai, N., Lu, Z., Chen, K. F., Huang, X. Q., Wei, B., Zhang, Y. H., Li, S. Y., Xin, X. S., Sha, X. Q., and Su, W. H., 2006, "Low Temperature Solid Oxide Fuel Cells Based on Sm0.2ce0.8o1.9 Films Fabricated by Slurry Spin Coating," Journal of Power Sources, 159(1), pp. 637-640.
[45] Pau Scherrer Institut, 2007, Spin Coating Schematic, June 23, http://materials.web.psi.ch/Research/Thin_Films/Methods/Images/Spin.jpg
[46] Kim, S. D., Hyun, S. H., Moon, J., Kim, J.-H., and Song, R. H., 2005, "Fabrication and Characterization of Anode-Supported Electrolyte Thin Films for Intermediate Temperature Solid Oxide Fuel Cells," Journal of Power Sources, 139(1-2), pp. 67-72.
[47] Mti Corporation, 2000, Dip Coating, January 7, http://www.mtixtl.com/ProductImages/dipcoaters/Image247.gif
[48] Sammes, N. M., Du, Y., and Bove, R., 2005, "Design and Fabrication of a 100 w Anode Supported Micro-Tubular Sofc Stack," Journal of Power Sources, 145(2), pp. 428-434.
[49] Minh, N. Q., 2004, "Solid Oxide Fuel Cell Technology-Features and Applications," Solid State Ionics, 174(1-4), pp. 271-277.

[50] Perednis, D., Wilhelm, O., Pratsinis, S. E., and Gauckler, L. J., 2005, "Morphology and Deposition of Thin Yttria-Stabilized Zirconia Films Using Spray Pyrolysis," Thin Solid Films, 474(1-2), pp. 84-95.
[51] Hui, R., Wang, Z. W., Kesler, O., Rose, L., Jankovic, J., Yick, S., Maric, R., and Ghosh, D., 2007, "Thermal Plasma Spraying for Sofcs: Applications, Potential Advantages, and Challenges," Journal of Power Sources, 170(2), pp. 308-323.
[52] Plasma Jet, 2008, Plasma Spray Schematic, June 24, http://www.plasmajet.ro/en/content/plasma-spray
[53] Chang, C. L., Hsu, C. S., and Hwang, B. H., 2008, "Unique Porous Thick Sm0.5sr0.5coo3 Solid Oxide Fuel Cell Cathode Films Prepared by Spray Pyrolysis," Journal of Power Sources, 179(2), pp. 734-738.
[54] Taniguchi, I., Van Landschoot, R. C., and Schoonman, J., 2003, "Fabrication of La1-Xsrxco1-Yfeyo3 Thin Films by Electrostatic Spray Deposition," Solid State Ionics, 156(1-2), pp. 1-13.
[55] Xie, Y., Neagu, R., Hsu, C. S., Zhang, X., and Deces-Petit, C., 2008, "Spray Pyrolysis Deposition of Electrolyte and Anode for Metal-Supported Solid Oxide Fuel Cell," Journal of the Electrochemical Society, 155(4), pp. B407-B410.
[56] Liu, L., and Kim, G.-Y., 2009, "Deposition of Porous Anode Film of Solid Oxide Fuel Cell by Spray Pyrolysis," eds., Pittsburgh, PA, pp.
[57] Carrillo, A. S., Tagawa, T., and Goto, S., 2001, "Application of Mist Pyrolysis Method to Preparation of Ni/Zro2 Anode Catalyst for Sofc Type Reactor," Materials Research Bulletin, 36(5-6), pp. 1017-1027.
[58] Hsu, C. S., and Hwang, B. H., 2006, "Microstructure and Properties of the La0.6sr0.4co0.2fe0.8o3 Cathodes Prepared by Electrostatic-Assisted Ultrasonic Spray Pyrolysis Method," Journal of the Electrochemical Society, 153(8), pp. A1478-A1483.
[59] Liu, Y., Compson, C., and Liu, M., 2004, "Nanostructured and Functionally Graded Cathodes for Intermediate Temperature Solid Oxide Fuel Cells," Journal of Power Sources, 138(1-2), pp. 194-198.
[60] Vanherle, J., Mcevoy, A. J., and Thampi, K. R., 1994, "Conductivity Measurements of Various Yttria-Stabilized Zirconia Samples," Journal of Materials Science, 29(14), pp. 3691-3701.
[61] Princivalle, A., Perednis, D., Neagu, R., and Djurado, E., 2004, "Microstructural Investigations of Nanostructured La(Sr)Mno3-Delta Films Deposited by Electrostatic Spray Deposition," Chemistry of Materials, 16(19), pp. 3733-3739.
[62] Beckel, D., Muecke, U. P., Gyger, T., Florey, G., Infortuna, A., and Gauckler, L. J., 2007, "Electrochemical Performance of Lscf Based Thin Film Cathodes Prepared by Spray Pyrolysis," Solid State Ionics, 178(5-6), pp. 407-415.
[63] Mogensen, M., Sammes, N. M., and Tompsett, G. A., 2000, "Physical, Chemical and Electrochemical Properties of Pure and Doped Ceria," Solid State Ionics, 129(1-4), pp. 63-94.
[64] Kim, J. W., Virkar, A. V., Fung, K. Z., Mehta, K., and Singhal, S. C., 1999, "Polarization Effects in Intermediate Temperature, Anode-Supported Solid Oxide Fuel Cells," Journal of the Electrochemical Society, 146(1), pp. 69-78.
[65] Virkar, A. V., Chen, J., Tanner, C. W., and Kim, J. W., 2000, "The Role of Electrode Microstructure on Activation and Concentration Polarizations in Solid Oxide Fuel Cells," Solid State Ionics, 131(1-2), pp. 189-198.
[66] Deseure, J., Bultel, Y., Dessemond, L., and Siebert, E., 2005, "Theoretical Optimisation of a Sofc Composite Cathode," Electrochimica Acta, 50(10), pp. 2037-2046.
[67] Lee, C. B., and Bae, J. M., 2008, "Fabrication and Characterization of Metal-Supported Solid Oxide Fuel Cells," Journal of Power Sources, 176(1), pp. 62-69.
[68] Ho, C. K., and Webb, S. W., 2006,
[69] Hussain, M. M., Li, X., and Dincer, I., 2006, "Mathematical Modeling of Planar Solid Oxide Fuel Cells," Journal of Power Sources, 161(2), pp. 1012-1022.
[70] Chan, S. H., and Xia, Z. T., 2001, "Anode Micro Model of Solid Oxide Fuel Cell," Journal of the Electrochemical Society, 148(4), pp. A388-A394.
[71] Bouvard, D., and Lange, F. F., 1991, "Relation between Percolation and Particle Coordiination in Binary Powder Mixtures," Acta Metallurgica Et Materialia, 39(12), pp. 3083-3090.
[72] Costamagna, P., Costa, P., and Antonucci, V., 1998, "Micro-Modelling of Solid Oxide Fuel Cell Electrodes," Electrochimica Acta, 43(3-4), pp. 375-394.
[73] Nam, J. H., and Jeon, D. H., 2006, "A Comprehensive Micro-Scale Model for Transport and Reaction in Intermediate Temperature Solid Oxide Fuel Cells," Electrochimica Acta, 51(17), pp. 3446-3460.

[74] Mori, H., Nonaka, N., Mizuno, M., Abe, H., and Naito, M., 2008, "Development of a Geometrical Model for Optimizing Porous Anode Microstructure of Solid Oxide Fuel Cells," Journal of Chemical Engineering of Japan, 41(4), pp. 246-253.
[75] Williford, R. E., Chick, L. A., Maupin, G. D., Simner, S. P., and Stevenson, J. W., 2003, "Diffusion Limitations in the Porous Anodes of Sofcs," Journal of the Electrochemical Society, 150(8), pp. A1067-A1072.
[76] Bieberle, A., and Gauckler, L. J., 2002, "State-Space Modeling of the Anodic Sofc System Ni, H-2-H2o Vertical Bar Ysz," Solid State Ionics, 146(1-2), pp. 23-41.
[77] Mogensen, M., and Skaarup, S., 1996, "Kinetic and Geometric Aspects of Solid Oxide Fuel Cell Electrodes," Solid State Ionics, 86-8(pp. 1151-1160.
[78] Chan, S. H., Khor, K. A., and Xia, Z. T., 2001, "A Complete Polarization Model of a Solid Oxide Fuel Cell and Its Sensitivity to the Change of Cell Component Thickness," Journal of Power Sources, 93(1-2), pp. 130-140.
[79] Colpan, C. O., Dincer, I., and Hamdullahpur, F., 2008, "A Review on Macro-Level Modeling of Planar Solid Oxide Fuel Cells," International Journal of Energy Research, 32(4), pp. 336-355.
[80] Aguiar, P., Adjiman, C. S., and Brandon, N. P., 2004, "Anode-Supported Intermediate Temperature Direct Internal Reforming Solid Oxide Fuel Cell. I: Model-Based Steady-State Performance," Journal of Power Sources, 138(1-2), pp. 120-136.
[81] Yoon, K. J., Zink, P., Gopalan, S., and Pal, U. B., 2007, "Polarization Measurements on Single-Step Co-Fired Solid Oxide Fuel Cells (Sofcs)," Journal of Power Sources, 172(1), pp. 39-49.
[82] Zhu, H., and Kee, R. J., 2003, "A General Mathematical Model for Analyzing the Performance of Fuel-Cell Membrane-Electrode Assemblies," Journal of Power Sources, 117(1-2), pp. 61-74.
[83] Cussler, E. L., 1984, *Diffusion, Mass Transfer in Fluid Systems*, Cambridge University Press, New York.
[84] Reid, R. P., John; Poling, Bruce, 1987, *The Properties of Gases & Liquids*, McGraw-Hill Book Company, New York.
[85] Kuo, C. H., and Gupta, P. K., 1995, "Rigidity and Conductivity Percolation Thresholds in Particulate Composites," Acta Metallurgica Et Materialia, 43(1), pp. 397-403.
[86] Suzuki, M., and Oshima, T., 1983, "Estimation of the Co-Ordination Number in a Multi-Component Mixture of Spheres," Powder Technology, 35(2), pp. 159-166.
[87] Jiang, S. P., Wang, W., and Zhen, Y. D., 2005, "Performance and Electrode Behaviour of Nano-Ysz Impregnated Nickel Anodes Used in Solid Oxide Fuel Cells," Journal of Power Sources, 147(1-2), pp. 1-7.
[88] Ferguson, J. R., Fiard, J. M., and Herbin, R., 1996, "Three-Dimensional Numerical Simulation for Various Geometries of Solid Oxide Fuel Cells," Journal of Power Sources, 58(2), pp. 109-122.
[89] Jiang, S. P., Duan, Y. Y., and Love, J. G., 2002, "Fabrication of High-Performance Ni/Y2o3-Zro2 Cermet Anodes of Solid Oxide Fuel Cells by Ion Impregnation," Journal of the Electrochemical Society, 149(9), pp. 1175-1183.
[90] Lee, J. H., Moon, H., Lee, H. W., Kim, J., Kim, J. D., and Yoon, K. H., 2002, "Quantitative Analysis of Microstructure and Its Related Electrical Property of Sofc Anode, Ni-Ysz Cermet," Solid State Ionics, 148(1-2), pp. 15-26.
[91] Primdahl, S., and Mogensen, M., 2002, "Mixed Conductor Anodes: Ni as Electrocatalyst for Hydrogen Conversion," Solid State Ionics, 152-153(pp. 597-608.
[92] Dees, D. W., Claar, T. D., Easler, T. E., Fee, D. C., and Mrazek, F. C., 1987, "Conductivity of Porous Ni/Zro2-Y2o3 Cermets," Journal of the Electrochemical Society, 34(9), pp. 2141-2146.
[93] Sunde, S., 2000, "Simulations of Composite Electrodes in Fuel Cells," Journal of Electroceramics, 5(2), pp. 153-182.
[94] Pasciak, G., Chmielowiec, J., and Bujlo, P., 2005, "New Ceramic Superionic Materials for It-Sofc Applications," Materials Science-Poland, 23(1), pp. 209-219.

APPENDIX A: HOMOGENEOUS ELECTRODE MODEL CODE

Master.m file

```
clc
clear all
format long

global Aa                %declare global variables
global anode_EC
global beta
global Deff_H2
global Deff_H2O
global F
global It
global La
global PH2
global PH2_frac
global n
global pore_diama
global Ptot
global R
global Rela
global Rioa
global Temp
global c_angle

%Guess a value for eta at x = 0. call this eta_g=voltage loss
eta_g = 0.001;

diameter = 0.000001;
dela = diameter;        %diameter of electrical conducting particle
dioa = diameter;        %diameter of ionic conducting particle
nela = 0.5;             %number fraction of electrical conducting particles
PH2_frac = 0.85;        %partial pressure fraction of hydrogen
Ptot = 101300;          %total pressure at the free surface of the
electrode
It = 5000;              %total current through the electrode
La = .000150;           %thickness
Temp = 1273;            %operating temperature
anode_EC = 1000;        %exchange current density (A/m^2)
P_a = .41;              %porosity
T_a = 3;                %tortuosity
necking = 0.5;          %necking factor between particle contacts
cond_el = 2e6;          %electrical conductivity (S/m)
cond_io = 15;           %ionic conductivity (S/m)
c_angle = pi/12;        %contact angle between particles
n = 1;                  %number of electrons in the reaction
beta = 0.5;             %symmetry factor a.k.a.-charge transfer balance
R = 8.314;              %gas constant (J/(K*mol))
F = 96485;              %Faradays' constant (C/mol)

% The next two functions obtain constants that are used in the system of
% equations later.
% Rela is electronic resistivity
```

```
% Rioa is ionic resistivity
% Aa is reaction surface area
% pore_diama is pore diameter
% Deff_H2 and Deff_H2O are the diffusion coefficients of hydrogen and
water
[Rela,Rioa,Aa,pore_diama] = micro
(dela,dioa,P_a,cond_el,cond_io,necking,nela);
[Deff_H2,Deff_H2O,PH2] = macro (pore_diama,Temp,P_a,T_a,Ptot,PH2_frac);

% This function gives the shooting solver the initial guess for eta.
[t,y,eta_optimal] = solution_finder(eta_g)
```

micro.m file

```
function[Rela,Rioa,Aa,pore_diama]=micro(dela,dioa,P_a,cond_el,cond_io,neck
ing,nela)
format long

rela = dela/2;          %particle radius
rioa = dioa/2;          %particle radius
global c_angle          %contact angle, 15 degrees
Z = 6;                  %coordination number in random binary packing

nioa = 1-nela;            %number fraction of ionic conducting particles
Pa = rioa./rela;          %particle radius ratio

Zela = 3+((Z-3)./(nela+(1-nela).*Pa.^2));          %coordination number of
electronic conducting particles
Zioa = 3+(((Z-3)*Pa.^2)./(nela+(1-nela).*Pa.^2));  %coordination number of
ionic conducting particles

Zel_ela = nela*Z./(nela+(1-nela).*Pa.^2);       %coordination number
between electronic conducting particles
Zio_ioa = nioa*Z./(nioa+(1-nioa).*Pa.^-2);      %coordination number
between ionic conducting particles
pela = (1-((4.236-Zel_ela)/2.472).^2.5).^0.4;   %probability of electronic
particle being in a percolation cluster
pioa = (1-((4.236-Zio_ioa)/2.472).^2.5).^0.4;   %probability of ionic
particle being in a percolation cluster

% calculate number of particles per unit and the reaction/contact area
if Pa>1
    n_stara = (1-P_a)./(4/3*pi*rela.^3.*(nela+(1-nela).*Pa.^3));
    Aa =
pi*(rela*sin(c_angle))^2.*n_stara.*nela.*nioa.*Zela.*Zioa/Z.*pela.*pioa;
else
    n_stara = (1-P_a)./(4/3*pi*rioa.^3.*(nioa+(1-nioa).*Pa.^-3));
    Aa =
pi*(rioa*sin(c_angle))^2.*n_stara.*nela.*nioa.*Zela.*Zioa/Z.*pela.*pioa;
end
%%%%%%%%%%%%%%%%%%%%%%%%%%%%%%%%%%%%%%%%%%%%%%%%%%%%    Percolation Theory
Start
% calculate percolation thresholds. probability of conduction will be zero
% if no particle clusters are connected through entire thickness of
```

```
% electrode
pe0a = 0;
pi0a = 0;
Z = 6;
Zel_el0a = 4.236-2.472*(-(pe0a.^2.5-1)).^.4;
Zio_io0a = 4.236-2.472*(-(pi0a.^2.5-1)).^.4;

ncethresha = Pa.^2*Zel_el0a./(Z+(Pa.^2-1)*Zel_el0a);
ncithresha = Pa.^-2*Zio_io0a./(Z+(Pa.^-2-1)*Zio_io0a);
%%%%%%%%%%%%%%%%%%%%%%%%%%%%%%%%%%%%%%%%%%%%%%%%%%%%    Percolation Theory
End

Rela = (1-ncethresha).^2./(necking*cond_el*(nela-ncethresha).^2);
%electronic resistivity
Rioa = (1-ncithresha).^2./(necking*cond_io*(nioa-ncithresha).^2);   %ionic
resistivity

% calculate pore diameter (m)
pore_diama = 2/3*(dela*P_a/(1-P_a))*(nela+(1-nela)*Pa^3)/(nela+(1-
nela)*Pa^2);
```

macro.m file

```
function
[Deff_H2,Deff_H2O,PH2]=macro(pore_diama,Temp,P_a,T_a,Ptot,H2_frac)

pore_radiusa=pore_diama/2;

molwtH2=2.0158;         %molecular weight of diatomic hydrogen (g/mol)
molwtH2O=18.0148;       %molecular weight of water (g/mol)

PH2=H2_frac*Ptot;       %partial pressure of hydrogen in feed gas (Pa)

% Knudsen diffusion calculation    ======================================
DkH2=97*pore_radiusa*(Temp/molwtH2)^.5;     %Knudsen diffusion coefficient
for hydrogen(m^2/s)
DkH2O=97*pore_radiusa*(Temp/molwtH2O)^.5;   %Knudsen diffusion coefficient
for water(m^2/s)

% Enskog-Chapman Binary Gas Diffusion Calculation=========================
A_H2=2.827;                     %collision diameter of hydrogen (angstrom)
A_H2O=2.641;                    %collision diameter of water (angstrom)
coldiam_H2_H2O=(A_H2+A_H2O)/2;  %average collision diameter (angstrom)

e_k_H2=59.7;                     %well depth of hydrogen (erg/K)
e_k_H2O=809.1;                   %well depth of water (erg/K)
e_k_H2_H2O=(e_k_H2*e_k_H2O)^.5;  %Lennard-Jones potential

coeff_a=Temp/e_k_H2_H2O;
A=1.06036;          %coefficients have been determined empirically
B=.15610;
C=.193000;
D=.47635;
```

```
E=1.03587;
FF=1.52996;
G=1.76474;
H=3.89411;

% diffusion collision integral is calculated (dimensionless)
col_int_a=A/coeff_a^B+C/exp(D*coeff_a)+E/exp(FF*coeff_a)+G/exp(H*coeff_a);
% binary diffusion is calculated and converted from (cm^2/s) to (m^2/s)
D_H2_H2O=.0018583*(1/molwtH2+1/molwtH2O)^.5*Temp^1.5/(Ptot/101300*col_int_
a*coldiam_H2_H2O^2*10000);

% effective diffusion coefficients accounting for porosity and tortuosity
Deff_H2=P_a/T_a*(1/DkH2+1/D_H2_H2O)^-1;
Deff_H2O=P_a/T_a*(1/DkH2O+1/D_H2_H2O)^-1;
```

solution_finder.m file

```
function [t,y,eta_optimal] = solution_finder(eta_g)
%Developed : Dr Baskar Ganapathysubramanian
%July 29, 2009
%Version 2.0
%Solves the stiff-coupled ODE BVP by the shooting method. Additionaly uses
%a function minimizer to find the optimal initial value
format long

% Now run this minimization algorithm to get the best value of eta_g that
% results in a solution that satisfies all boundary conditions
% This function is the error minimizer
options = optimset('Display','notify','TolFun',1e-2);
eta_optimal = fminsearch(@fc,eta_g,options);

% After the optimal eta is found, it is sent to final_solve.
[t,y] = final_solve(eta_optimal);

figure(1)
plot(t,y(:,1))
xlabel('Thickness (m)')
ylabel('Voltage (V)')
% axis([0 .00015 0 .3])
% figure(2)
% plot(t,y(:,2))
% xlabel('Thickness (m)')
% ylabel('dV')
figure(3)
plot(t,y(:,3))
xlabel('Thickness (m)')
ylabel('H2 Partial Pressure(Pa)')
% axis([0 .00015 80000 100000])
figure(4)
plot(t,y(:,4))
xlabel('Thickness (m)')
ylabel('Current Density(A)')
% axis([0 .00015 0 5000])
```

```
global Aa anode_EC PH2 beta n F Temp Ptot R
diel_calc=-Aa.*anode_EC.*(y(:,3)./PH2.*exp(beta.*n.*F.*y(:,1)./(R.*Temp))-
(Ptot-y(:,3))./(Ptot-PH2).*exp(-beta.*n.*F.*y(:,1)./(R.*Temp)));

fit_i=polyfit(t,y(:,4),10);
dfit_i=polyder(fit_i);
dfit_eval=polyval(dfit_i,t);

figure(7)
plot(t,polyval(fit_i,t))
xlabel('Thickness (m)')
ylabel('polyfit current(A)')

figure(5)
plot(t,dfit_eval)
xlabel('Thickness (m)')
ylabel('polyfit dcurrent(A)')

figure(6)
plot(t,diel_calc)
xlabel('Thickness (m)')
ylabel('calculated dcurrent(A)')

% This function is error calculator
% This function solves the Initial value ODE
function error = fc(eta_g);
format long

global eta_p            %declare global variables
global eta_p_end
global It
global La
global PH2_frac
global press_o
global Ptot
global Rela
global Rioa

% Each shoot will be compared with eta_p_end.
eta_p = Rela * It;              %eta prime BC at free surface
eta_p_end = Rioa * It;          %eta prime BC at electrolyte interface
press_o = Ptot * PH2_frac;      %H2 pressure at frees surface (Pa)

options = odeset('RelTol',1e-10,'Stats','off','NonNegative',[1 3 4]);

% These are the initlal value conditions for the shooter.
[t,y]=ode15s(@fuelcell,[0 La],[eta_g eta_p press_o It],options);

% Plot just to visualize convergence
% plot(t,y(:,1));
% pause(1);
```

```
%check to see if this guessed value of eta_g results in a valid eta_prime
%at the right side boundary
error = (eta_p_end-y(end,2)).^2

%This function is the ODE solver
%Developed : Reuben Flesner, Dr Baskar Ganapathysubramanian
%July 29, 2009
%Version 2.0
function dy = fuelcell(t,y);
format long
% call global variables
global Rela Rioa Aa anode_EC PH2 beta n F Temp Ptot Deff_H2 Deff_H2O R

dy = zeros(4,1);

dy(1) = y(2);
dy(2) = (Rela+Rioa)*Aa*anode_EC*(y(3)/PH2*exp(beta*n*F*y(1)/(R*Temp))-
((Ptot-y(3))/(Ptot-PH2))*exp(-beta*n*F*y(1)/(R*Temp)));
dy(3) = -R*Temp*y(4)/(2*F*((1-y(3)/Ptot)*Deff_H2+y(3)/Ptot*Deff_H2O));
dy(4) = -Aa*anode_EC*(y(3)/PH2*exp(beta*n*F*y(1)/(R*Temp))-(Ptot-
y(3))/(Ptot-PH2)*exp(-beta*n*F*y(1)/(R*Temp)));
```

final_solve.m file

```
function [t,y] = final_solve(eta_g)
%Developed : Dr Baskar Ganapathysubramanian
%July 29, 2009
%Version 2.0
%Solves the sstiff-coupled ODE BVP by the shooting method. Additionaly
uses
%a function minimizer to find the optimal initial value
format long

global It           %call global variables
global eta_p
global press_o

options = odeset('RelTol',1e-10,'Stats','off','NonNegative',[1 3 4]);
[t,y]=ode15s(@fuelcell1,[0 150e-6],[eta_g eta_p press_o It],options);

%This function is the ODE solver
%Developed : Reuben Flesner, Dr Baskar Ganapathysubramanian
%July 29, 2009
%Version 2.0

function dy = fuelcell1(t,y);
format long
dy = zeros(4,1);

% call global variables
global Aa anode_EC beta Deff_H2 Deff_H2O F n PH2 Ptot R Rela Rioa Temp
```

```
dy(1) = y(2);
dy(2) = (Rela+Rioa)*Aa*anode_EC*(y(3)/PH2*exp(beta*n*F*y(1)/(R*Temp))-
((Ptot-y(3))/(Ptot-PH2))*exp(-beta*n*F*y(1)/(R*Temp)));
dy(3) = -R*Temp*y(4)/(2*F*((1-y(3)/Ptot)*Deff_H2+y(3)/Ptot*Deff_H2O));
dy(4) = -Aa*anode_EC*(y(3)/PH2*exp(beta*n*F*y(1)/(R*Temp))-(Ptot-
y(3))/(Ptot-PH2)*exp(-beta*n*F*y(1)/(R*Temp)));
```

APPENDIX B: PARTICLE SIZE GRADED ELECTRODE MODEL CODE

```
function solution_finder_concaveup
%Developed : Dr Baskar Ganapathysubramanian & Reuben Flesner
%July 29, 2009
%Version 2.0
%Solves the stiff-coupled ODE BVP by the shooting method. Additionaly uses
%a function minimizer to find the optimal initial value
close all
clear all
clc

format long
eta_g = 0.0041;

% Now run this minimization algorithm to get the best value of eta_g that
% results in a solution that satisfies all boundary conditions
% This function is the error minimizer
options = optimset('Display','off','TolFun',1e-2);

eta_optimal = fminsearch(@fc,eta_g,options);

% After the optimal eta is found, it is sent to final_solve.
[x,y] = final_solve_concaveup(eta_optimal);

global La
figure(1)                   %plot voltage
plot(x,y(:,1))
% axis([0 La 0 .5])
xlabel('Thickness (m)')
ylabel('Voltage (V)')
figure(3)                   %plot H2 pressure
plot(x,y(:,3))
xlabel('Thickness (m)')
ylabel('H2 Partial Pressure(Pa)')
% axis([0 .00015 80000 100000])
figure(4)                   %plot current
plot(x,y(:,4))
xlabel('Thickness (m)')
ylabel('Current Density(A)')
axis([0 La 0 5000])

eta_optimal         %output eta_optimal for viewing
y(end,1)            %output voltage for viewing

global d_free d_interface b La          %call global variables
x = 0:.000001:La;
d = (d_free-d_interface)/d_free*((b^2+La*b)*d_free./(La*(x+b)) + d_free-
(d_free*(b^2+La*b)/(La*b))) + d_interface;
figure(7)
plot(x,d)                   %plot particle grading profile
```

```
xlabel('Thickness (m)')
ylabel('particle diameter (m)')

% This function is error calculator
% This function solves the Initial value ODE
function error = fc(eta_g)
format long

global cond_el          %declare global variable
global cond_io          %declare global variable
global d_free           %declare global variable
global d_interface      %declare global variable
global eta_p            %declare global variable
global eta_p_end        %declare global variable
global H2_frac          %declare global variable
global It               %declare global variable
global La               %declare global variable
global necking          %declare global variable
global nel              %declare global variable
global press_o          %declare global variable
global Ptot             %declare global variable

cond_el = 2e6;          %input bulk electrical conductivity value
cond_io = 15;           %input bulk ionic conductivity value
d_free = 1e-6;          %input conducting particle diamter at free surface
d_interface = .1e-6;    %input conducting particle diameter at EE
interface
del = d_free;           %reassignment for function micro_bc_a
dio = d_free;           %reassignment for function micro_bc_a
It=5000;                %input total current through electode
La=.000150;             %input electrode thickness
H2_frac=.85;            %input fraction of feed gas that is hydrogen
Ptot=101300;            %input total pressure, usually atmospheric
pressure
necking = 0.5;          %input necking factor between particles
nel = 0.5;              %input number fraction of electronic conducting
particles

% this function finds Rel for the BC at 'a' for interval 'a' to 'b'
[Rel_bc]=micro_bc_a(del,dio,cond_el,necking,nel); %find Rel at free
surface

del = d_interface;      %reassign for function micro_bc_b
dio = d_interface;      %reassign for function micro_bc_b

% this function finds Rio for the BC at 'b' for interval 'a' to 'b'
[Rio_bc]=micro_bc_b(del,dio,cond_io,necking,nel); %find Rio at free
surface

% Each shoot will be compared with eta_p_end.
eta_p = Rel_bc * It;
eta_p_end = Rio_bc * It;
press_o = H2_frac * Ptot;
```

```
options = odeset('RelTol',1e-10,'Stats','notify','NonNegative',[1 3 4]);
% These are the initlal value conditions for the shooter.
[x,y]=ode15s(@eq_system,[0 La],[eta_g eta_p press_o It],options);

%check to see if this guessed value of eta_g results in a valid eta_prime
%at the right side boundary
error = (eta_p_end-y(end,2)).^2         %output error to watch converge

%This function is the ODE solver
%Developed : Reuben Flesner, Dr Baskar Ganapathysubramanian
%July 29, 2009
%Version 2.0
function dy = eq_system(x,y)
format long
dy = zeros(4,1);

global A              %declare global variable
global anode_EC       %declare global variable
global b              %declare global variable
global beta           %declare global variable
global c_angle        %declare global variable
global d              %declare global variable
global F              %declare global variable
global n              %declare global variable
global P_a            %declare global variable
global R              %declare global variable
global T_a            %declare global variable
global Temp           %declare global variable

%call global variables into function
global cond_el cond_io d_free d_interface H2_frac La necking nel Ptot
%
==========================================================================
b = .00001;            %b changes the grading profile 1=straight line,
small values make more non-linear profiles
d=(d_free-d_interface)/d_free*((b^2+La*b)*d_free/(La*(x+b)) + d_free-
(d_free*(b^2+La*b)/(La*b))) + d_interface;

del = d;              %diamteter of electronic conducting particle (m)
dio = d;              %diamteter of ionic conducting particle (m)
P_a = .41;            %porosity
Temp = 1273;          %temperature (K)
T_a = 3;              %tortuosity
c_angle = pi/12;      %contact angle between particles (radians)
anode_EC = 1000;      %exchange current (A/m^2)
F = 96485;            %Faraday's constant (C/mol)
n = 1;                %number of electrons in limiting reaction step
R = 8.314;            %gas constant (J/(mol*K))
beta = 0.5;           %charge transfer symmetry factor

%the micro and macro functions are called to find resistivity, reaction
```

```
%area, pore diameter, diffusion coefficients and the partial pressure of
H2
[Rel,Rio,A,pore_diam]=micro(del,dio,P_a,cond_el,cond_io,necking,nel,c_angl
e);
[Deff_H2,Deff_H2O,PH2] = macro (pore_diam,Temp,P_a,T_a,Ptot,H2_frac);

dy(1) = y(2);
dy(2) = (Rel+Rio).*A*anode_EC*(y(3)/PH2*exp(beta*n*F*y(1)/(R*Temp))-
((Ptot-y(3))/(Ptot-PH2))*exp(-beta*n*F*y(1)/(R*Temp)));
dy(3) = -R*Temp.*y(4)/(2*F*((1-y(3)/Ptot).*Deff_H2+y(3)./Ptot.*Deff_H2O));
dy(4) = -A*anode_EC*(y(3)/PH2*exp(beta*n*F*y(1)/(R*Temp))-(Ptot-
y(3))/(Ptot-PH2)*exp(-beta*n*F*y(1)/(R*Temp)));

function [Rel_bc]=micro_bc_a(del,dio,cond_el,necking,nel)
format long
rela = del/2;        %particle radius
rioa = dio/2;        %particle radius
Z = 6;               %coordination number in random binary packing
nela=nel;
Pa = rioa./rela;     %particle radius ratio
%%%%%%%%%%   Percolation Theory Start
pe0a = 0;       %probability of conduction occurring at the percolation
limit
Zel_el0a = 4.236-2.472*(-(pe0a.^2.5-1)).^.4;    %elec to elec contact at
p=0
ncethresha = Pa.^2*Zel_el0a./(Z+(Pa.^2-1)*Zel_el0a);    %critical number
fraction for elec conduction

%%%%%%%%%%   Percolation Theory End
Rel_bc = (1-ncethresha).^2./(necking*cond_el*(nela-ncethresha).^2);
%effective elec resistivity

function [Rio_bc]=micro_bc_b(del,dio,cond_io,necking,nel)
format long
rela = del/2;        %particle radius
rioa = dio/2;        %particle radius
Z = 6;               %coordination number in random binary packing
nela=nel;
nioa = 1-nela;
Pa = rioa./rela;         %particle radius ratio
%%%%%%%%%%   Percolation Theory Start
pi0a = 0;       %probability of conduction occurring at the percolation
limit
Zio_io0a = 4.236-2.472*(-(pi0a.^2.5-1)).^.4;    %ionic to ionic contact at
p=0
ncithresha = Pa.^-2*Zio_io0a./(Z+(Pa.^-2-1)*Zio_io0a);  %critical number
fraction for ionic conduction
%%%%%%%%%%   Percolation Theory End
Rio_bc = (1-ncithresha).^2./(necking*cond_io*(nioa-ncithresha).^2);
%effective ionic resistivity

function
[Rel,Rio,A,pore_diam]=micro(del,dio,P_a,cond_el,cond_io,necking,nel,c_angl
e)
```

```
format long

rela = del/2;         %particle radius
rioa = dio/2;         %particle radius
Z = 6;                 %coordination number in random binary packing

nela=nel;               %number fraction of electronic conducting
particles
nioa = 1-nela;          %number fraction ofionic conducting particles
Pa = rioa./rela;        %particle radius ratio

Zela = 3+((Z-3)./(nela+(1-nela).*Pa.^2));        %elec coordination number
Zioa = 3+(((Z-3)*Pa.^2)./(nela+(1-nela).*Pa.^2));%ionic coordination
number

Zel_ela = nela*Z./(nela+(1-nela).*Pa.^2); %elec to elec coordination
number
Zio_ioa = nioa*Z./(nioa+(1-nioa).*Pa.^-2);  %ion to ion coordination
number
pela = (1-((4.236-Zel_ela)/2.472).^2.5).^0.4;
pioa = (1-((4.236-Zio_ioa)/2.472).^2.5).^0.4;

% number of particles per volume and reaction/contact surface area
if Pa>1
    n_stara = (1-P_a)./(4/3*pi*rela.^3.*(nela+(1-nela).*Pa.^3));
    A =
pi*(rela*sin(c_angle))^2.*n_stara.*nela.*nioa.*Zela.*Zioa/Z.*pela.*pioa;
else
    n_stara = (1-P_a)./(4/3*pi*rioa.^3.*(nioa+(1-nioa).*Pa.^-3));
    A =
pi*(rioa*sin(c_angle))^2.*n_stara.*nela.*nioa.*Zela.*Zioa/Z.*pela.*pioa;
end
%%%%%%%%%%%%%%%%%%%%%%%%%%%%%%%%%%%%%%%%%%%%%%%%%%%%%    Percolation Theory
Start
pe0a = 0;       %probability of conduction occurring at the percolation
limit
pi0a = 0;       %probability of conduction occurring at the percolation
limit
Zel_el0a = 4.236-2.472*(-(pe0a.^2.5-1)).^.4;    %elec to elec contact at
p=0
Zio_io0a = 4.236-2.472*(-(pi0a.^2.5-1)).^.4;    %ionic to ionic contact at
p=0

ncethresha = Pa.^2*Zel_el0a./(Z+(Pa.^2-1)*Zel_el0a);    %critical number
fraction for elec conduction
ncithresha = Pa.^-2*Zio_io0a./(Z+(Pa.^-2-1)*Zio_io0a);  %critical number
fraction for ionic conduction

% volfrac_e0a = ncethresha./((1-ncethresha).*Pa.^3+ncethresha);
% volfrac_i0a = ncithresha./((1-ncithresha)./Pa.^3+ncithresha);

%%%%%%%%%%%%%%%%%%%%%%%%%%%%%%%%%%%%%%%%%%%%%%%%%%%%%    Percolation Theory
End
```

```
Rel = (1-ncethresha).^2./(necking*cond_el*(nela-ncethresha).^2);
%effective elec resistivity
Rio = (1-ncithresha).^2./(necking*cond_io*(nioa-ncithresha).^2);
%effective ionic resistivity

% pore diameter calculation
pore_diam = 2/3*(del*P_a/(1-P_a))*(nela+(1-nela)*Pa^3)/(nela+(1-
nela)*Pa^2);

function [Deff_H2,Deff_H2O,PH2] = macro
(pore_diam,Temp,P_a,T_a,Ptot,H2_frac)

% see previous code for macro model comments
pore_radiusa=pore_diam/2;
molwtH2=2.0158;
molwtH2O=18.0148;

PH2=H2_frac*Ptot;

% Knudsen diffusion
DkH2=97*pore_radiusa*(Temp/molwtH2)^.5;
DkH2O=97*pore_radiusa*(Temp/molwtH2O)^.5;

% Chapman-Enskog Binary diffusion
A_H2=2.827;
A_H2O=2.641;
coldiam_H2_H2O=(A_H2+A_H2O)/2;

e_k_H2=59.7;
e_k_H2O=809.1;
e_k_H2_H2O=(e_k_H2*e_k_H2O)^.5;

coeff_a=Temp/e_k_H2_H2O;
A=1.06036;
B=.15610;
C=.193000;
D=.47635;
E=1.03587;
FF=1.52996;
G=1.76474;
H=3.89411;
col_int_a=A/coeff_a^B+C/exp(D*coeff_a)+E/exp(FF*coeff_a)+G/exp(H*coeff_a);
D_H2_H2O=.0018583*(1/molwtH2+1/molwtH2O)^.5*Temp^1.5/(Ptot/101300*col_int_
a*coldiam_H2_H2O^2*10000);
% effective diffusion for hydrogen and water
Deff_H2=P_a/T_a.*(1./DkH2+1./D_H2_H2O).^-1;
Deff_H2O=P_a/T_a.*(1./DkH2O+1./D_H2_H2O).^-1;
```

APPENDIX C: POROSITY GRADED ELECTRODE MODEL CODE

```
function solution_finder_concaveup
%Developed : Dr Baskar Ganapathysubramanian & Reuben Flesner
%July 29, 2009
%Version 2.0
%Solves the stiff-coupled ODE BVP by the shooting method. Additionaly uses
%a function minimizer to find the optimal initial value
close all
clear all
clc

format long
eta_g = 0.005;

% Now run this minimization algorithm to get the best value of eta_g that
% results in a solution that satisfies all boundary conditions
% This function is the error minimizer
options = optimset('Display','off','TolFun',1e-2);

eta_optimal = fminsearch(@fc,eta_g,options);

% After the optimal eta is found, it is sent to final_solve.
[x,y] = final_solve_concaveup(eta_optimal);

global La It
figure(1)                   %plot voltage
plot(x,y(:,1))
% axis([0 La 0 .5])
xlabel('Thickness (m)')
ylabel('Voltage (V)')
figure(3)                   %plot H2 pressure
plot(x,y(:,3))
xlabel('Thickness (m)')
ylabel('H2 Partial Pressure(Pa)')
% axis([0 .00015 80000 86200])
figure(4)                   %plot current
plot(x,y(:,4))
xlabel('Thickness (m)')
ylabel('Current Density(A)')
% axis([0 La 0 5000])

eta_optimal         %output eta_optimal for viewing
y(end,1)            %output voltage for viewing

global P_free P_interface b         %call global variables
x = 0:.000001:La;
P_a=(P_free-P_interface)./P_free*((b.^2+La*b)*P_free./(La*(x+b)) + P_free-
(P_free*(b.^2+La*b)./(La*b))) + P_interface;
figure(7)
plot(x,P_a)                   %plot particle grading profile
xlabel('Thickness (m)')
ylabel('particle diameter (m)')
```

```
axis([0 .00015 0 1])
% This function is error calculator
% This function solves the Initial value ODE
function error = fc(eta_g)
format long

global cond_el          %declare global variable
global cond_io          %declare global variable
global d                %declare global variable
global P_free           %declare global variable
global P_interface      %declare global variable
global eta_p            %declare global variable
global eta_p_end        %declare global variable
global H2_frac          %declare global variable
global It               %declare global variable
global La               %declare global variable
global necking          %declare global variable
global nel              %declare global variable
global press_o          %declare global variable
global Ptot             %declare global variable
global Temp

Temp = 1173;
cond_el = 2e6;          %input bulk electrical conductivity value
cond_io = 3.44e4*exp(-10300/Temp);  %input bulk ionic conductivity value
P_free =      0.6;     %input porosity percent at free surface
P_interface = 0.2;     %input porosity percent at EE interface

d = 3e-6;           %particle diameter
del = d;            %reassignment for function micro_bc_a
dio = d;            %reassignment for function micro_bc_a

It = 12000;              %input total current through electode

La=.000150;             %input electrode thickness
H2_frac=0.85;           %input fraction of feed gas that is hydrogen
Ptot=101300;            %input total pressure, usually atmospheric
pressure
necking = 0.5;          %input necking factor between particles
nel = 0.36;             %input number fraction of electronic conducting
particles

% this function finds Rel for the BC at 'a' for interval 'a' to 'b'
[Rel_bc]=micro_bc_a(del,dio,cond_el,necking,nel); %find Rel at free
surface

% this function finds Rio for the BC at 'b' for interval 'a' to 'b'
[Rio_bc]=micro_bc_b(del,dio,cond_io,necking,nel); %find Rio at free
surface

% Each shoot will be compared with eta_p_end.
eta_p = Rel_bc * It;
eta_p_end = Rio_bc * It;
```

```
press_o = H2_frac * Ptot;

options = odeset('RelTol',1e-10,'Stats','notify','NonNegative',[1 3 4]);
% These are the initlal value conditions for the shooter.
[x,y]=ode15s(@eq_system,[0 La],[eta_g eta_p press_o It],options);

%check to see if this guessed value of eta_g results in a valid eta_prime
%at the right side boundary
error = (eta_p_end-y(end,2)).^2         %output error to watch converge

%This function is the ODE solver
%Developed : Reuben Flesner, Dr Baskar Ganapathysubramanian
%July 29, 2009
%Version 2.0
function dy = eq_system(x,y)
format long
dy = zeros(4,1);

global A              %declare global variable
global anode_EC       %declare global variable
global b              %declare global variable
global beta           %declare global variable
global c_angle        %declare global variable
global d              %declare global variable
global F              %declare global variable
global n              %declare global variable
global P_a            %declare global variable
global R              %declare global variable
global T_a            %declare global variable

%call global variables into function
global cond_el cond_io P_free P_interface H2_frac La necking nel Ptot Temp
%
==========================================================================
b = 0.0001;            %b changes the grading profile 1=straight line,
small values make more non-linear profiles
P_a=(P_free-P_interface)/P_free*((b^2+La*b)*P_free/(La*(x+b)) + P_free-
(P_free*(b^2+La*b)/(La*b))) + P_interface;

del = d;              %diamteter of electronic conducting particle (m)
dio = d;              %diamteter of ionic conducting particle (m)
T_a = 3;              %tortuosity
c_angle = pi/12;      %contact angle between particles (radians)
anode_EC = 4000;      %exchange current (A/m^2)
F = 96485;            %Faraday's constant (C/mol)
n = 1;                %number of electrons in limiting reaction step
R = 8.314;            %gas constant (J/(mol*K))
beta = 0.5;           %charge transfer symmetry factor

%the micro and macro functions are called to find resistivity, reaction
%area, pore diameter, diffusion coefficients and the partial pressure of
H2
```

```
[Rel,Rio,A,pore_diam]=micro(del,dio,P_a,cond_el,cond_io,necking,nel,c_angl
e);
[Deff_H2,Deff_H2O,PH2] = macro (pore_diam,Temp,P_a,T_a,Ptot,H2_frac);

dy(1) = y(2);
dy(2) = (Rel+Rio).*A*anode_EC*(y(3)/PH2*exp(beta*n*F*y(1)/(R*Temp))-
((Ptot-y(3))/(Ptot-PH2))*exp(-beta*n*F*y(1)/(R*Temp)));
dy(3) = -R*Temp.*y(4)/(2*F*((1-y(3)/Ptot).*Deff_H2+y(3)./Ptot.*Deff_H2O));
dy(4) = -A*anode_EC*(y(3)/PH2*exp(beta*n*F*y(1)/(R*Temp))-(Ptot-
y(3))/(Ptot-PH2)*exp(-beta*n*F*y(1)/(R*Temp)));

function [Rel_bc]=micro_bc_a(del,dio,cond_el,necking,nel)
format long
rela = del/2;        %particle radius
rioa = dio/2;        %particle radius
Z = 6;               %coordination number in random binary packing
nela=nel;
Pa = rioa./rela;     %particle radius ratio
%%%%%%%%%%   Percolation Theory Start
pe0a = 0;       %probability of conduction occurring at the percolation
limit
Zel_el0a = 4.236-2.472*(-(pe0a.^2.5-1)).^.4;    %elec to elec contact at
p=0
ncethresha = Pa.^2*Zel_el0a./(Z+(Pa.^2-1)*Zel_el0a);    %critical number
fraction for elec conduction

%%%%%%%%%%   Percolation Theory End
Rel_bc = (1-ncethresha).^2./(necking*cond_el*(nela-ncethresha).^2);
%effective elec resistivity

function [Rio_bc]=micro_bc_b(del,dio,cond_io,necking,nel)
format long
rela = del/2;        %particle radius
rioa = dio/2;        %particle radius
Z = 6;               %coordination number in random binary packing
nela=nel;
nioa = 1-nela;
Pa = rioa./rela;         %particle radius ratio
%%%%%%%%%%   Percolation Theory Start
pi0a = 0;       %probability of conduction occurring at the percolation
limit
Zio_io0a = 4.236-2.472*(-(pi0a.^2.5-1)).^.4;    %ionic to ionic contact at
p=0
ncithresha = Pa.^-2*Zio_io0a./(Z+(Pa.^-2-1)*Zio_io0a);  %critical number
fraction for ionic conduction
%%%%%%%%%%   Percolation Theory End
Rio_bc = (1-ncithresha).^2./(necking*cond_io*(nioa-ncithresha).^2);
%effective ionic resistivity

function
[Rel,Rio,A,pore_diam]=micro(del,dio,P_a,cond_el,cond_io,necking,nel,c_angl
e)
format long
```

```
rela = del/2;          %particle radius
rioa = dio/2;          %particle radius
Z = 6;                 %coordination number in random binary packing

nela=nel;                %number fraction of electronic conducting
particles
nioa = 1-nela;           %number fraction ofionic conducting particles
Pa = rioa./rela;         %particle radius ratio

Zela = 3+((Z-3)./(nela+(1-nela).*Pa.^2));        %elec coordination number
Zioa = 3+(((Z-3)*Pa.^2)./(nela+(1-nela).*Pa.^2));%ionic coordination
number

Zel_ela = nela*Z./(nela+(1-nela).*Pa.^2); %elec to elec coordination
number
Zio_ioa = nioa*Z./(nioa+(1-nioa).*Pa.^-2);  %ion to ion coordination
number
pela = (1-((4.236-Zel_ela)/2.472).^2.5).^0.4;
pioa = (1-((4.236-Zio_ioa)/2.472).^2.5).^0.4;

% number of particles per volume and reaction/contact surface area
if Pa>1
    n_stara = (1-P_a)./(4/3*pi*rela.^3.*(nela+(1-nela).*Pa.^3));
    A =
pi*(rela*sin(c_angle))^2.*n_stara.*nela.*nioa.*Zela.*Zioa/Z.*pela.*pioa;
else
    n_stara = (1-P_a)./(4/3*pi*rioa.^3.*(nioa+(1-nioa).*Pa.^-3));
    A =
pi*(rioa*sin(c_angle))^2.*n_stara.*nela.*nioa.*Zela.*Zioa/Z.*pela.*pioa;
end
%%%%%%%%%%%%%%%%%%%%%%%%%%%%%%%%%%%%%%%%%%%%%%%%%%%%%%%%%%%%%%%%    Percolation Theory
Start
pe0a = 0;       %probability of conduction occurring at the percolation
limit
pi0a = 0;       %probability of conduction occurring at the percolation
limit
Zel_el0a = 4.236-2.472*(-(pe0a.^2.5-1)).^.4;    %elec to elec contact at
p=0
Zio_io0a = 4.236-2.472*(-(pi0a.^2.5-1)).^.4;    %ionic to ionic contact at
p=0

ncethresha = Pa.^2*Zel_el0a./(Z+(Pa.^2-1)*Zel_el0a);    %critical number
fraction for elec conduction
ncithresha = Pa.^-2*Zio_io0a./(Z+(Pa.^-2-1)*Zio_io0a);  %critical number
fraction for ionic conduction
%%%%%%%%%%%%%%%%%%%%%%%%%%%%%%%%%%%%%%%%%%%%%%%%%%%%%%%%%%%%%%%%    Percolation Theory
End
Rel = (1-ncethresha).^2./(necking*cond_el*(nela-ncethresha).^2);
%effective elec resistivity
Rio = (1-ncithresha).^2./(necking*cond_io*(nioa-ncithresha).^2);
%effective ionic resistivity

% pore diameter calculation
```

```
pore_diam = 2/3*(del*P_a/(1-P_a))*(nela+(1-nela)*Pa^3)/(nela+(1-
nela)*Pa^2);

function [Deff_H2,Deff_H2O,PH2] = macro
(pore_diam,Temp,P_a,T_a,Ptot,H2_frac)

% see previous code for macro model comments
pore_radiusa=pore_diam/2;
molwtH2=2.0158;
molwtH2O=18.0148;

PH2=H2_frac*Ptot;

% Knudsen diffusion
DkH2=97*pore_radiusa*(Temp/molwtH2)^.5;
DkH2O=97*pore_radiusa*(Temp/molwtH2O)^.5;

% Chapman-Enskog Binary diffusion
A_H2=2.827;
A_H2O=2.641;
coldiam_H2_H2O=(A_H2+A_H2O)/2;

e_k_H2=59.7;
e_k_H2O=809.1;
e_k_H2_H2O=(e_k_H2*e_k_H2O)^.5;

coeff_a=Temp/e_k_H2_H2O;
A=1.06036;
B=.15610;
C=.193000;
D=.47635;
E=1.03587;
FF=1.52996;
G=1.76474;
H=3.89411;

col_int_a=A/coeff_a^B+C/exp(D*coeff_a)+E/exp(FF*coeff_a)+G/exp(H*coeff_a);
D_H2_H2O=.0018583*(1/molwtH2+1/molwtH2O)^.5*Temp^1.5/(Ptot/101300*col_int_
a*coldiam_H2_H2O^2*10000);

% effective diffusion for hydrogen and water
Deff_H2=P_a/T_a.*(1./DkH2+1./D_H2_H2O).^-1;
Deff_H2O=P_a/T_a.*(1./DkH2O+1./D_H2_H2O).^-1;


function [x,y] = final_solve_concaveup(eta_optimal)
%Developed : Dr Baskar Ganapathysubramanian & Reuben Flesner
%July 29, 2009
%Version 2.0
%Solves the sstiff-coupled ODE BVP by the shooting method. Additionaly
uses
%a function minimizer to find the optimal initial value
format long
```

```
global It                %call global variables into function
global eta_p             %call global variables into function
global La                %call global variables into function
global press_o           %call global variables into function

options = odeset('RelTol',1e-10,'Stats','off','NonNegative',[1 3 4]);
[x,y]=ode15s(@fuelcell,[0 La],[eta_optimal eta_p press_o It],options);

%This function is the ODE solver
%Developed : Reuben Flesner, Dr Baskar Ganapathysubramanian
%July 29, 2009
%Version 2.0

function dy = fuelcell(x,y);
format long
dy = zeros(4,1);

%call global variables into function
global anode_EC b beta c_angle cond_el cond_io d P_free P_interface
global F necking nel n P_a R T_a Temp H2_frac La Ptot

% this equation defines the particle size grading profile
P_a = (P_free-P_interface)/P_free*((b^2+La*b)*P_free/(La*(x+b)) + P_free-
(P_free*(b^2+La*b)/(La*b))) + P_interface;
del = d;         %del = dio
dio = d;

[Rel,Rio,A,pore_diam]=micro(del,dio,P_a,cond_el,cond_io,necking,nel,c_angl
e);
[Deff_H2,Deff_H2O,PH2] = macro (pore_diam,Temp,P_a,T_a,Ptot,H2_frac);

dy(1) = y(2);
dy(2) = (Rel+Rio).*A*anode_EC*(y(3)/PH2*exp(beta*n*F*y(1)/(R*Temp))-
((Ptot-y(3))/(Ptot-PH2))*exp(-beta*n*F*y(1)/(R*Temp)));
dy(3) = -R*Temp.*y(4)/(2*F*((1-y(3)/Ptot).*Deff_H2+y(3)./Ptot.*Deff_H2O));
dy(4) = -A*anode_EC*(y(3)/PH2*exp(beta*n*F*y(1)/(R*Temp))-(Ptot-
y(3))/(Ptot-PH2)*exp(-beta*n*F*y(1)/(R*Temp)));

function
[Rel,Rio,A,pore_diam]=micro(del,dio,P_a,cond_el,cond_io,necking,nel,c_angl
e)
format long

rela = del/2;         %particle radius
rioa = dio/2;         %particle radius
Z = 6;                 %coordination number in random binary packing

nela=nel;
nioa = 1-nela;
Pa = rioa./rela;          %particle radius ratio
% volfrac_ela = nela./((1-nela).*Pa.^3+nela);
% volfrac_ioa = nioa./((1-nioa)*Pa.^-3+nioa);
```

```
Zela = 3+((Z-3)./(nela+(1-nela).*Pa.^2));
Zioa = 3+(((Z-3)*Pa.^2)./(nela+(1-nela).*Pa.^2));

Zel_ela = nela*Z./(nela+(1-nela).*Pa.^2);
Zio_ioa = nioa*Z./(nioa+(1-nioa).*Pa.^-2);
pela = (1-((4.236-Zel_ela)/2.472).^2.5).^0.4;
pioa = (1-((4.236-Zio_ioa)/2.472).^2.5).^0.4;

if Pa>1
    n_stara = (1-P_a)./(4/3*pi*rela.^3.*(nela+(1-nela).*Pa.^3));
    A =
pi*(rela*sin(c_angle))^2.*n_stara.*nela.*nioa.*Zela.*Zioa/Z.*pela.*pioa;
else
    n_stara = (1-P_a)./(4/3*pi*rioa.^3.*(nioa+(1-nioa).*Pa.^-3));
    A =
pi*(rioa*sin(c_angle))^2.*n_stara.*nela.*nioa.*Zela.*Zioa/Z.*pela.*pioa;
end
%%%%%%%%%%%%%%%%%%%%%%%%%%%%%%%%%%%%%%%%%%%%%%%%%%%%%%%%    Percolation Theory
Start
pe0a = 0;       %probability of conduction occurring at the percolation
limit
pi0a = 0;       %probability of conduction occurring at the percolation
limit
Zel_el0a = 4.236-2.472*(-(pe0a.^2.5-1)).^.4;    %elec to elec contact at
p=0
Zio_io0a = 4.236-2.472*(-(pi0a.^2.5-1)).^.4;    %ionic to ionic contact at
p=0
ncethresha = Pa.^2*Zel_el0a./(Z+(Pa.^2-1)*Zel_el0a);    %critical number
fraction for elec conduction
ncithresha = Pa.^-2*Zio_io0a./(Z+(Pa.^-2-1)*Zio_io0a);  %critical number
fraction for ionic conduction
%%%%%%%%%%%%%%%%%%%%%%%%%%%%%%%%%%%%%%%%%%%%%%%%%%%%%%%%    Percolation Theory
End
Rel = (1-ncethresha).^2./(necking*cond_el*(nela-ncethresha).^2);
%effective elec resistivity
Rio = (1-ncithresha).^2./(necking*cond_io*(nioa-ncithresha).^2);
%effective ionic resistivity

% pore diameter calculation
pore_diam = 2/3*(del*P_a/(1-P_a))*(nela+(1-nela)*Pa^3)/(nela+(1-
nela)*Pa^2);

function [Deff_H2,Deff_H2O,PH2] = macro
(pore_diam,Temp,P_a,T_a,Ptot,H2_frac)
pore_radiusa=pore_diam/2;

molwtH2=2.0158;
molwtH2O=18.0148;

PH2=H2_frac*Ptot;
%    knudsen calculations    ==========================================
DkH2=97*pore_radiusa*(Temp/molwtH2)^.5;
```

```
DkH2O=97*pore_radiusa*(Temp/molwtH2O)^.5;

A_H2=2.827;
A_H2O=2.641;
coldiam_H2_H2O=(A_H2+A_H2O)/2;

e_k_H2=59.7;
e_k_H2O=809.1;
e_k_H2_H2O=(e_k_H2*e_k_H2O)^.5;

coeff_a=Temp/e_k_H2_H2O;
A=1.06036;
B=.15610;
C=.193000;
D=.47635;
E=1.03587;
FF=1.52996;
G=1.76474;
H=3.89411;

col_int_a=A/coeff_a^B+C/exp(D*coeff_a)+E/exp(FF*coeff_a)+G/exp(H*coeff_a);
D_H2_H2O=.0018583*(1/molwtH2+1/molwtH2O)^.5*Temp^1.5/(Ptot/101300*col_int_
a*coldiam_H2_H2O^2*10000);

Deff_H2=P_a/T_a.*(1./DkH2+1./D_H2_H2O).^-1;
Deff_H2O=P_a/T_a.*(1./DkH2O+1./D_H2_H2O).^-1;
```